ABSTRACT

Title of Dissertation: ATOMISTIC MODELING OF SOLID INTERFACES IN ALL-SOLID-STATE LI-ION BATTERIES

Yizhou Zhu, Doctor of Philosophy, 2018

Dissertation Directed By: Assistant Professor Yifei Mo, Department of Materials Science and Engineering

All-solid-state Li-ion battery based on solid electrolyte is a promising next-generation battery technology, providing intrinsic safety and higher energy density. Despite the development of solid electrolyte materials with high ionic conductivity, the high interfacial resistance and interfacial degradation at the solid electrolyte–electrode interfaces limit the electrochemical performance of the all-solid-state batteries. Fundamental understanding about the solid-solid interfaces is essential to improve the performance of all-solid-state batteries.

In this dissertation, I perform first principles computation to bring new understanding about these solid interfaces. Using our developed computation approach based on large materials database, I calculated the intrinsic electrochemical stability window of solid electrolytes and predicted interphase decomposition products. I revealed the effects of different types of interphase layers on the interface stability and

battery performance, and also provided interfacial engineering strategies to improve interface compatibility.

Lithium metal anode can provide significantly higher energy density of Li-ion batteries. However, only a limited number of materials are known to be stable against lithium metal due to its strong reducing nature. Using first-principles calculations and large materials database, I revealed the general trend of lithium reduction behavior in different material chemistry. Different from oxides, sulfides, and halides, nitride anion chemistry exhibits unique stability against lithium metal, which is either thermodynamically intrinsic or a result of stable passivation. Therefore, many nitrides materials are promising candidate materials for lithium metal anode protection.

Since solid electrolytes in all-solid-state batteries are often polycrystalline, the grain boundaries can have an important impact on the ion diffusion in solid electrolytes. I performed molecular dynamics simulations to study the ion diffusion at grain boundaries in solid electrolyte materials, and showed the distinct diffusion behavior at grain boundaries different from the facile ion transport in the bulk. In addition, I studied the order-disorder transition induced by mechanical strain in lithium garnet. Such transition can lead to orders of magnitude change in ionic diffusivity.

This series of work demonstrated that computational modeling techniques can help to gain critical fundamental understandings of the solid interfaces in all-solid-state Li-ion battery, and to provide practical engineering strategies to improve the battery performance.

ATOMISTIC MODELING OF SOLID INTERFACES IN ALL-SOLID-STATE LI-ION BATTERIES

by

Yizhou Zhu

Dissertation submitted to the Faculty of the Graduate School of the
University of Maryland, College Park, in partial fulfillment
of the requirements for the degree of
Doctoral of Philosophy
2018

Advisory Committee:
Professor Yifei Mo, Chair
Professor Peter Chung
Professor Liangbing Hu
Professor Eric Wachsman
Professor Chunsheng Wang

Acknowledgements

First of all, I would like to express my sincere gratitude to my Ph.D. advisor Professor Yifei Mo. He is both a great researcher and a great mentor, and these two add up to be a great advisor. Research side, the most important things I learned from him are: how to pick important scientific questions, how to think critically, and how to get insights from computation and modeling. Mentoring side, he put huge amount of time and efforts on training me. Just pick one example, when I was writing my very first paper in his group, we had more than 40 iterations on revising the manuscript. During the past four years, I never ever regretted joining his group and working with him. For me, this is a great four-year journey.

I would also thank Prof. Chunsheng Wang, Prof. Liangbing Hu, Prof. Eric Wachsman, and Prof. Peter Chung. I learnt a lot from them during the interactions and collaborations with them. This dissertation would not have been possible without the advice from these outstanding researchers.

I also want to thank my labmates and collaborators: Xingfeng He, Qiang Bai, Adelaide Mei-Chun Nolan, Yunsheng Liu, Alex Epstein, Dr. Fudong Han, Dr. Kun Fu, Dr. Wei Luo, Dr. Xiulin Fan, etc. I enjoyed the collaborations and discussions with them, and I appreciate all the help they offered to me during the past few years.

Additional thanks to the coffee machine in our office, this work (literally) cannot be finished without its continuous coffee support.

I also thank my friends Dr. Yubing Zhou, Jianan Li, Yan Ding, Juan He, Dr. Liangfang Zhao, Lijuan Liu, Yanxue Hong, Xuan Xiao, Wenying Li, Bowen Liang, Tongfei Chen, Yuwang Chen, Dr. Lei Zhang, Dr. Bi-cheng Zhou. They offered me

help, suggestions, and encouragement in the past few years, especially during my hard times.

Special thanks to Dr. Shuze Zhu. Thanks for all the support, understanding, and accompany, which gives me the courage to pursue my dream.

Last and most importantly, I want to thank my parents and my grandparents, for their unconditional love and support throughout my whole life.

Table of Contents

Chapter 1. Introduction

The continued drive for high energy density Li-ion batteries has imposed ever-stricter requirements on the electrolyte materials. Current organic liquid electrolytes in commercial Li-ion batteries are flammable, causing notorious safety issues. Moreover, the limited electrochemical window of the organic liquid electrolytes limits the choice of electrode materials and hence the achievable energy density of the Li-ion batteries.

All-solid-state Li-ion batteries (ASLiBs) based on ceramic solid electrolyte (SE) materials are a promising next-generation energy storage technology with high energy density and enhanced cycle life.[1,2] ASLiBs benefit from extra safety provided by intrinsically non-flammable ceramic solid electrolytes materials, thus is considered to be a promising ultimate solution to the notorious safety issue of Li-ion batteries.

Thanks to the recent discovery and development of Li ionic conductor materials, such as Li lithium thiophosphates[1,3,4] and Li garnet-type materials,[5,6] high Li ionic conductivity of 1 to 10 mS/cm comparable to the organic liquid electrolytes has been achieved in the solid electrolyte materials. Moreover, the claimed outstanding stability of ceramic solid electrolyte materials may enable Li metal anode and high-voltage cathodes,[1,2] which can significantly increase the energy density of Li-ion batteries.[7-9]

However, despite the high bulk ionic conductivity achieved in the solid electrolyte materials, the electrochemical performance of ASLiBs is still not comparable to those assembled with liquid electrolytes. High interfacial resistance and interfacial degradation are the key limiting factors of the ASLiB performance, including poor cyclability, low coulombic efficiency, etc. Therefore, to resolve the high interfacial resistance and to further improve the ASLiBs performance, fundamental understanding of the origin of high

interfacial resistance is required. In addition, specific interfacial engineering and material design strategies are needed to guide the future development of ASLiBs with improved interfacial stability and interfacial ionic transport.

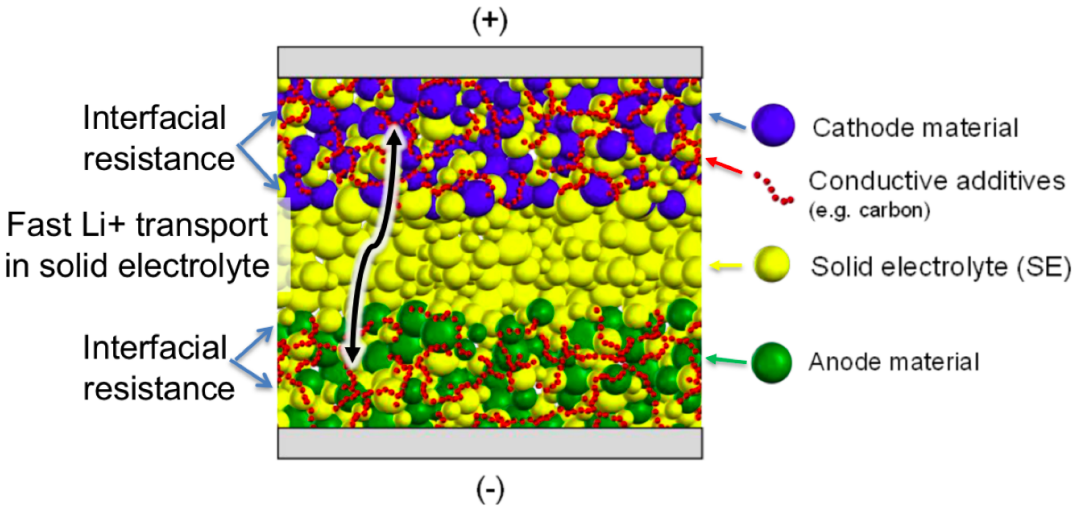

Figure 1.1 Schematic illustration of all-solid-state Li-ion batteries.[10] Ion transport at multiple interfaces, including the interfaces between solid electrolytes and electrodes, grain boundaries in solid electrolytes, are involved during battery operation. The properties of these interfaces, especially the ionic transport properties and interface stabilities, are critical to the battery performance.

Computational modeling can provide fundamental understanding of the properties and mechanisms at these buried interfaces, which are difficult to access and characterize in experiments. In this dissertation, I will show how we use computational modeling to investigate the interfacial properties in ASLiBs. Using first principles calculations and molecular dynamics simulations, we gain the fundamental understanding of materials interfaces and provide design strategies to develop interfaces with improved stability for ASLiBs.

1.1 The Stability of Solid Electrolyte – Electrode Interfaces and Engineering Strategies.

Currently, one of the key bottleneck problem of ASLiBs is the high interfacial resistance at the electrolyte–electrode interface. Previously, the high interfacial resistance at these solid-solid interfaces was attributed to multiple factors, including poor physical contact, interfacial degradation, carrier depletion caused by space-charge effect. However, the intrinsic chemical and electrochemical stability of these interfaces were neglected.

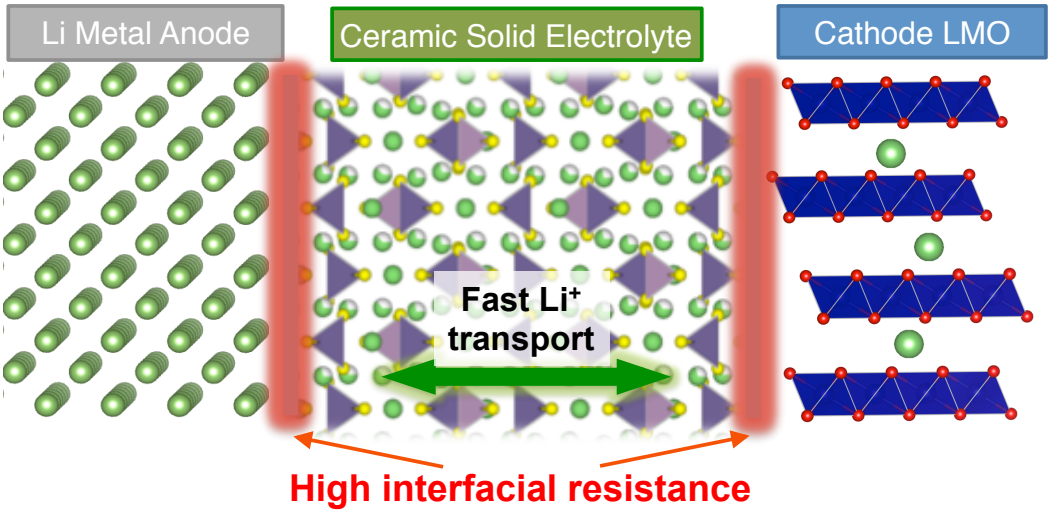

Figure 1.2. Despite the fast bulk ionic transport achieved in bulk solid electrolyte materials, the high interfacial resistance is the limiting factor in ASLiB performance.

Early reports on the electrochemical stability window of solid electrolyte materials were based on conventional cyclic voltammetry measurements. For example, $Li_{10}GeP_2S_{12}$ (LGPS) and $Li_7La_3Zr_2O_{12}$ (LLZO) were reported to be stable from 0 to 5 V. [1,9,11,12] However, later experimental and computational studies questioned the claimed stability of solid electrolyte materials against Li metal and at high voltages.[13,14] It is critical to assess the intrinsic electrochemical stability window of the solid electrolyte materials. Cycling outside of the intrinsic electrochemical window of the solid electrolyte materials would lead to the

spontaneous formation of an interphase layer, and these interphase layers can have significant effects on the interfacial resistance and the overall performance of the ASLiBs. The continued decompositions at the solid electrolyte–electrode interfaces may lead to interfacial degradation and poor coulombic efficiency of the ASLiBs. In addition, the interphase layers may be poor ionic conductor, which would result in high interfacial resistance.

In chapter 3, we use computation to investigate the thermodynamics of the interfaces between solid electrolytes and electrodes in ASLiBs. We found that the intrinsic electrochemical windows of solid electrolytes are limited, which leads to the spontaneous formation of interphase layer. I will discuss how the properties of the formed interphase affect the battery performance. Based on their properties, we classify different solid electrolyte–electrode interfaces into different types, and provide strategies to improve the interface stability and battery performance.

1.2 Material Design and Interface Engineering to Enable Lithium Metal Anode

Lithium metal is one of the most promising anode materials. It has the highest theoretical specific capacity and the lowest standard potential, which can significantly boost the energy density of Li-ion batteries. However, strong reducing nature of lithium metal limits its application, causing incompatibility and undesired reaction with most electrolytes. The lack of long-term stability between lithium metal anode and electrolyte leads to quick battery capacity fade and cell failure. In addition, the undesired growth of Li dendrite during cell cycling causes short circuiting in the cell, leading to catastrophic cell failure and safety

issues. Despite decades of research efforts, the goal of stabilizing lithium metal anode over many charge-discharge cycles and long battery life time has not been fully realized.

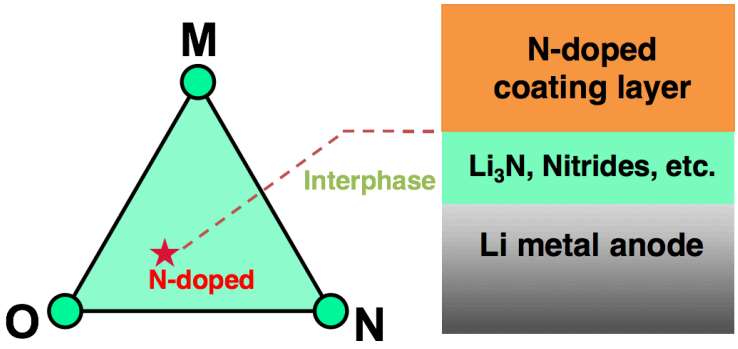

Figure 1.3. Due to the strong reducing nature of lithium metal, identify potential protection coating materials to protect electrolytes against lithium metal reduction is crucial for the development of lithium batteries. We propose to use nitride-based materials chemistry, which has unique intrinsic stability against Li metal reduction, to engineer the anode interface and protect electrolytes from reduction.

To enable Li metal anode, identify materials that are intrinsically stable or can be used as protection coating is critical. However, despite that many lithium solid electrolytes were previously reported to be stable against Li metal, multiple experimental and first principles studies confirmed that most solid electrolytes such as $Li_{10}GeP_2S_{12}$ (LGPS), NASICON-type $Li_{1.3}Al_{0.3}Ti_{1.7}(PO_4)_3$ (LATP), and perovskite $Li_{0.33}La_{0.56}TiO_3$ (LLTO), are not thermodynamically stable against Li metal and will be reduced at the interface. [13-20] Therefore, developing Li-stable materials to protect the solid electrolytes from lithium metal reduction is critical.

Previous discoveries on Li-metal-stable materials are mostly based on a trial-and-error approach. Only a few materials, such as lithium binaries Li_2O, Li_2S, Li_3N, and LiF,

are known to be stable against Li metal. A more comprehensive understanding on the general trend of material stability against Li metal reduction is needed.

In chapter 4, I will show how we use first principles calculations powered by large-scale materials database, to uncover lithium-stable materials out of a variety of chemistry across the periodic table. we discovered that nitrides exhibit thermodynamically intrinsic stability against lithium metal. Such unique stability is lacking in other materials chemistry, such as oxides, sulfides, and halides, which are commonly used for lithium protection. The intrinsic stability of many nitride compounds against lithium reduction makes them ideal candidate materials to protect lithium metal anode over long term.

1.3 Ionic Diffusion at the Grain Boundary in Solid Electrolyte Materials

The recent advancement in all-solid-state Li-ion batteries is mainly driven by the discovery and development of novel solid electrolyte materials. Despite that they are solid materials, some of them can provide liquid-like high ionic conductivity. The fast bulk ionic transport in these has drawn a lot of research effort to understand the underlying mechanism of its fast ion diffusion.[21-25]

However, the employed solid electrolytes in all-solid-state Li-ion batteries are usually polycrystalline materials. Therefore, besides the bulk ionic transport, the ion diffusion at grain boundaries can also have a significant impact on the overall ionic transport and thus battery performance. [26,27]

Grain boundaries usually exhibit different structures and chemistry from bulk, which can lead to distinct ionic diffusion behavior. Moreover, some recent studies revealed

that the grain boundaries are related to lithium dendrite growth, as lithium dendrite show preference growth inside the grain boundary of solid electrolyte.[28,29]

Despite the extensive study on the bulk properties, current understanding on the grain boundaries in solid electrolytes are still limited. We select Li-stuffed garnet $Li_7La_3Zr_2O_{12}$ (LLZO) as a model system to study the grain boundary diffusion in super ionic conductor materials.

In chapter 5, I perform molecular dynamics simulation to investigate the ionic diffusion at grain boundaries in lithium garnet. We found that grain boundaries in lithium garnet exhibit slower ion transport compared to the bulk. Through analyzing the atomistic structure of grain boundaries, we revealed that the framework shows limited change and that lithium ions exhibit different configuration at the grain boundaries compared to bulk.

1.4 Strain Effect on Ionic Diffusion in Lithium Garnet

Mechanical strain is can significantly affect the ion diffusion in ionic conductor materials.[30,31]. The strain on the solid electrolytes may be caused by the volume change of electrode materials during cycling or by the applied pressure during the assembling of ASLiBs. Lithium garnet is a promising solid electrolyte for all-solid-state Li-ion batteries. However, there is little information about the effect of mechanical strain on the ion diffusion of lithium garnet.

In chapter 6, I will show our simulation results about the strain effects on the ionic diffusion in lithium garnet. We found that there is a strong coupling between the lattice parameters and lithium sublattice ordering. Applying mechanical strain can induce an order-disorder transition in lithium sublattice of lithium garnet. This strain-induced order-disorder

transition of lithium sublattice can have a significant effect on the Li-ion diffusion in lithium garnet.

Chapter 2. Computational Methods

In this chapter, I introduce our computation method to evaluate the interface stability in the all-solid-state Li-ion batteries.

2.1. Interface Equilibrium Criteria

To evaluated the stability of the interfaces, we consider the following equilibrium criteria. These equilibrium criteria must be satisfied for the interfaces at thermodynamic equilibrium.

1) Equilibrium of neutral Li

Stable interface should reach the equilibrium of neutral Li (under applied potential) across the interfaces. Through this equilibrium, the Li chemical potential μ_{Li} should be equal at the contact points between solid electrolyte and electrode materials. This criterion is equivalent to the equilibrium of the materials (i.e., the electrochemical stability) against different electrostatic potential ϕ. The equilibration of μ_{Li} and ϕ are facilitated by the good mobility of Li ions in the solid electrolytes and electrode materials.

2) Equilibrium of non-Li elements

Stable interface should also reach the equilibrium of neutral non-Li elements across the interfaces. Similar to the equilibrium of Li, the equilibrium of any non-Li element M at the interface requires the equivalence of chemical potential μ_M at the contact points between the solid electrolytes and electrode materials, though non-Li elements, such as Co and S, are usually not as mobile as Li.

3) The full thermodynamic equilibrium

This criterion is to evaluate the chemical stability of the interface, which is

determined by whether the two materials mixed by a certain ratio can have an exothermic reaction to form other phases as the phase equilibria at the same composition. Such reaction would not exist if two materials were chemically stable against each other, where the phase equilibria would be equivalent to two original materials. If the phase equilibria were different from the combination of original two materials, we calculate the decomposition energy to evaluate the driving force. This criterion considered the full equilibrium of all elements, while only one element is allowed to equilibrate in criteria 1 and 2.

4) The equilibrium of the two materials in contact under an applied potential.

This criterion is to evaluate the electrochemical stability of the interface, which is different from the chemical stability in the absence of an applied potential as in criterion 3. We determined the thermodynamic phase equilibria of the interface as a function of the applied potential. Similar to criterion 3, an exothermic reaction to from other phases at the applied potential suggests thermodynamically favorable decomposition reaction.

We use phase diagram calculations to evaluate the aforementioned criteria. Specifically, we calculate the phase equilibria under different conditions and then evaluate the phase/interface stability and thermodynamic driving force of decomposition.

2.2. Compositional Phase Diagram

The compositional phase diagrams were constructed to evaluate the phase equilibria of a given solid electrolyte or electrode phase with the composition *C*. The phase equilibria were determined by constructing the convex energy hull of all relevant phases in the compositional phase diagram.[32] The phase equilibria at the composition *C* corresponding to the energy minimum $E_{eq}(C)$ were identified by comparing the energy of all relevant phases

in its compositional space. The phase stability of the investigated phase was evaluated using the decomposition energy ΔE_D,

$$\Delta E_D(\text{phase}) = E_{eq}(C) - E(\text{phase}), \qquad \textbf{Eq. 1}$$

of a given phase to its phase equilibria. ΔE_D is the negative of energy above hull.

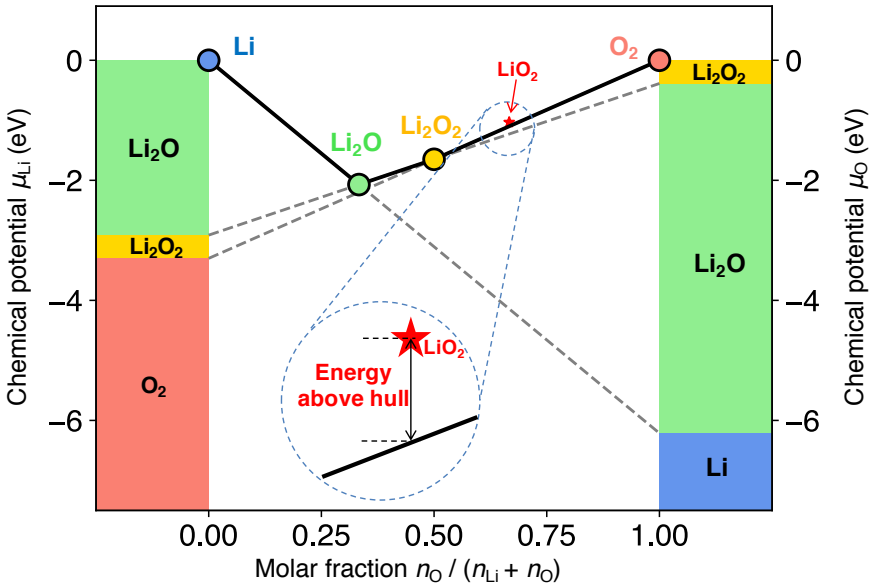

Figure 2.1. An example phase diagram showing the phase stability and electrochemical stability in Li-O system. The convex hull was connected by four stable phases: Li, Li_2O, Li_2O_2, and O_2, while LiO_2 is an unstable phase with a positive energy above hull (intersect). The left and right color bar shows the electrochemical stability of the stable phases. Each color block corresponds to the most stable phase under the given chemical potential of Li or O.

2.3. Grand Potential Phase Diagram

Grand potential phase diagrams were constructed to evaluate the stability of a material in equilibrium with an external environment.[13,32] The grand potential phase

diagram identifies the phase equilibria $C_{eq}(C, \mu_M)$ of a given phase with the composition C in equilibrium with the chemical potential μ_M of element M. The given phase is stable within a certain range of μ_M. Outside the μ_M stable range of the phase, the composition of the phase equilibria $C_{eq}(C, \mu_M)$ have a different number of element M from the original composition C, where the number of element M is changed by Δn_M. The decomposition reaction energy at the chemical potential μ_M is calculated as

$$\Delta E_D^{open}(\text{phase}, \mu_M) = E_{eq}\left(C_{eq}(C, \mu_M)\right) - E(\text{phase}) - \Delta n_M \cdot \mu_M. \quad \textbf{Eq. 2}$$

Using the same scheme in previous studies,[13] the electrode potential ϕ was considered as a part of the Li chemical potential μ_{Li},

$$\mu_{Li}(\phi) = \mu_{Li}^0 - e\phi, \quad \textbf{Eq. 3}$$

where μ_{Li}^0 was the chemical potential of Li metal. In this study, μ_M was referenced to the elementary state μ_M^0, and the applied potential ϕ was referenced to Li metal. The electrochemical window of the phase was estimated as the range of ϕ, where the phase is neither oxidized nor reduced. The decomposition reaction energy at applied voltage ϕ was calculated as

$$\Delta E_D^{open}(\text{phase}, \phi) = \Delta E_D^{open}(\text{phase}, \mu_{Li}(\phi)). \quad \textbf{Eq. 4}$$

2.4. Evaluate the Chemical Stability of Interfaces

In this study, we considered the interface as a pseudo-binary[33] of the solid electrolyte and the electrode, which has a composition

$$C_{Inteface}(C_{SE}, C_{Electrode}, x) = x \cdot C_{SE} + (1 - x) \cdot C_{Electrode} \quad \textbf{Eq. 5}$$

where C_{SE} and $C_{Electrode}$ are the compositions (normalized to one atom per formula) of SE

and electrode materials, respectively, and x is the molar fraction of SE which varies from 0 to 1. The energy of the interface pseudo-binary,

$$E_{\text{Interface}}(\text{SE}, \text{Electrode}, x) = x \cdot E(\text{SE}) + (1 - x) \cdot E(\text{Electrode}) \quad \textbf{Eq. 6}$$

was set to a linear combination of the electrolyte and electrode energies. The decomposition energy of the interface pseudo-binary was calculated similar to Eq. 1 as

$$\begin{aligned} &\Delta E_{\text{D}}(\text{SE}, \text{Electrode}, x) \\ &= E_{\text{eq}}\left(C_{\text{interface}}(C_{\text{SE}}, C_{\text{Electrode}}, x)\right) \\ &- E_{\text{Interface}}(\text{SE}, \text{Electrode}, x) \end{aligned} \quad \textbf{Eq. 7}$$

ΔE_{D}(SE, Electrode, x) includes the decomposition energy ΔE_{D} from Eq. 1 if the SE or the electrode are not thermodynamically stable. We defined $\Delta E_{\text{D,mutual}}$ as the reaction energy between phase equilibria of SE and electrode materials,

$$\Delta E_{\text{D,mutual}}(\text{SE}, \text{Electrode}, x) = \Delta E_{\text{D}}(\text{SE}, \text{Electrode}, x) - x \cdot \Delta E_{\text{D}}(\text{SE}) - (1 - x) \cdot \Delta E_{\text{D}}(\text{Electrode}). \quad \textbf{Eq. 8}$$

The $\Delta E_{\text{D,mutual}}$ describes the mutual reaction between SE and electrode materials excluding the decomposition energy ΔE_{D} (Eq. 1) of the SE and electrode themselves. Since the phase equilibria and the reaction energies vary with the pseudo-binary composition, we identified the minimum of the mutual reaction energy,

$$\Delta E_{\text{D,min,mutual}}(\text{SE}, \text{Electrode}) = \min_{x \in (0,1)} \left[\Delta E_{\text{D,mutual}}(\text{SE}, \text{Electrode}, x)\right], \quad \textbf{Eq. 9}$$

which reaches the minimum at $x = x_{\text{m}}$. At the same interface pseudo-binary composition x_{m}, we calculated the total decomposition energy as

$$\Delta E_{\text{D,min,total}}(\text{SE}, \text{Electrode}) = \Delta E_{\text{D}}(\text{SE}, \text{Electrode}, x_{\text{m}}). \quad \textbf{Eq. 10}$$

It is worth noting that the identified x_{m} corresponds to the most exothermic decomposition reactions, while the actual interphase layer may differ from the most favorable

thermodynamic phase equilibria and may have a distribution of elemental profile and materials compositions across the interfaces.

2.5. Evaluate the Electrochemical Stability of Interfaces

The electrochemical stability of the interface was evaluated for the interface pseudo-binary (Eq. 5) using the grand potential phase diagram described in section 2.3 and the previous study[33]. The decomposition reaction energy $\Delta E_{\mathrm{D}}^{\mathrm{open}}(\mathrm{SE}, \mathrm{Electrode}, x, \phi)$ at applied voltage ϕ was calculated as

$$\begin{aligned}&\Delta E_{\mathrm{D}}^{\mathrm{open}}(\mathrm{SE}, \mathrm{Electrode}, x, \phi)\\&= E_{\mathrm{eq}}\left(C_{\mathrm{eq}}(C_{\mathrm{interface}}(C_{\mathrm{SE}}, C_{\mathrm{Electrode}}, x), \mu_{\mathrm{M}})\right) - E_{\mathrm{interface}}(\mathrm{SE}, \mathrm{Electrode}, x) - \\&\Delta n_{\mathrm{Li}} \cdot \mu_{\mathrm{Li}}(\phi).\end{aligned} \qquad \textbf{Eq. 11}$$

The decomposition reaction energy $\Delta E_{\mathrm{D}}^{\mathrm{open}}$ was normalized to the number of non-Li atoms because the number of Li changes with the phase equilibria at different applied voltage. Similar to section 2.4, we defined the mutual reaction energy $\Delta E_{\mathrm{D,mutual}}^{\mathrm{open}}$ as

$$\begin{aligned}&\Delta E_{\mathrm{D,mutual}}^{\mathrm{open}}(\mathrm{SE}, \mathrm{Electrode}, x, \phi)\\&= \Delta E_{\mathrm{D}}^{\mathrm{open}}(\mathrm{SE}, \mathrm{Electrode}, x, \phi) - x \cdot \Delta E_{\mathrm{D}}^{\mathrm{open}}(\mathrm{SE}, \phi) - (1-x) \cdot \Delta E_{\mathrm{D}}^{\mathrm{open}}(\mathrm{Electrode}, \phi\end{aligned} \qquad \textbf{Eq. 12}$$

to evaluate the reaction energy of the "mutual" reaction between electrolyte and electrode excluding the decomposition energy $\Delta E_{\mathrm{D}}^{\mathrm{open}}(\mathrm{SE}, \phi)$ and $\Delta E_{\mathrm{D}}^{\mathrm{open}}(\mathrm{Electrode}, \phi)$ of the SE and electrode themselves, respectively. Since the phase equilibria and reaction energies are dependent on the pseudo-binary composition, we identified the minimum of mutual reaction energy at a given applied voltage ϕ as

$$\Delta E_{\mathrm{D,min,mutual}}^{\mathrm{open}}(\mathrm{SE}, \mathrm{Electrode}, \phi) = \min_{x \in (0,1)} \left[\Delta E_{\mathrm{D,mutual}}^{\mathrm{open}}(\mathrm{SE}, \mathrm{Electrode}, x, \phi)\right] \qquad \textbf{Eq. 13}$$

for the mutual reaction between the SE and electrode materials under the applied voltage ϕ,

similar to the previous study[33]. If $\Delta E^{\mathrm{open}}_{\mathrm{D,min,mutual}}(\mathrm{SE, Electrode}, \phi) \neq 0$, we calculated the total decomposition reaction energy as

$$\Delta E^{\mathrm{open}}_{\mathrm{D,min,total}}(\mathrm{SE, Electrode}, \phi) = \Delta E^{\mathrm{open}}_{\mathrm{D}}(\mathrm{SE, Electrode}, x_{\mathrm{m}}(\phi), \phi), \qquad \textbf{Eq. 14}$$

where $x_{\mathrm{m}}(\phi)$ is at the minimum point of the mutual reaction energy $\Delta E^{\mathrm{open}}_{\mathrm{D,min,mutual}}$ identified in Eq. 13. If $\Delta E^{\mathrm{open}}_{\mathrm{D,min,mutual}}(\mathrm{SE, Electrode}, \phi) = 0$, the minimum point x_{m} of $\Delta E_{\mathrm{D,min,mutual}}$ in Eq. 9 is used in Eq. 14. For the SE–LCO interfaces, we considered the voltage range of ϕ from 2 V to 5 V for Li-ion batteries.

2.6. Density Functional Theory (DFT) Calculations

Most compounds used in this work to construct phase diagrams were from the Materials Project (MP)[34] and Inorganic Crystal Structure Database (ICSD). We also added additional lithium ternary compounds, which were predicted using substitution prediction algorithm developed by Hautier et al.

The energies of most materials were obtained from the MP database. For materials that are not available in the MP database, density functional theory (DFT) computation based on Perdew–Burke–Ernzerhof (PBE) generalized gradient approximation (GGA) functionals [35] described by the projector augmented-wave approach[36] as implemented in the Vienna Ab initio Simulation Package (VASP)[37] were performed. The parameters of DFT calculations, such as the plane-wave energy cutoff and *k*-points density, were consistent with those used for the MP.[38] The energy correction schemes for transition metal, O, S, N, and F elements were applied as in the MP.[39,40] The calculated reaction energies and voltages were based on DFT energies as in previous studies,[13,32] where the contributions of *PV* terms

and entropy terms were neglected.

We also require the electronic conductivity property of the formed interphases to evaluate the interface properties. Due to the lack of electronic conductivity data from other sources, we used the valence state of transition metal cations and the band gap calculated in GGA to judge whether a phase is electronic insulating. Phases that have transition metal cations at their highest valence state and that have a calculated band gap wider than 0.7 eV in GGA are considered electronic insulating. Though the band gap calculated in GGA is systematically underestimated, we chose our cut-off value as 0.7 eV, which is the GGA calculated gap of Li_3P, a known poor electronic conductor.[19,41]

Chapter 3. Electrochemical and Chemical Stability of the Solid Electrolyte–Electrode Interfaces

The high interfacial resistance at the electrolyte–electrode interface is a crucial problem in ASLiBs, limiting the power and rate performances of the ASLiBs.[2] The high interfacial resistance is attributed to poor interfacial contact,[42] the mechanical failure of the contacts,[43] interfacial degradation due to mutual diffusion,[44] or the formation of lithium-depleted space-charge layer.[2] The lithium-depleted space-charge layer formed at the interface due to the large chemical potential differences between the sulfide solid electrolytes and the oxide cathode materials is often blamed as the cause of high interfacial resistance.[2] The possibility of the decomposition at the interfaces is often overlooked since the solid electrolytes are claimed to have excellent stability.

The claimed outstanding stability of the solid electrolyte materials is based on the widely reported electrochemical window of 0-5 V from cyclic voltammetry (CV) measurements.[1,9,11,12] However, some recent experimental and computational studies questioned the claimed stability of solid electrolyte materials against Li metal and at high voltages. For example, the reduction and oxidation of $Li_{10}GeP_2S_{12}$ (LGPS) at low and high potentials, respectively, in contrast to the originally claimed 0-5 V electrochemical window, have been demonstrated by first principles computation[13] and experiments.[14] Recent *in-situ*

This chapter has been published in
Y. Zhu, X. He, Y. Mo, Origin of outstanding stability in the lithium solid electrolyte materials: insights from thermodynamic analyses based on first principles calculations. ***ACS Applied Materials & Interfaces***, 7, 23685-23693, (2015)
Y. Zhu, X. He, Y. Mo, First principles study on electrochemical and chemical stability of solid electrolyte–electrode interfaces in all-solid-state Li-ion batteries. ***Journal of Materials Chemistry A***, 4, 3253-3266, (2016)

X-ray photoelectron spectroscopy (XPS) experiments also observed the interfacial decomposition of LiPON,[45] lithium lanthanum titanate,[18] and NASICON-type[17] solid electrolyte materials against Li metal. Transmission electron microscopy (TEM) and energy dispersive X-ray (EDX) studies identified interphase layers of tens to a hundred nanometers at the $LiCoO_2$ electrode-electrolyte interfaces with Li_2S-P_2S_5 [46] or LLZO.[44] These interphase layers were attributed to the structural disordering and the mutual diffusion of non-Li elements, such as Co and S, across the interface. And they have significant effects on the interfacial resistance and the overall performance of the ASLiBs. For example, continued decompositions may lead to interfacial degradation and poor coulombic efficiency of the ASLiBs. In addition, the interphase layers may be poor ionic conductor, which would result in high interfacial resistance.

However, the formation mechanisms of such interphase layers and the effects on the performance of ASLiBs have rarely been discussed. Currently, there is limited knowledge about the formation mechanisms of the interphase layers at the buried solid electrolyte–electrode interfaces in ASLiBs. The formation of interphase layers in ASLiBs may be caused by three mechanisms:

1) The reduction or oxidation of the solid electrolyte materials under an applied potential due to their limited electrochemical windows;

2) The chemical reactions between the solid electrolyte and the electrode materials caused by the chemical incompatibility between the solid electrolyte and the electrodes; and

3) The electrochemical reactions of the solid electrolyte–electrode interfaces during the cycling of the ASLiBs.

The thermodynamics for these three mechanisms, which correspond to the chemical

and electrochemical stability of the interfaces, are well defined. To the best of our knowledge, such thermodynamics information has not been available for the solid electrolyte and electrode materials in the context of ASLiBs. Understanding the origin of the interfacial decomposition and the formation mechanisms of interphase layers are critical for resolving the issue of high interfacial resistance in ASLiBs and for guiding the development of ASLiBs.

In this chapter, we employ a computational scheme based on first principles calculations to obtain the thermodynamics of the interfaces between commonly used solid electrolytes and electrodes in ASLiBs. Our results confirmed the strong thermodynamic driving force for the decomposition at interfaces in ASLiBs due to the limited electrochemical window of the solid electrolyte materials and the poor chemical compatibility between the solid electrolyte and the electrodes. In addition, some of the formed interphases and the applied coating layers were demonstrated to improve the interface stability and the performance of the ASLiBs. The interfaces based on different solid electrolyte and interphases were classified into different types, and the strategies to address the interfacial problems were proposed and demonstrated.

3.1 Stability of Solid Electrolyte Materials against Lithium Metal

We first evaluated the electrochemical stability of solid electrolyte materials against Li metal and at low voltages. The crystal structures and the phase equilibria of the commonly used solid electrolyte materials investigated in this study are summarized in Appendix. The phase equilibria, i.e., the phases with the lowest energy, in equilibrium with Li metal were identified by the Li grand potential phase diagrams.

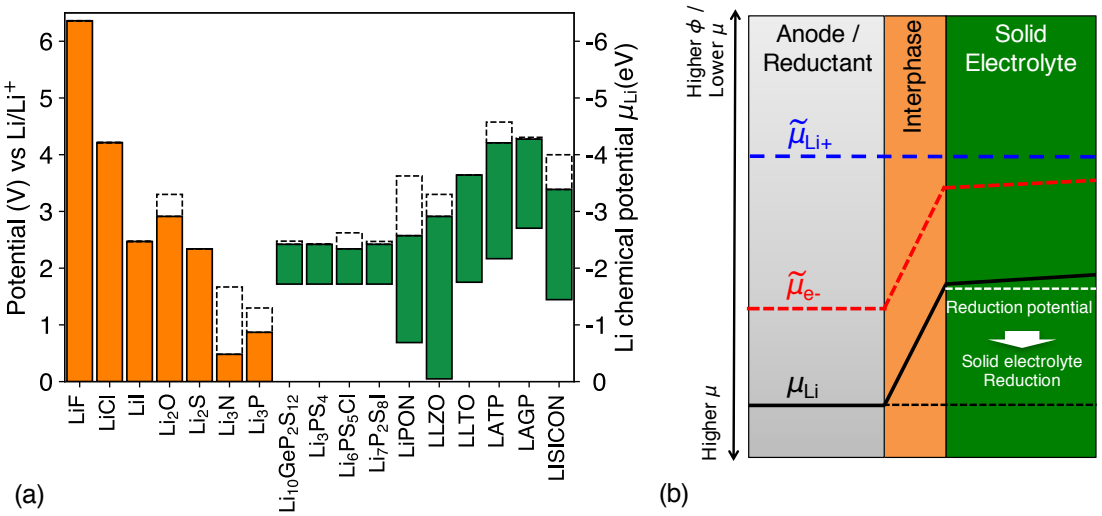

Figure 3.1. (a) Electrochemical window (solid color bar) of solid electrolyte and other materials. The oxidation potential to fully delithiate the material is marked by the dashed line. (b) Schematic diagram about the change of Li chemical potentials μ_{Li} (black line) and the electrochemical potential $\tilde{\mu}_{Li^+}$ (blue dash line) and $\tilde{\mu}_{e^-}$ (red dash line) across the interface between the anode and the solid electrolyte. Since the actual profile of $\tilde{\mu}_{e^-}$ determined by the charge carrier distribution may be complicated,[47,48] the profiles of chemical and electrochemical potential shown here are schematic and may not be linear. The vertical scale is for the electrostatic potential or the voltage referenced to Li, and is reversed for the chemical potential or electrochemical potential.

The solid electrolyte materials are not thermodynamically stable against Li metal (Table 3.1) and are reduced at low voltages with highly favorable decomposition energy (Fig. 3.1a and Table 3.1). In contrast, the Li binary compounds, such as LiF, Li_2O, Li_2S, Li_3P, and Li_3N, are thermodynamically stable against Li metal (Fig. 3.1a). The lithiation and reduction of $Li_{10}GeP_2S_{12}$ (LGPS) starts at 1.71 V, and the LGPS in equilibrium with Li

metal is eventually lithiated into the phase equilibria consisting $Li_{15}Ge_4$, Li_3P, and Li_2S. The Li reduction of the LGPS into these reaction products has a highly favorable reaction energy of -1.25 eV/atom (-3014 kJ/mol of LGPS) at 0 V (Table 3.1). In agreement with our computation, the reduction of LGPS starting at 1.71 V and the formation of Li-Ge alloy after the reduction have been demonstrated in CV and XPS experiments, respectively.[14] Other sulfides materials, such as Li_3PS_4, Li_4GeS_4, Li_6PS_5Cl, and $Li_7P_2S_8I$, are reduced at a similar voltage of ~1.6-1.7 V. The reduction potential is mostly governed by the reduction of P and Ge in the materials, and the reduction products include Li_3P and Li_2S at 0 V. For those materials containing Ge, Cl, and I elements, Li-Ge alloy, LiCl, and LiI are formed, respectively, as a part of phase equilibria at 0 V. The $Li_7P_3S_{11}$ is reduced at a voltage of 2.28 V into Li_3PS_4 with a small decomposition energy, and the majority of the reduction starts at 1.71 V due to the lithiation of Li_3PS_4. The decomposition energy for all these solid electrolyte decreases with the potential to ~ -1 eV/atom at 0 V (Table 3.1), indicating the highly favorable reduction reactions of the sulfide solid electrolytes.

The reduction of oxide solid electrolyte materials $Li_{0.33}La_{0.56}TiO_3$ (LLTO) and $Li_{1.3}Ti_{1.7}Al_{0.3}P_3O_{12}$ (LATP) starts at a voltage of 1.75 and 2.17 V, respectively. Our predicted reduction potential of LLTO is in good agreement with the value of 1.7 - 1.8 V reported in the CV experiments.[20,49] The calculations also found the reduction of Ti^{4+} in LLTO and LATP into Ti^{3+} or lower valences at low voltages (Table 3.1). The reduction of Ti is a widely known problem and is observed at the interfaces of LLTO[18] and LATP[17] with Li metal by *in-situ* XPS spectroscopy. In addition, the reduction of Ge-containing oxide materials $Li_{1.5}Al_{0.5}Ge_{1.5}(PO_4)_3$ (LAGP) and $Li_{3.5}Zn_{0.25}GeO_4$ (LISICON) starting at 2.70 and 1.44 V respectively, and Li-Ge alloys are formed at low voltages (Fig. 3.1a and Table 3.1).

The reductions of LAGP and LISICON are consistent with the experiment studies.[50-52] The good agreements between our computation results and many experiments demonstrated the validity of our computation scheme.

Table 3.1 Reduction reaction of the solid electrolyte materials at Li metal.

	Phase equilibria with Li metal	E_D (eV/atom)
Li_2S	Li_2S (stable)	0
LGPS	$Li_{15}Ge_4$, Li_3P, Li_2S	-1.25
Li_3PS_4	Li_3P, Li_2S	-1.42
Li_4GeS_4	$Li_{15}Ge_4$, Li_2S	-0.89
$Li_7P_3S_{11}$	Li_3P, Li_2S	-1.67
Li_6PS_5Cl	Li_3P, Li_2S, LiCl	-0.96
$Li_7P_2S_8I$	Li_3P, Li_2S, LiI	-1.26
LiPON	Li_3P, Li_3N, Li_2O	-0.66
LLZO	Zr (or Zr_3O), La_2O_3, Li_2O	-0.021
LLTO	Ti_6O, La_2O_3, Li_2O	-0.35
LATP	Ti_3P, TiAl, Li_3P, Li_2O	-1.56
LAGP	Li_9Al_4, $Li_{15}Ge_4$, Li_3P, Li_2O	-1.99
LISICON	$Li_{15}Ge_4$, LiZn, Li_2O	-0.77

Our calculations found the Li reduction of the solid electrolyte materials that are thought to be stable against Li. For example, LiPON, which is calculated using Li_2PO_2N as a representative of the material class, shows a reduction potential of 0.69 V. The final decomposition products of LiPON in equilibrium with Li metal are Li_3N, Li_2O, and Li_3P (Table 3.1), which are consistent with the *in-situ* XPS observations.[45] Although the calculated decomposition energy of LiPON is as large as -0.66 eV/atom at 0 V (Table 3.1),

LiPON is known to be compatible with Li metal as demonstrated by many experimental studies.[12,53] Similarly, Li_3PS_4 and $Li_7P_2S_8I$, which are reported to be compatible with Li metal anode,[9,54,55] are reduced against Li metal and at low voltages (Table 3.1 and Fig. 3.1). Therefore, the stability of these solid electrolyte materials against Li metal is not thermodynamically intrinsic.

The decomposition products, which form an interphase between the solid electrolyte and electrode, passivate the solid electrolyte and inhibit the continuous decomposition. For example, the decomposition products of LiPON, Li_3PS_4, and $Li_7P_2S_8I$ are Li binary compounds, such as Li_2O, Li_2S, Li_3P, Li_3N, and LiI, formed at the Li reduction. The interphase consisting of these decomposition products are stable against the high μ_{Li} of Li metal (Fig. 3.1a), which is beyond the reduction potential (cathodic limit) of the solid electrolyte (Fig. 3.1b). At the equilibrium, the redistribution of Li^+ and other charged carriers (such as electron e^-) are formed at the interface to account for the potential drop across the electrode-electrolyte interface.[56] The electrochemical potential of the highly mobile Li^+, $\tilde{\mu}_{Li^+}$, which includes the electrostatic potential energy, is constant across the interface. In contrast, the electrochemical potential of the electronic carrier $\tilde{\mu}_{e^-}$ (red line in Fig. 3.1b) decreases significantly in the interphase from the anode to the solid electrolyte, since these interphases have poor electronic mobility and conductivity. Therefore, the Li chemical potential μ_{Li} (black line in Fig. 3.1b), which equals to the sum of $\tilde{\mu}_{Li^+}$ and $\tilde{\mu}_{e^-}$, decreases in the interphase from the anode to the solid electrolyte. The high μ_{Li} from the anode decreases to be within the electrochemical window of the solid electrolyte after the passivation of the decomposition interphase. As a result, the decomposition of the solid electrolyte has no thermodynamic driving force to continue into the bulk. The solid electrolyte is stabilized by

the decomposition interphases, which essentially serve as solid-electrolyte-interphases (SEIs) in all-solid-state Li-ion batteries. In summary, the SEI of the decomposition interphase decreases the high Li chemical potential μ_{Li} applied on the solid electrolyte, and bridges the Li chemical potential gap between Li metal and the solid electrolyte. This passivation mechanism explained the observed Li metal compatibility of LiPON, Li_3PS_4, and $Li_7P_2S_8I$.

The passivation mechanism relies on the electronic insulating properties of the decomposition interphase layers to stabilize the solid electrolyte, and is not active if the interphase layer is electronically conductive. For example, the reduction of LGPS, LAGP, and LISICON with Li metal forms electronically conductive Li-Ge alloys, and the lithiation of LLTO and LATP forms titanates with Ti of 3+ or lower valences. The decomposition interphases for these solid electrolytes at Li reductions are mixed electronic and ionic conductors. The electronic conductivity in the interphase cannot account for the drop of $\tilde{\mu}_{\mathrm{e}^-}$ across the interface regardless of the specific electron transport mechanism being metallic, band, or polaronic conduction. These mixed conductor interphases cannot account for the μ_{Li} drop as the change of both $\tilde{\mu}_{\mathrm{Li}^+}$ and $\tilde{\mu}_{\mathrm{e}^-}$ would be small across the interphase. As a result, the solid electrolyte is still exposed to the high μ_{Li} of the anode, and the reduction reaction continues into the bulk. In addition, the mixed electronic and ionic conductor interphase facilitate the kinetic transport of Li ion and electrons for the decomposition reactions.[18] The absence of the passivation mechanism explains the lithiation and reduction of LGPS, LLTO, LATP, LAGP, and LISICON observed in the CV experiments.

It is worth noting that garnet LLZO shows the lowest reduction potential of as low as 0.05 V against Li and the least favorable decomposition reaction energy of only 0.021

eV/atom (49 kJ/mol of LLZO) at 0 V among all solid electrolyte materials examined (Table 3.1). Given such small reaction energy, the Li reduction of garnet is likely to be kinetically inhibited, and the reduction products of Li_2O, Zr_3O and La_2O_3 (Table 3.1) may provide passivation to the material. These explain the widely reported 0 - 5 V window of garnet from the CV measurements in the literature.[5,57] The reduction of garnet at 0.05 V forms Zr_3O (Fig. 3.1), following another plateau at 0.004 V to form Zr based on the DFT GGA energies. Since these small values of energy and voltage is beyond typical accuracy of DFT and the approximations of the scheme, it is inconclusive whether the garnet LLZO is reduced to Zr_3O or Zr at 0 V or against Li metal. Nevertheless, the formation of Zr would be thermodynamically favorable at a potential significantly lower than 0 V, which corresponds to applying high current density at the Li-LLZO interface. Recent report of instability of garnet against Li at elevated temperatures of 300 °C may be an indication of the limited stability of garnet against Li metal,[58] as the diffusion and phase nucleation are facilitated at high temperatures.

3.2 Stability of Solid Electrolyte Materials under High Potentials

The oxidation reactions of the solid electrolyte materials were investigated using the same method. The LGPS material is delithiated and oxidized starting at 2.42 V (Fig. 3.1), and the final oxidation products of P_2S_5, GeS_2, and S are formed at the equilibrium oxidation potential of 2.48 V (Table 3.2). The oxidation potential of the LGPS is confirmed by the CV experiment.[14] Similar to Li_2S, all sulfide solid electrolytes such as Li_3PS_4, Li_4GeS_4, $Li_7P_3S_{11}$, and $Li_7P_2S_8I$ are oxidized at ~ 2.5 V to form S (Table 3.2). The other elements, such as P and Ge, are usually oxidized into P_2S_5 and GeS_2, respectively. The oxidation

reactions of sulfide solid electrolytes are highly favorable at 5 V as described by the decomposition energy (Table 3.2).

Table 3.2. Oxidation reaction of the solid electrolyte materials at 5 V.

	Phase equilibria at 5V	E_D (eV/atom)
Li_2S	S	-1.77
LGPS	GeS_2, P_2S_5, S	-1.04
Li_3PS_4	S, P_2S_5	-0.97
Li_4GeS_4	GeS_2, S	-1.12
$Li_7P_3S_{11}$	S, P_2S_5	-0.90
Li_6PS_5Cl	P_2S_5, S, PCl_3	-1.27
$Li_7P_2S_8I$	P_2S_5, S, I_2	-1.00
LiPON	PNO, P_2O_5, N_2	-0.69
LLZO	O_2, La_2O_3, $La_2Zr_2O_7$	-0.53
LLTO	O_2, TiO_2, $La_2Ti_2O_7$	-0.15
LATP	O_2, TiP_2O_7, $Ti_5P_4O_{20}$, $AlPO_4$	-0.065
LAGP	$Ge_5O(PO_4)_6$, GeP_2O_7, $AlPO_4$, O_2	-0.056
LISICON	Zn_2GeO_4, GeO_2, O_2	-0.57

Oxide solid electrolyte materials have higher oxidation potential than sulfides. The oxidation of LLZO, LISICON, and LLTO starts at 2.91, 3.39, and 3.71 V, respectively. The NASICON materials, LATP and LAGP, show the best resistance to oxidation with the highest oxidation potential of 4.21 and 4.28 V, respectively (Fig. 3.1), and the lowest decomposition energy of only ~ -0.06 eV/atom at 5 V (Table 3.2). The delithiation reactions continue at higher voltages, and the O_2 gas release during the oxidation at high voltages for all oxide solid electrolytes (Table 3.2). The oxidation of these solid electrolyte materials is

not surprising, given that Li_2O is oxidized at 2.91 V and that the O_2 gas is released by the further oxidation of Li_2O_2. LiPON starts oxidation at 2.63 V with the N_2 gas release. Our computation results are consistent with the experiments by Yu *et al.*[12], in which the onset of LiPON oxidation at ~2.6 V in the I-V measurements and the micro-sized gas bubbles in the LiPON material were observed after applying a high voltage of 6 V.

A significant overpotential to the calculated thermodynamic equilibrium potential is expected for the oxidation reaction processes, which are likely to have a slow kinetics. The kinetic limitations of the oxidation reactions may come from multiple aspects. Most decomposition products at high voltages (Table 3.2) are electronic insulating, and the diffusion of non-Li elements is usually slow in solids. Furthermore, the nucleation and release of O_2 and N_2 gas molecules are likely to have sluggish kinetics. For example, a significant overpotential of > 1 V is often observed in the oxygen evolution reactions in metal-air batteries.[59] Therefore, the overpotential of the decomposition reactions may provide a higher nominal oxidation potential of > 5 V and a wider nominal electrochemical window observed in the CV experiments.[1,9,11,12]

3.3 Chemical Stability of the Solid Electrolyte against non-Li Elements

In addition to the equilibrium of Li (and ϕ) evaluated in section 3.1-3.2, the equilibrium of non-Li elements such as Co, O and S should also be achieved between the solid electrolyte and the electrode, though non-Li elements are usually less mobile than Li/Li^+ in the solid electrolyte and electrode materials. The equilibria evaluated in this section correspond to chemical stability instead of the electrochemical stability, although the same scheme is used to evaluate electrochemical stability as in section 3.1

and 3.2. The μ_O stability window of LCO and $L_{0.5}CO$ electrode materials (Fig. 3.2a) corresponds to the range of possible μ_O values in the cathode material at the discharged and charged states, respectively. The oxide SEs, such as LLZO, LLTO, and LATP, have the μ_O window overlapping with those of LCO and $L_{0.5}CO$ (Fig. 3.2a). This overlapping of the μ_O window suggests that a common value of μ_O could be achieved across the interface of solid electrolyte and LCO/$L_{0.5}CO$ materials where the equilibrium μ_O is in the stable window for both materials.

Table 3.3. Phase equilibria of the solid electrolyte and $LiCoO_2$(LCO) /$Li_{0.5}CoO_2$($L_{0.5}CO$) materials at different chemical potential of O and S, respectively.

	anion μ (eV)	Corresponding environment	Decomposition products	ΔE_D^{open} (eV/atom)
LGPS	μ_O = -0.73	O-poor limit of $L_{0.5}CO$	GeP_2O_7, SO_3, Li_2SO_4	-3.68
	μ_O = -2.64	O-poor limit of LCO	$LiPO_3$, S, GeS_2, Li_2SO_4	-0.28
	μ_O = -3.00	Oxidation onset	Li_4GeS_4, S, Li_3PO_4	-0.02
Li_3PS_4	μ_O = -0.73	O-poor limit of $L_{0.5}CO$	$LiPO_3$, SO_3, Li_2SO_4	-3.73
	μ_O = -2.64	O-poor limit of LCO	$LiPO_3$, S, Li_2SO_4	-0.24
	μ_O = -3.00	Oxidation onset	Li_3PO_4, S	0
$LiPON_{0.14}$	μ_O = -0.73	O-poor limit of $L_{0.5}CO$	$LiNO_3$, Li_3PO_4, $Li_4P_2O_7$	-0.09
	μ_O = -2.64	O-poor limit of LCO	N_2, Li_3PO_4, $Li_4P_2O_7$	-0.02
	μ_O = -4.08	Oxidation onset	Li_2PO_2N, Li_3PO_4, LiN_3	0
$LiPON_{0.46}$	μ_O = -0.73	O-poor limit of $L_{0.5}CO$	$LiNO_3$, Li_3PO_4, $Li_4P_2O_7$	-0.36
	μ_O = -2.64	O-poor limit of LCO	N_2, Li_3PO_4, $Li_4P_2O_7$	-0.11
	μ_O = -4.08	Oxidation onset	Li_2PO_2N, Li_3PO_4, LiN_3	0
LCO	μ_S = -1.24	S-poor limit of LGPS	Co_9S_8, Li_2SO_4	-0.28
	μ_S = -2.72	Decomposition onset of LCO	CoO, Li_6CoO_4, Li_2SO_4	0
$L_{0.5}CO$	μ_S = -1.24	S-poor limit of LGPS	Co_9S_8, $CoSO_4$, Li_2SO_4	-0.40
	μ_S = -7.35	Decomposition onset of $L_{0.5}CO$	Li_2SO_4, Co_3O_4, $LiCoO_2$	-0.03

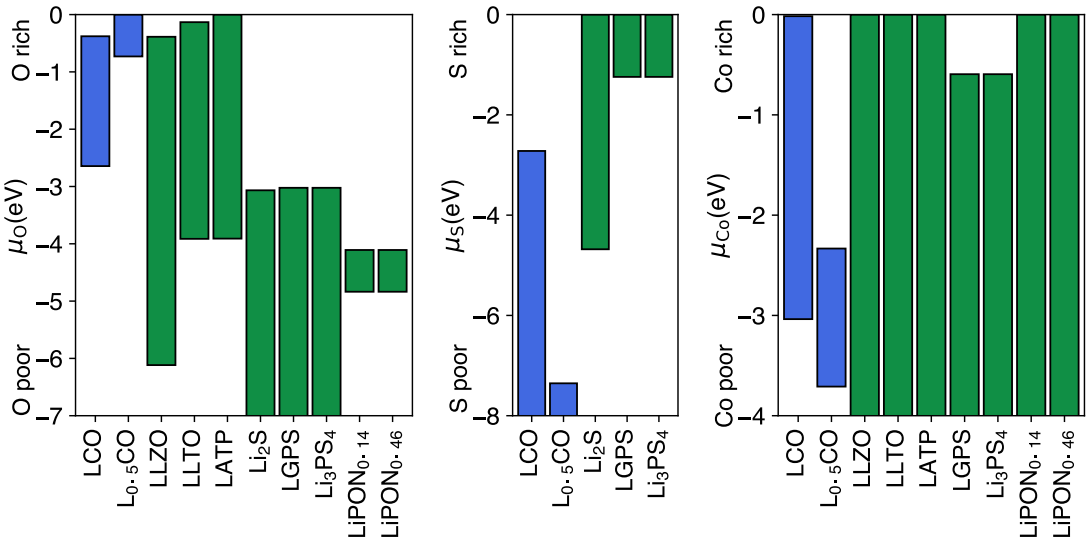

Figure 3.2. The stability window of solid electrolyte and electrode $LiCoO_2$/$Li_{0.5}CoO_2$ ($LCO/Li_{0.5}CO$)with respect to the chemical potential of (a) O, (b) S, and (c) Co.

In contrast, the μ_O windows of the sulfide solid electrolytes, LGPS and Li_3PS_4, have a significant gap with those of LCO and $L_{0.5}CO$ (Fig. 3.2a). Therefore, no common value of μ_O at the interface can simultaneously satisfy the μ_O equilibrium criterion between sulfide SEs and LCO materials. The equilibrium μ_O would be beyond the stability window of one or both materials, which would decompose simultaneously as a result. The μ_S stability window of the sulfide solid electrolytes does not overlap with that of $LCO/L_{0.5}CO$ either (Fig. 3.2b). These gaps of μ_O and μ_S windows suggest that the sulfide SE–LCO interfaces cannot satisfy the criteria (criterion 2 in Chapter 2) for the equilibrium of S and O across the interface. The high μ_O of the $LCO/L_{0.5}CO$ tends to oxidize LGPS and Li_3PS_4 into phases including Li_3PO_4 and Li_2SO_4, and the high μ_S of sulfide solid electrolytes tends to reduce LCO into phases including cobalt sulfides (Fig. 3.2 and Table 3.3). The reactions between sulfide electrolytes and LCO cathode material are highly thermodynamically favorable (Table 3.3), and the

formation of interphase layer has been reported in several experimental studies.[46,60] The observed distribution of Co and S across the interface, which was previously interpreted as the mutual diffusion of S and Co,[46] is likely the formation of cobalt sulfides interphase layer. Similar to sulfides, LiPON also has a μ_O window gap with LCO (Fig. 3.2a), but its decomposition energy is significantly smaller than sulfide solid electrolytes (Table 3.3).

The μ_{Co} stability windows of LCO and $L_{0.5}CO$ overlap with all solid electrolytes investigated, suggesting that the equilibrium of Co can be achieved at the interface without going beyond the μ_{Co} window of the SE or LCO materials. This result suggests that the incompatibility between sulfide SE and LCO are mostly originated from the discrepancy of O and S anion chemistries rather than that of Co. The distribution and mutual diffusion of Co across the interfaces observed in the previous EDX experiments[46] are likely due to the formation of decomposition interphases such as cobalt sulfides.

3.4 Chemical Stability of the Solid Electrolyte-cathode Interfaces

The equilibria with respect to only one element evaluated in above sections correspond to physical situations where only one mobile Li reaches equilibrium. Full thermodynamic equilibria evaluated in this section allow the simultaneous equilibria with respect to all elements and describe the chemical stability of the SE–electrode interfaces. The chemical stability of the interface evaluated in this section is about whether two materials would react exothermically without any applied voltage. This chemical stability of the interface is important for the heat treatment and sintering during the cell preparation.

Table 3.4. The phase equilibria and decomposition energies of the SE–LCO and SE-$L_{0.5}CO$ interfaces.

C_{SE}	$C_{Cathode}$	x_m	Phase equilibria at x_m	$\Delta E_{D,min,mutual}$ (meV/atom)	$\Delta E_{D,min,total}$ (meV/atom)
LGPS	LCO	0.42	Co_9S_8, Li_2S, Li_2SO_4, Li_3PO_4, Li_4GeO_4	-340	-349
	$L_{0.5}CO$	0.40	Co_9S_8, Li_2S, Li_2SO_4, Li_3PO_4, Li_4GeO_4	-499	-527
Li_3PS_4	LCO	0.41	Co_9S_8, Li_2S, Li_2SO_4, Li_3PO_4	-405	-405
	$L_{0.5}CO$	0.39	Co_9S_8, Li_2S, Li_2SO_4, Li_3PO_4	-564	-584
$LiPON_{0.14}$	LCO	0.93	CoN, Li_3PO_4, Li_6CoO_4, N_2	-35	-35
	$L_{0.5}CO$	0.59	Co_3O_4, LCO, $LiNO_3$, Li_3PO_4	-65	-65
$LiPON_{0.46}$	LCO	0.81	CoN, Li_2O, Li_3PO_4	-99	-99
	$L_{0.5}CO$	0.62	CoO, LCO, Li_3PO_4, N_2	-154	-154
LLZO	LCO	0.96	La_2O_3, $Li_6Zr_2O_7$, Li_5CoO_4	-1	-8
	$L_{0.5}CO$	0.47	La_2O_3, $La_2Zr_2O_7$, $Li_7Co_5O_{12}$, O_2	-39	-60
LLTO	LCO	0.64	Co_3O_4, $La_2Ti_2O_7$, Li_2TiO_3, $L_{0.5}CO$	-0.5	-44
	$L_{0.5}CO$	-	LLTO, $L_{0.5}CO$ (stable)	0	-
LATP	LCO	0.32	$L_{0.5}CO$, Co_3O_4, Li_3PO_4, $LiAl_5O_8$, TiO_2	-53	-63
	$L_{0.5}CO$	-	LATP, $L_{0.5}CO$ (stable)	0	-

Our calculations found that the interfaces between sulfide solid electrolytes and LCO/$L_{0.5}CO$ cathode are not thermodynamically stable (Table 3.4 and Fig. 3.3). The mutual reactions of LGPS with LCO and $L_{0.5}CO$ have favorable decomposition energies $\Delta E_{D,min,mutual}$ of -340 and -499 meV/atom, respectively. Similarly, the decomposition

energies of Li_3PS_4 with LCO and $L_{0.5}CO$ are -405 and -564 meV/atom, respectively. The phase equilibria of both interfaces include the formation of Co_9S_8, Li_2SO_4, and Li_3PO_4. The formation of cobalt sulfides at the interface between LCO and Li_2S-P_2S_5 electrolyte was reported in the experiments.[46] This reaction corresponds to a valence change of Co from 3+ to 2+. The cobalt sulfide phases with lower valences are known to be electronically conductive,[61] which are detrimental to the stability of the interfaces.[15] In addition, the mutual reaction energies for both LGPS and Li_3PS_4 with $L_{0.5}CO$ are lower than those with LCO, indicating larger thermodynamic driving force for the interfacial decomposition reactions at the charged state of the battery.

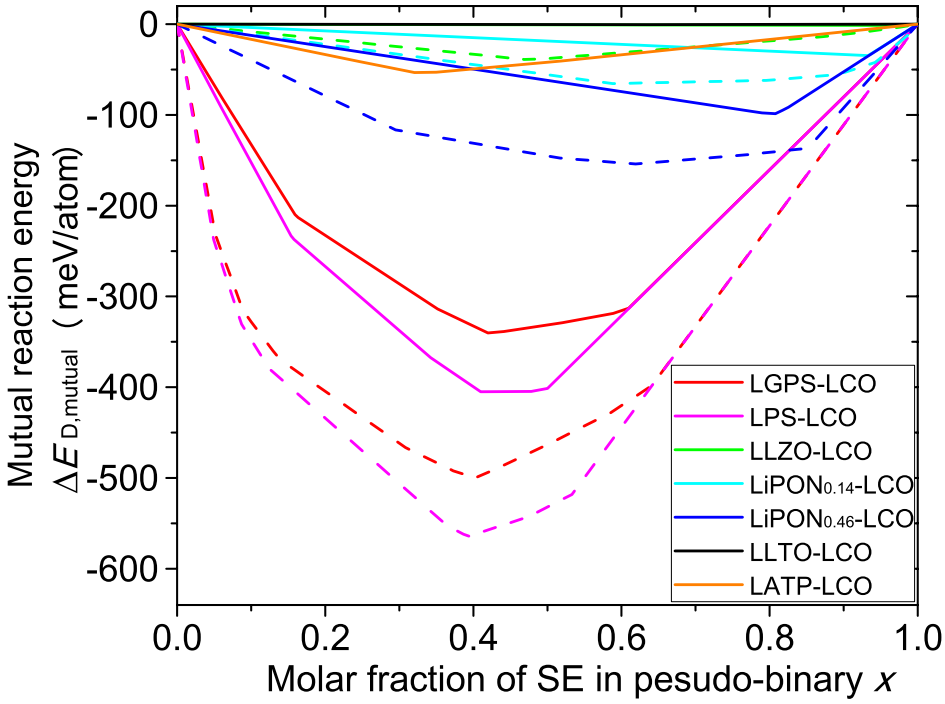

Figure 3.3. Calculated mutual reaction energy $\Delta E_{D,mutual}$ of SE–LCO (solid lines) and SE-$L_{0.5}CO$ (dashed lines) interfaces. The mutual reaction energy of LLZO–LCO, LLTO–LCO, LLTO-$L_{0.5}CO$, and LATP-$L_{0.5}CO$ have zero or near-zero values (minimum values provided in Table 4), which overlap at $\Delta E_{D,mutual} = 0$.

The interfaces between LCO cathode and oxide solid electrolytes have significantly better chemical stability with $\Delta E_{D,min,mutual}$ of zero to tens of meV/atom compared to the sulfide electrolytes (Table 3.4 and Fig. 3.3). For example, the minimum reaction energy $\Delta E_{D,min,mutual}$ of garnet LLZO with LCO and $L_{0.5}CO$ are only -1 and -39 meV/atom, respectively. In addition, LLTO and LATP (Table 3.3 and Fig. 3.4) are thermodynamically stable against the charged state cathode $L_{0.5}CO$, and their interfaces with LCO have small decomposition energies $\Delta E_{D,min,mutual}$ of only -1 and -53 meV/atom, respectively. The interfacial decomposition reactions may be kinetically inhibited. The good stability of LLTO and LLZO against LCO has been observed in the experiments.[42,62] However, the sintering of the interfaces at high temperature may enhance the formation of the interphase layers.[63] The main decomposition products of LLZO-$L_{0.5}CO$ interface include La_2O_3, $La_2Zr_2O_7$, O_2 (Table 3.4), which are similar to the delithiation products of garnet LLZO at high voltage (Table 3.2). The decomposition of the LLZO-$L_{0.5}CO$ interface is mainly due to the delithiation of the LLZO by $L_{0.5}CO$. Our predicted phase equilibria at the LATP–LCO interface includes Co_3O_4, which is also observed as a reaction product at LCO-LATP interface in an experimental study.[64] The formation of Co_3O_4 and $L_{0.5}CO$ corresponds to the Co valence increase from 3+ to 4+. The increase of Co valence at oxide solid electrolyte interfaces is opposite from that at the sulfide solid electrolyte interfaces, indicating the different nature of interfacial decompositions and the resulting properties between oxide and sulfide solid electrolytes. In addition, the decomposition interphase layers including Li_3PO_4 and $LiAl_5O_8$ can potentially passivate the interface and provide decent Li ionic conductivity across the interface.[65] In summary, the oxide solid electrolyte materials, LLZO, LLTO, and LATP, have significantly better chemical compatibility with

the LCO cathode materials compared to sulfide solid electrolytes.

LiPON also shows thermodynamically favorable reactions with LCO and $L_{0.5}CO$ (Table 3.4 and Fig. 3.3). The phase equilibria and decomposition energy are highly dependent on the LiPON composition. At low N content of 0.14, the mutual reaction energy $\Delta E_{D,min,mutual}$ of LiPON is only -35 and -65 meV/atom against LCO and $L_{0.5}CO$, respectively. At higher nitrogen content of 0.46, the minimum mutual reaction energies with LCO and $L_{0.5}CO$ of -106 and -153 meV/atom, respectively, indicate more favorable decompositions. The LCO chemical compatibility of LiPON is better than sulfide solid electrolytes but worse than oxide solid electrolytes. The formation of an interphase layer and the change of chemical structures at the LiPON/$LiCoO_2$ interfaces were observed by *in situ* XPS experiments.[66] The good compatibility of the LiPON with the LCO cathode material observed in the experiments[67-70] may be explained by the effect of the interphase layers, including Li_3PO_4, which is a well-known coating material for cathode[71-73] and is the dominant decomposition product at the LiPON interfaces.

3.5 Electrochemical Stability of the Solid Electrolyte-Cathode Interfaces

In this section, we evaluated the phase equilibria of the solid electrolyte–LCO interfaces at the applied potential ϕ on the basis of the equilibrium criterion 4 (section 2.5). These phase equilibria correspond to the interphase evolution, such as lithiation or delithiation, in response to the applied potential, and the interfacial decomposition described by the reaction energies may become more favorable at certain applied potentials. The interface between LCO and Li_3PS_4 was found to have poor stability over the entire range of the applied voltage from 2 to 5 V. The interfacial mutual reaction energy $\Delta E^{\text{open}}_{\text{D,min,mutual}}$ is

in the range of [-737, -594] meV/atom for LPS from 2 to 5 V (Fig. 3.4 and Table 3.5). The total decomposition energy $\Delta E_{\mathrm{D,min,total}}^{\mathrm{open}}$ of LGPS or Li_3PS_4 reaches -1.25 eV/atom at 5 V (Fig. 3.4), suggesting highly favorable decompositions at high voltages. Previous experimental studies also reported the formation of interphases of tens nanometers including cobalt sulfides between LCO and Li_2S-P_2S_5 SE after charging.[46] The growing differences between $\Delta E_{\mathrm{D,min,mutual}}^{\mathrm{open}}$ and $\Delta E_{\mathrm{D,min,total}}^{\mathrm{open}}$ at higher voltages (Fig. 3.4) are mainly due to the increasing contribution from the delithiation of the SEs to the total decomposition energy $\Delta E_{\mathrm{D,min,total}}^{\mathrm{open}}$.

The oxide solid electrolytes–LCO interfaces generally have significantly better stability than the sulfide SEs during the whole voltage range. For example, the LLZO–LCO interface has the minimum interfacial mutual reaction energy $\Delta E_{\mathrm{D,min,mutual}}^{\mathrm{open}}$ of only -33 meV/atom (Table 3.5). At high voltage above 4 V, the reaction products, $La_2Zr_2O_7$ and $LaCoO_3$, are likely poor Li ionic conductor materials. The predicted phase $LaCoO_3$ was observed experimentally for the LLZO–LCO interface after the heat treatment of over 1000 °C,[74] which causes Li loss similar to the delithiation at high voltage. In addition, $LaCoO_3$ may be electronic conductive,[75] leading to the formation of thick interphase layers and potential degradation at the interface. However, the final phase equilibria of the interface at high voltage involve O_2 gas release, which is likely to have poor kinetics as in the oxygen evolution reactions in Li-air batteries. A significant amount of overpotential, yielding high oxidation potential observed in many CV experiments, is expected for such oxidation reactions. Similarly, the LCO interfaces with LLTO and LATP show good stability with zero mutual reaction energy $\Delta E_{\mathrm{D,min,mutual}}^{\mathrm{open}}$ at voltage higher than 3.34 V and 4.53 V,

respectively (Fig. 3.4 and Appendix). The good electrochemical stability of the interfaces between LLTO/LATP and LCO at high voltages may partly due to high oxidation potential (anodic limit) of these solid electrolytes and the good chemical stability between the solid electrolytes and LCO cathode.

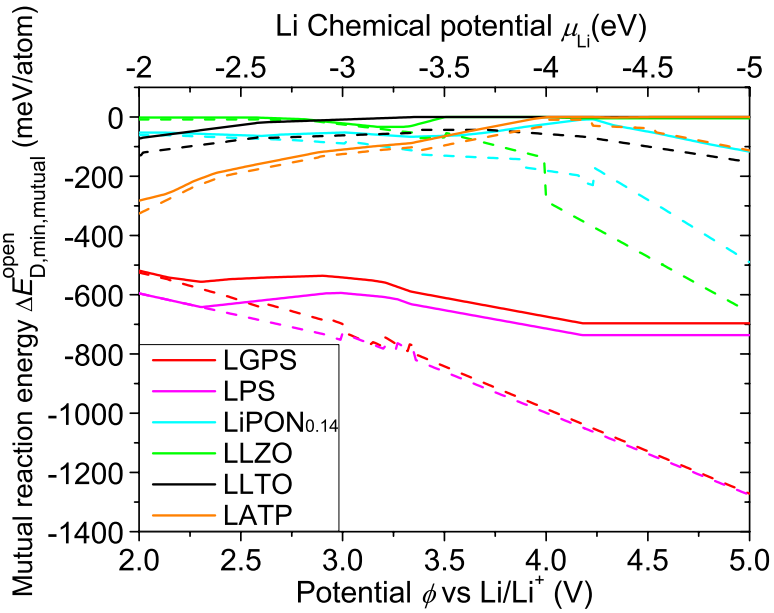

Figure 3.4. The mutual reaction energy $\Delta E^{open}_{D,min,mutual}$ (solid lines) and the total reaction energy $\Delta E^{open}_{D,min,total}$ (dashed lines) at the SE–LCO interfaces under applied potential ϕ in a 2 V – 5 V range.

The mutual reaction energy of the $LiPON_{0.14}$–LCO interface is comparable to oxide SEs, though $LiPON_{0.14}$ reacts favorably with LCO in the whole 2 V- 5 V range (Fig. 4 and Table 5). The formation of Li_3PO_4 interphase and the small decomposition energy may explain the widely observed stability of LiPON with LCO.[67-69,76] The interfacial reaction between LiPON and LCO also involves N_2 and O_2 gas release at above 4.23 V, respectively. The void formation at LiPON–$LiCoO_2$ interface after battery cycling was reported in an *in-situ* TEM experimental study.[69]

Table 3.5. Phase equilibria and decomposition energy of SE–LCO interfaces under applied potential ϕ.

Interface	Applied potential ϕ (V)	Phase equilibria at $x = x_m(\phi)$ under ϕ	$\Delta E^{open}_{D,min,mutual}$ (meV/atom)	$\Delta E^{open}_{D,min,total}$ (meV/atom)
Li_3PS_4–	2.00 - 2.91	Co_3S_4, Li_2SO_4, Li_3PO_4	[-641, -596]	[-737, -596]
LCO	2.91 - 2.99	Co_3S_4, Li_2SO_4, $Li_4P_2O_7$	[-596, -594]	[-750, -737]
	2.99 - 3.20	Co_3S_4, Li_2SO_4, $LiCoPO_4$	[-607, -594]	[-779, -730]
	3.20 - 3.26	Co_3S_4, Li_2SO_4, $Co_3(PO_4)_2$	[-613, -608]	[-785, -773]
	3.26 - 5.00	Co_3S_4, $CoSO_4$, $Co_3(PO_4)_2$	[-737, -616]	[-1273, -763]
LLZO–	2.00 - 2.57	La_2O_3, $Li_6Zr_2O_7$, Li_5CoO_4	[-2, -2]	[-9, -9]
LCO	2.57 - 2.81	La_2O_3, $Li_6Zr_2O_7$, $Li_7Co_5O_{12}$	[-7, -2]	[-13, -8]
	2.81 - 3.50	La_2O_3, $La_2Zr_2O_7$, $Li_7Co_5O_{12}$	[-33, -2]	[-72, -11]
	3.50 - 3.99	La_2O_3, $La_2Zr_2O_7$, O_2, $L_{0.5}CO$	0	[-137, -53]
	3.99 - 5.00	$LaCoO_3$, $La_2Zr_2O_7$, O_2	[-5, 0]	[-656, -284]
$LiPON_{0.14}$–	2.00 - 2.12	CoN, N_2, Li_3PO_4	[-53, -53]	[-55, -55]
LCO	2.12 - 2.70	CoO, N_2, Li_3PO_4	[-64, -53]	[-70, -55]
	2.70 - 3.01	Co_3O_4, N_2, Li_3PO_4	[-59, -53]	[-84, -70]
	3.01 - 3.89	Co_3O_4, $LiNO_3$, Li_3PO_4	[-67, -35]	[-139, -77]
	3.89 - 4.16	$LiCoPO_4$, $LiNO_3$, Li_3PO_4	[-33, -11]	[-190, -165]
	4.16 - 4.18	$LiCoPO_4$, $LiNO_3$, $Li_4P_2O_7$	[-9, -9]	[-221, -221]
	4.19 - 4.23	$CoPO_4$, $LiNO_3$, $Li_4P_2O_7$	[-9, -8]	[-221, -215]
	4.23 - 4.54	$CoPO_4$, $LiNO_3$, O_2	[-53, -9]	[-288, -169]
	4.54 - 5.00	$CoPO_4$, $Co(NO_3)_4$, O_2	[-116, -56]	[-482, -294]

Our results show that the stability of the interface and the formed phase equilibria are dependent on the applied potential, as the delithiation at high voltages provides additional thermodynamic driving force for the interfacial decompositions. Among the SE–LCO interfaces investigated, the interfaces of the SEs (such as oxides) that have good electrochemical window and good chemical stability with the electrode in general show better stability during electrochemical cycling. Therefore, the SE with a wide electrochemical window and the good chemical stability with electrodes are desired to achieve intrinsic interface stability during electrochemical cycling. For those SE (such as sulfides) and interfaces that cannot satisfy the above criteria, an interfacial coating layer material can be applied to resolve the stability problems at the interface.

3.6 Improved Interfacial Stability by Applying Coating Layers

Currently, the interfacial resistance has become a critical problem for the performance of all-solid-state Li-ion batteries. Engineering of the interface, such as the application of interfacial coating layers, is used to improve interfacial protection and to reduce interface resistance. In this section, we investigated the electrochemical stability of the coating layer materials, such as $Li_4Ti_5O_{12}$,[77,78] $LiTaO_3$,[79] $LiNbO_3$,[80,81] Li_2SiO_3,[82] and Li_3PO_4,[83] which were demonstrated to suppress the mutual diffusion of non-Li elements and to reduce the interfacial resistance at the solid electrolyte-cathode interfaces in all-solid-state Li-ion batteries.[2,44,46,79]

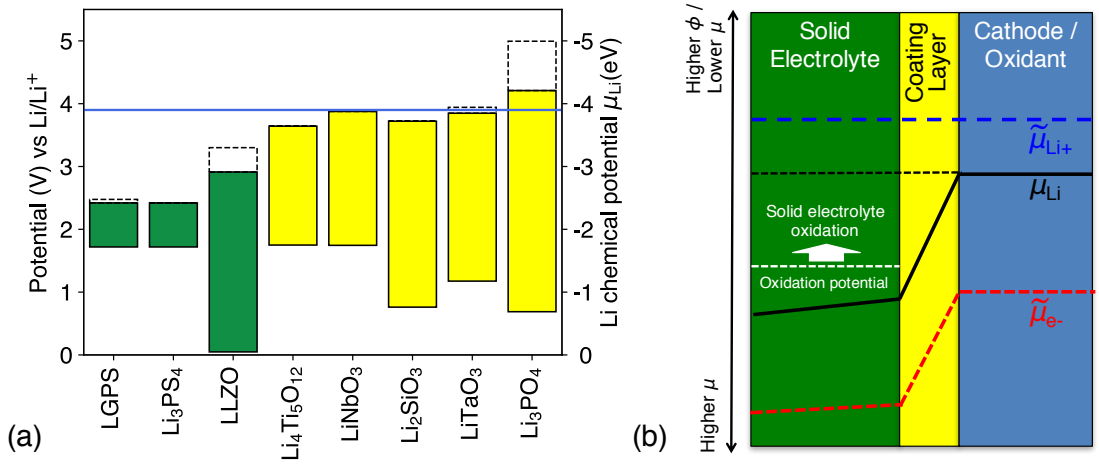

Figure 3.5. (a) Electrochemical stability window (color bars) of commonly used coating layer materials. The oxidation potential to fully delithiate the material is marked by the dash line. The blue solid line at 3.9 V represents the equilibrium voltage of the $LiCoO_2$ cathode material. (b) Schematic diagram of Li chemical potentials μ_{Li} (black line) and the electrochemical potential $\tilde{\mu}_{Li+}$ (blue dashed line) and $\tilde{\mu}_{e-}$ (red dashed line) across the solid electrolyte-cathode interface.

Our calculations show that these coating layer materials have an electrochemical window from the reduction potential of 0.7-1.7 V to the oxidation potential of 3.7-4.2 V (Fig. 3.5a). Therefore, the coating layer materials are stable between 2 V to 4 V, the usual voltage range during the cycling of Li-ion batteries. In addition, the coating layers materials have poor electronic conductivity and can serve as artificial SEIs to passivate the solid electrolyte (Fig. 3.5b). Given that the sulfide solid electrolyte materials are oxidized at as low as 2.5 V and are not thermodynamically stable at the voltage of 4 V, the coating layers serve as critical passivation through the passivation mechanism. The coating layers mitigate the low Li chemical potential μ_{Li} from the cathode material applied on the solid electrolyte

materials. As a result, the oxidation and delithiation of the solid electrolyte at the cathode interface is stopped, and the oxidation potential (anodic limit) of the solid electrolyte is extended by the artificial coating layer. Therefore, the coating layer effectively extended the anodic limit of the sulfide solid electrolyte from ~2.5 V to ~4 V. The overpotential to oxidize the coating layers may further extend the nominal stability window. Similar strategy of applying artificial coating layers has been employed at the anode side for the protection and stabilization of Li metal anode. For example, Polyplus[84] has applied coating layers between Li metal and LATP electrolyte to protect the LATP materials against Li metal. The passivation mechanism of the coating layer at the anode side is the same as the decomposition interphase demonstrated in section 3.1.

Table 3.6. The mutual reaction energy $\Delta E_{D,min,mutual}$ (in meV/atom) of the coating layer materials with the SE or LCO materials.

	Li_3PS_4	LLZO	LCO	$L_{0.5}CO$
$Li_4Ti_5O_{12}$	-80	-75	-1	0
$LiNbO_3$	-155	-76	0	0
Li_2SiO_3	-19	-29	0	0
$LiTaO_3$	-49	-68	0	0
Li_3PO_4	0	0	0	0

The coating layer material lying between the original SE–LCO interfaces forms two new interfaces with the SE and LCO, respectively. By applying the same computational scheme as in section 2.4, we investigated interfacial chemical compatibility of these two interfaces with the coating layer. The previously demonstrated coating layer materials, such as $Li_4Ti_5O_{12}$, $LiTaO_3$, $LiNbO_3$, Li_2SiO_3, and Li_3PO_4, have excellent chemical stability with

the LCO and $L_{0.5}CO$ with zero or negligible decomposition energy $\Delta E_{D,min,mutual}$ (Table 3.6). In addition, all coating layer materials show relatively better stability with the sulfide SE comparing to the original sulfide SE–LCO interfaces, which have the interfacial reaction energy $\Delta E_{D,min,mutual}$ of ~ -500 meV/atom. As a result, the interface with the coating layer has significantly improved stability and suppresses the formation of thick interphase layer. This result of the coating layer was observed as reduced mutual diffusion across the interface in the experiments.[77,79,82] In addition to stabilizing the interface, the coating layer of only a few nanometers is significantly thinner than the decomposition interphase layer of ~10 to 100 nm. The reduced thickness of the coating layer may significantly reduce the high interfacial resistance caused by the thick decomposition interphase layer.

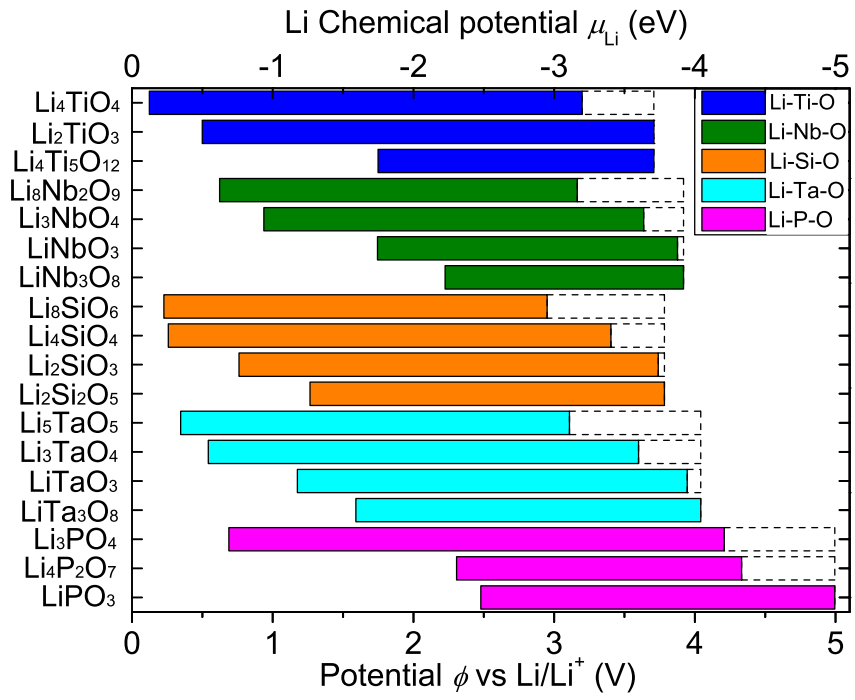

Figure 3.6. Electrochemical window of potential coating layer materials. The dashed box marks the equilibrium voltage to fully delithiate the materials.

Table 3.7. The mutual reaction energy $\Delta E_{\mathrm{D,min,mutual}}$ (in meV/atom) of the coating layer materials with the SE or LCO materials.

	Li_3PS_4	LLZO	LCO	$L_{0.5}CO$
Li_4TiO_4	-125	0	0	-30
Li_2TiO_3	-75	-5	0	0
$Li_8Nb_2O_9$	-147	0	0	-20
Li_3NbO_4	-132	-4	0	0
$LiNb_3O_8$	-173	-115	-16	0
Li_8SiO_6	-177	0	-3	-50
Li_4SiO_4	-81	-1	0	-12
$Li_2Si_2O_5$	-10	-69	-4	0
Li_5TaO_5	-117	0	0	-32
Li_3TaO_4	-64	-3	0	0
$LiTa_3O_8$	-64	-105	-22	0
$Li_4P_2O_7$	-9	-101	-44	-3
$LiPO_3$	-32	-201	-76	-19

In addition, we also computationally investigated other compounds (listed in Fig. 3.6 and Table 3.7) based on the same cations, such as Ti, Nb, Si, Ta, and P, as potential coating layer materials. All these lithium metal oxide materials have a wide electrochemical window (Fig. 3.6). The compounds with higher Li content generally show lower reduction potential, and the compounds with lower Li content or higher O content show higher oxidation potential. Most of these compounds have excellent chemical stability against LCO

and $L_{0.5}CO$ cathode materials with zero or small $\Delta E_{\mathrm{D,min,mutual}}$ (Table 3.7).

All these coating layer materials significantly improve the stability of sulfide SE–LCO interfaces. The chemical stability between LLZO–coating layer interface varies significantly with the compositions of the coating layer materials. It is interesting to note that the coating layers that are the most stable with sulfide SE may not necessarily be the most stable ones with LLZO. For example, $LiNbO_3$, a demonstrated coating layer for sulfide SEs, is not as stable as Li_3NbO_4 and $Li_8Nb_2O_9$ with LLZO according to the decomposition energy $\Delta E_{\mathrm{D,min,mutual}}$ (Table 3.7). In the previous study, the application of Nb at the LLZO–LCO interfaces may form amorphous lithium niobates including $Li_8Nb_2O_9$ or Li_3NbO_4-like phases,[81] which stabilize the LLZO–LCO interface and hence reduce the interfacial resistance. Similarly, the other Li-rich coating layers, such as Li_4TiO_4, Li_2TiO_3, Li_8SiO_6, Li_4SiO_4, Li_5TaO_5, and Li_3TaO_4 may work better with LLZO than those previously demonstrated for sulfide SEs, such as $Li_4Ti_5O_{12}$, $LiTaO_3$, and Li_2SiO_3.

3.7 Critical Role of Interphases, Interface Types and Interfacial Engineering Strategies

Our thermodynamic analyses based on first principles calculations indicate that most solid electrolyte materials have limited electrochemical window. In contrast to the widely held perception about the outstanding stability of the solid electrolyte materials, the solid electrolyte materials are reduced and oxidized at low and high potentials, respectively, and are not thermodynamically stable against Li metal. The sulfide solid electrolytes based on thio-phosphates are reduced at ~1.6-1.7 V and oxidized at ~2.5 V. The stability window of oxide solid electrolytes varies greatly from one material to another. Although some

oxides have high reduction potential as sulfides, most oxide solid electrolytes have a significantly higher oxidation potential, and are not oxidized until > 3 V. In particular, the NASICON materials, LATP and LAGP, are thermodynamically stable up to ~4.2 V. Among all these oxides investigated, the Li garnet materials have the best resistance to Li reduction. Overall, the oxide solid electrolyte materials have significantly wider electrochemical window than sulfides. The reduction and oxidation potentials as well as the decomposition products of solid electrolytes predicted from our calculations are in good agreement with prior experimental studies, confirming that our computation method based on the Li grand potential phase diagram is a valid scheme in evaluating the electrochemical stability of materials.

Our calculation results demonstrated that the good stability of the solid electrolyte materials is originated from the kinetic stabilizations. First, the wide, nominal electrochemical window observed in many CV experiments can be partially attributed to the significant overpotential of the sluggish kinetics during the decomposition reactions (Fig. 3.7). The decomposition reactions though kinetically sluggish are still thermodynamically favorable at the applied overpotential and may happen over an extended period of time, leading to the deterioration of the batteries. This kinetic stabilization from the sluggish kinetics of the reactions is different from the passivation mechanisms. The passivation mechanism of the interphases is the origin of the outstanding stability in the solid electrolyte. The decomposition interphases with good stability and poor electronic transport are effectively the SEIs in the all-solid-state Li-ion batteries to passivate the solid electrolytes (Fig. 3.7). The interphases, which are stable against solid electrolytes and electrodes, mitigate the Li chemical potential discrepancy between the electrolyte and

electrode at the interfaces. As a result, the anodic/cathode limits and the electrochemical window of the solid electrolyte are significantly extended by the extra electrochemical window provided by the interphases (Fig. 3.6). The effective electrochemical window of the solid electrolyte materials is its own intrinsic electrochemical window plus the electrochemical window of the interphases (Fig. 3.7).

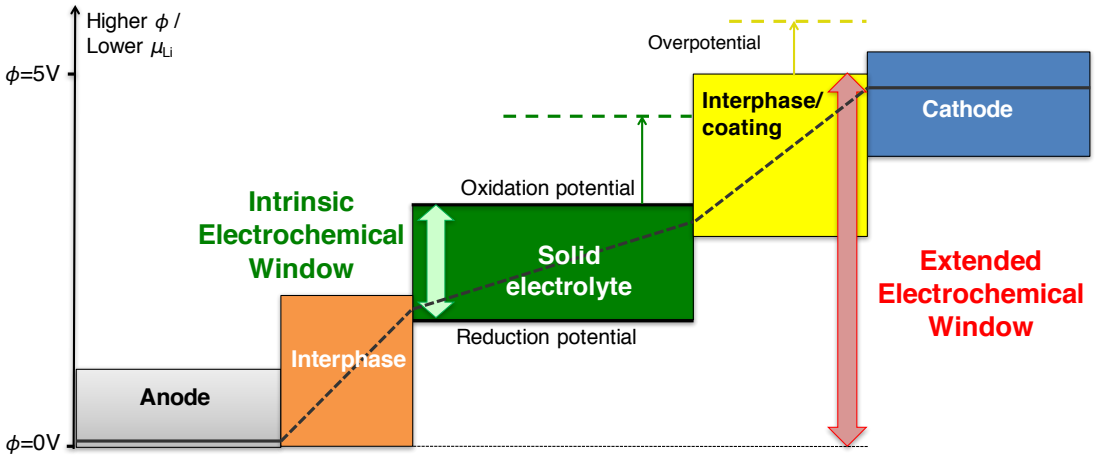

Figure 3.7. Schematic diagram of the electrochemical window (color bars) and the Li chemical potential profile (black line) in all-solid-state Li-ion battery. The profile of chemical potential is schematic in this plot and may not be linear. The high μ_{Li} in anode (silver) and low μ_{Li} in cathode (blue) are beyond the stability window of the solid electrolyte (green). The observed nominal electrochemical window is extended by the overpotential (dash line) and by the interphases (orange and yellow), which account for the gap of μ_{Li} between solid electrolyte and electrodes across the interfaces.

Our computational study revealed that the electrochemical and chemical stabilities of the solid electrolyte–electrode interfaces in the ASLiBs are intrinsically limited. Most solid electrolyte–electrode interfaces are not thermodynamically stable before, after, and during electrochemical cycling. In particular, the sulfide solid electrolytes are neither

chemically nor electrochemically stable against the LCO cathode, due to the anion chemical potential discrepancy between sulfide solid electrolytes and LCO. The oxide solid electrolytes have significantly better chemical and electrochemical stabilities with the LCO cathode than sulfide SEs. The interfacial reactions between oxide solid electrolyte and LCO, though may be kinetically limited, are also thermodynamically favorable, suggesting potential interfacial degradations after thermal processing or during battery cycling.

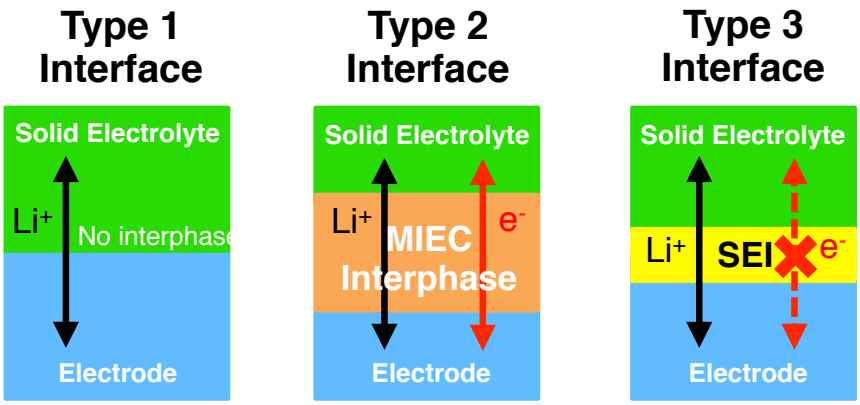

Figure 3.8. Schematic illustration of the three types of solid electrolyte–electrode interfaces. Type 1: ideal stable interface; Type 2: interface formed with interphase layers that are mixed ionic and electronic conductors (MIEC); Type 3: interfaces formed with stable solid-electrolyte interphase (SEI)

These results about the interfacial thermodynamics suggest the ubiquitous formation of the interphase layers at the solid electrolyte–electrode interfaces, which have significant implications for the research and development of the ASLiBs. The properties of these interphase layers would be critical to the performance of the ASLiBs. In particular, the distinctive chemistry nature of sulfide and oxide solid electrolytes lead to very different interphase properties for the SE–LCO cathode interfaces and hence require different interfacial engineering strategies. Following the definitions by Wenzel *et al.*,[18] we

distinguish three different types of interfaces based on the interface stability and interphase properties. (Fig. 3.8)

Type 1 interface - Stable interfaces with no decomposition or interphase layers.

Type 1 interfaces are either thermodynamically intrinsic stable or kinetically stabilized during the cycling voltage range. Type 1 interfaces do not have interphase layer between the solid electrolyte and electrode, and is expected to have decent interfacial ionic conductivity, because both the solid electrolyte and the electrode are good Li ionic conductors. However, our thermodynamic analyses demonstrated that few solid electrolyte materials have thermodynamically intrinsic stabilities against Li metal anode or high-voltage cathodes, or during the entire range of cycling voltages. Among five classes of SE materials investigated, LLTO and LATP have best electrochemical stability against LCO cathode materials at high voltages, and LLZO has the best stability against Li metal. Some oxide SEs may form kinetically stabilized Type 1 interfaces with the electrode materials,[42,62] though these Type 1 interfaces may still degrade and convert to other types during sintering or electrochemical cycling due to the limited thermodynamic stability. Type 1 interface requires the SEs with wide electrochemical window and good chemical compatibility with the electrode materials. Since the electrochemical window of the solid electrolytes and the chemical compatibility of the SE–electrode interfaces are limited, it is unrealistic to have a solid electrolyte with both Type 1 interfaces with Li metal anode and high-voltage cathode.

Type 2 interface - Interfaces formed with interphase layers that are mixed ionic and electronic conductors (MIEC).

The formation of the interphase layer between the solid electrolyte and the electrode is expected for most Li-SE and SE–LCO interfaces as suggested by the interfacial

thermodynamics results from our computation. The electronic conductivity of the interphase, regardless of specific electronic conductive mechanisms, determines whether the interface is Type 2 or Type 3. If the formed interphase is MIEC, the simultaneous transport of Li ions and electrons would enable continued decomposition reactions, which are thermodynamically favorable. Therefore, the MIEC interphases cannot provide essential passivation at the interface.[15] The examples of Type 2 interfaces include the Li-LGPS and Li-LLTO interfaces, which formed interphases including the electron-conducting Li-Ge alloys and lithium titanates, respectively. The formation of Type 2 interfaces in these materials explains the Li reduction of the LGPS and LLTO materials observed in the experiments.[14,85] The continued decomposition may result in poor coulombic efficiency in ASLiBs. Therefore, Type 2 interfaces, which may cause continued interfacial degradation and high interfacial resistance, should be avoided in the ASLiBs. The application of artificial coating layers can be used to engineer Type 2 interfaces into Type 3 interfaces.

Type 3 interface - Interfaces formed with stable solid-electrolyte interphase (SEI).

In contrast to Type 2 interfaces, the interphase layers in Type 3 interfaces are electronic insulating and are stable during the electrochemical cycling, acting as a stable SEI at the SE–electrode interfaces. Type 3 interfaces with spontaneously formed SEIs have self-limiting interfacial degradation. The SEIs passivate the SE materials and stop the continued decomposition into the bulk of the solid electrolyte.[15] The Li-LiPON interface is Type 3, where the formed interphases containing Li_2O, Li_3N, and Li_3P are electronic insulating.[15,45] In addition, the interphase decomposition layer, including fast Li-ion conducting Li_3N and Li_3P,[41,86] is likely to yield low interfacial resistance. The interfacial resistance of Type 3 interfaces is highly dependent on the ionic conductivity of the SEIs. The Li-LiPON interface

is an ideal Type 3 interfaces which have spontaneously formed SEIs with excellent ionic conductivity. For those Type 3 interfaces with poor Li-ion conducting SEIs, the application of a coating layer with good ionic conductivity as the artificial SEI may resolve the high resistance problem of the spontaneously formed SEIs.

We summarize the categorization of different combination of SE and electrode materials into the defined interface types (Fig. 3.8). Our discussion focuses on Li metal anode and LCO cathode materials (similar results are expected for other transition metal oxide cathodes), which are often desired for the ASLiBs. For Li-SE interfaces, Type 1 interfaces are rare due to the strong thermodynamic driving force for Li metal to reduce the solid electrolyte. The Li-LLZO interface may be Type 1 as a result of kinetically stabilization and small thermodynamic driving force for Li reduction. The high temperature treatment may facilitate the Li reduction of LLZO and formation of the interphase.[58] The Li-LiPON and Li-Li_3PS_4 are typical Type 3 interfaces, where the passivation layers of high Li ionic conductivity and poor electronic conductivity are formed. The Li-LGPS, Li-LLTO, and Li-LATP are typical Type 2 interfaces, where significant reduction of the SE is observed. Cations, such as Ti and Ge, in SEs would facilitate the formation of the Type 2 interfaces, because of the formation of the electronic conducting interphase layers at Li reduction. Therefore, the use of these cations should be avoided in the design of SE materials for Li metal compatibility. In contrast, anion mixing should be a viable strategy for the SE materials design to simultaneously improve stability and Li ionic conductivity. LiPON is a successful case of using oxynitride to achieve good stability and Li ionic conductivity. Similar successes have been demonstrated in the doping of Li_3PS_4 with halides, such as LiCl

and LiI.[54,87] Similarly, we expect some oxysulfide compounds as promising solid electrolytes.

The interfaces between the solid electrolyte and cathode, such as LCO, may be more complicated, due to a large number of elements involved and a wide range of Li chemical potential at the charged and discharge states of the battery. The sulfide SE–LCO interfaces may also be partially Type 2, because the interphases include the cobalt sulfide binaries such as Co_9S_8 or Co_3S_4, which are electronically conductive.[61,88] This formation of MIEC interphases may explain the large thickness of the interphase layers of 10-100 nanometers observed at these sulfide–LCO interfaces.[46] Thick interphase layers generally result in a high interfacial resistance. However, the decomposition does not happen to the entire bulk of SEs due to the limited diffusion of Co and the drop of the Co content inside the SEs. The part of the interphase at the direct adjacent of solid electrolyte is of low content of Co sulfides and is still passivating (Type 3), which stops the further growth of the interphase layers. The variation of the interphase composition across the interface has been observed in our computation (Appendix) and the EDX experiments.[60,82] Therefore, the sulfide SE-cathode interface is not strictly Type 2 (as in Li-LLTO) but rather a mixture of Type 2 and Type 3. Having some Type 2 features inside the interphase may have negative impact on the electrochemical performance of the ASLiBs. The enabled transport of both Li^+ and e^- through the MIEC interphase would facilitate the electrochemical cycling of these interphase layers during cycling voltages (as predicted in section 3.4). Active electrochemical cycling of these interphase layers may facilitate the growth of the decomposition interphase layers as a result of cyclic lithiation and delithation[14], which lead to repetitive volume change and the failure of the mechanical contact at the interface. Such

special interface properties may explain the poor cyclability of the ASLiBs. Therefore, the key problem of sulfide SE–LCO interfaces is the poor stability, which leads to thick interphase layers, high interfacial resistance, and degradation over cycling. Therefore, the application of the coating layer at these interfaces is the corresponding strategy to address the stability issue by turning the interfaces into a desired Type 3 interface with thin thickness and improved interfacial conductivity. The coating layers serve as artificial SEIs to stabilize the interface and to resolve the issue of poor interfacial conductivity.

In general, we found that the oxide SE and LCO interfaces may be Type 1 or Type 3. In particular, LLTO-$L_{0.5}CO$ and LATP-$L_{0.5}CO$ are thermodynamically stable as Type 1, and other oxide SE–LCO interfaces may be kinetically stabilized as Type 1. After the thermodynamically favorable decomposition between these materials, some oxide SE–LCO interfaces may turn into Type 3, because the interphases formed at oxides SE-cathode interfaces are mostly electronic insulating. However, such interphases and formed SEI layers in some Type 3 oxide solid electrolyte-cathode interfaces may have poor Li ionic conductivity, since most of the equilibrium phases have low or zero Li content as a result of the delithiation. For example, the spontaneous decomposition interphase, such as $La_2Zr_2O_7$, of LLZO–LCO interface are likely poor Li ion conductor. For these Type 3 interfaces, the key issue is not poor interfacial stability but the low ionic conductivity of the formed interphase layers. Therefore, interfacial engineering for the aforementioned Type 3 interfaces is also necessary to improve interfacial ionic conductivity. The increased interfacial conductivity after applying lithium niobate interphase layer in the previous study[81] may be due to the higher ionic conductivity of the coating layer than that of the spontaneous decomposition interphase. In addition, the soft and ductile Nb metal may

enhance the wetting and may promote the interfacial contact between the LLZO and LCO. As illustrated above, the categorization of different types of interfaces is critical to understand the problems at the interfaces and to apply corresponding interfacial engineering, which is the key to achieve desired interfacial properties and to improve electrochemical performance in ASLiBs.

Chapter 4. Strategies Based on Nitride Materials Chemistry to Stabilize Li Metal Anode

Li metal has been long desired as the anode material with the highest theoretical specific capacity and the lowest standard potential to significantly increase the energy density in rechargeable Li-ion battery.[89,90] Enabling Li metal anode has been regarded as the "Holy Grail" [91,92], but confronts many challenges. The undesired growth of Li dendrite during cell cycling causes short circuiting in the cell, leading to catastrophic cell failure and safety issues. In addition, Li metal is strongly reducing, and is not compatible with most electrolytes.[93-95] The lack of long-term stability between electrolyte and Li metal anode results in low coulombic efficiency, capacity fading during cycling, and cell failure.[94-96] To protect electrolytes against Li metal and to stabilize Li metal anode, electrolytes and additives are developed to form stable solid-electrolyte-interphase (SEI) layer on Li metal.[96] Forming such SEI layers has led to the success of graphite anode in commercial Li-ion batteries.[93,94,97,98] Besides the spontaneous formation of SEI, applying Li-stable protection materials as artificial SEI on Li metal is also demonstrated to significantly improve the cyclability and coulombic efficiency of the cells with Li metal anode.[84,99-102] Recently, using solid electrolytes to assemble all-solid-state lithium-ion batteries is a promising direction to enable Li metal anode.[90] For example, the solid electrolyte LiPON, an oxynitride material, was demonstrated to achieve a cycle life of over 10,000 cycles in thin-film lithium metal batteries.[8]

This chapter has been published in **Y. Zhu**, X. He, Y. Mo, Strategies based on nitride materials chemistry to stabilize Li metal anode. ***Advanced Science***, 1600517, (2017)

To protect against the reduction of Li metal, protection coating materials or solid electrolytes that are thermodynamically stable or that form stable passivation layers against Li metal are needed. Many Li binaries such as LiF, Li_2O, Li_2S, Li_3N, and Li_3P, are thermodynamically stable against Li metal, and some are found in SEI layers.[45,98,103,104] However, despite that many lithium solid electrolytes were previously reported to be stable against Li metal, multiple experimental and first principles studies confirmed the reduction of solid electrolytes, including $Li_{10}GeP_2S_{12}$ (LGPS), NASICON-type $Li_{1.3}Al_{0.3}Ti_{1.7}(PO_4)_3$ (LATP), and perovskite $Li_{0.33}La_{0.56}TiO_3$ (LLTO).[13-20] In these materials, Li metal reduces Ge and Ti cations, forming Li-Ge alloy and lithium titanate, respectively. Even for the well-demonstrated Li-compatible LiPON materials, recent computational and *in situ* experimental studies confirmed Li reduction, which leads to a spontaneously formed interphase layer consisting of Li_3N, Li_2O, and Li_3P at Li-LiPON interface.[15,45] This interphase layer is electronic insulating, passivating LiPON against further Li reduction. Therefore, forming passivating SEI layer against Li metal is critical to achieving good stability. Given the limited number of available materials stable against Li metal, the development of novel Li-stable protection materials or solid electrolytes is crucial to enable Li metal anode.

However, the design and discovery of Li-stable materials are still mostly based on a trial-and-error approach, due to the lack of knowledge about Li metal stability of different materials chemistry and compositions. Li reduction behavior is only known for a limited number of well-studied materials. For example, the reduction of Ge and Ti is a known problem in LGPS and LATP, respectively, but it is not clear whether these cations will still be reduced in different compositions or in other anion chemistry. In addition, it is not clear

whether the excellent stability of LiPON is a general property of oxynitride chemistry. Such knowledge about Li stability will be crucial to guide further materials development to stabilize Li metal anode, and will enable guided engineering of materials chemistry to form stable SEI on lithium metal.

In this chapter, we aim to fill this knowledge gap about Li metal stability and passivation behavior over a wide range of materials chemistry. Using a data-driven first principles computation approach based on a large-scale materials database, we studied Li metal stability and lithiation reactions in a wide range of materials chemistry and composition space. We determined the intrinsic thermodynamic stability of materials against Li metal as a function of cation and anion chemistry, and discovered that nitride anion chemistry uniquely exhibits better thermodynamic stability against Li metal compared to oxides, sulfides, and halides. In addition, the materials chemistry and composition range that can form stable passivation interphase against Li metal were identified. On the basis of newly obtained chemistry knowledge from computation, multiple novel strategies to form stable SEI on Li metal anode were proposed, providing opportunities for future research and development of lithium batteries.

4.1. General Trend of Materials Stability against Li Metal Reduction.

We calculated the Li reduction potential (cathodic limit) of M-X binary compounds and Li-M-X ternary compounds in four anion chemistries, X = N, O, S, and F (Fig. 4.1), which are commonly used in solid electrolytes or coating layer materials. To illustrate our results, we first take Al-abiding compounds as examples. The binary materials AlF_3, Al_2S_3 and Al_2O_3 have high cathodic limits of >1.2 V, and their lithiation reactions with Li metal

form Li_9Al_4 and Li-X binary materials with a reaction energy of -0.77, -0.74, and -0.23 eV per Li, respectively (Table 4.1). The same trend is also observed for ternary Li-Al-X (Appendix B), Li-Ge-X, and Li-P-X compounds (Table 4.1).

Table 4.1. Cathodic limits and lithiation reactions for example fluorides, sulfides, oxides and nitrides. The reaction energy E_D is normalized to per Li inserted.

Compound	Phase equilibria at cathodic limit	Cathodic limit ref. to Li/Li+ (V)	Phase equilibria with Li metal	E_D (eV) per Li
AlN	Li_9Al_4, Li_3AlN_2	-0.004	Li_9Al_4, Li_3N *	0.16
Al_2O_3	Al, $LiAl_5O_8$	1.23	Li_9Al_4, Li_2O	-0.23
Al_2S_3	Al, $LiAlS_2$	1.60	Li_9Al_4, Li_2S	-0.74
AlF_3	Al, Li_3AlF_6	1.29	Li_9Al_4, LiF	-0.77
Li_5GeN_3	$Li_{15}Ge_4$, Li_3N	0.20	$Li_{15}Ge_4$, Li_3N	-0.20
Li_4GeO_4	Ge, Li_2O	1.02	$Li_{15}Ge_4$, Li_2O	-0.72
Li_4GeS_4	Ge, Li_2S	1.62	$Li_{15}Ge_4$, Li_2S	-1.04
Li_2GeF_6	Ge, LiF	2.71	$Li_{15}Ge_4$, LiF	-1.60
Li_7PN_4	Li_3P, Li_3N	0.01	Li_3P, Li_3N	-0.01
Li_3PO_4	Li_3P, Li_2O	0.69	Li_3P, Li_2O	-0.69
Li_3PS_4	P, Li_2S	1.72	Li_3P, Li_2S	-1.42
$LiPF_6$	P, LiF	2.74	Li_3P, LiF	-2.06

These examples show that different anion chemistry exhibits different stability against Li metal. In general, fluorides have the highest cathodic limits, yielding poorest stability against Li metal. This is similar to the trend observed in organic liquid electrolytes, as fluorinated compounds usually show higher reduction potential.[95] Oxides and sulfides

* Since AlN is stable against Li metal, such phases are not phase equilibria with Li metal, but are fully lithiated products after lithiation with overpotential.

have lower cathodic limits than fluorides, and only a few of investigated oxides and sulfides are thermodynamically stable against Li metal.

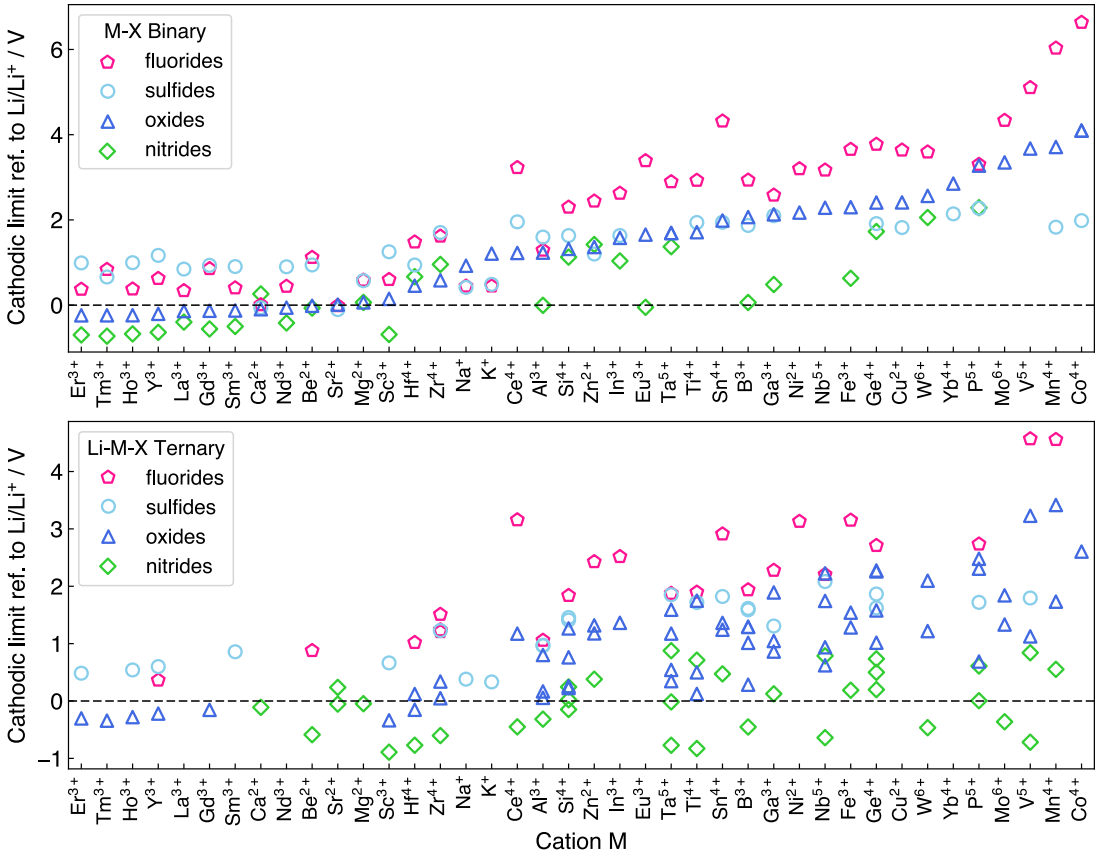

Figure 4.1. Cathodic limits (referenced to Li/Li^+) for Li reduction of a) M-X binary compounds and b) Li-M-X ternary compounds in fluoride, sulfide, oxide, and nitride anion chemistries. Only cation M at its highest common valence state is considered. Each data point represents a compound. A full list of compounds and corresponding lithiation reactions are provided in the Appendix B.

By contrast, nitrides show significant lower cathodic limits compared to other anion chemistry. For example, AlN shows a negative cathodic limit referenced to Li/Li^+, and a positive reaction energy of 0.16 eV per Li to form Li_9Al_4 and Li_3N after lithiation (Table 4.1). Therefore, it is thermodynamically unfavorable to lithiate AlN by Li metal. In addition,

Li_3AlN_2 also shows a negative cathodic limit of -0.32 V (Appendix), indicating its intrinsic stability against Li metal reduction. These trends are observed in both binary and ternary compounds with other cations. In general, many nitrides have negative reduction potential, and are thermodynamically stable against Li metal. Some of these nitrides that are electronic insulators and decent ionic conductors, e.g. Li_3AlN_2, Li_3BN_2, Li_5SiN_3,[105] may be used as buffer layer materials to protect against Li metal. In summary, nitride anion chemistry shows unique electrochemical stability at low potentials and against Li metal.

4.2. Cation Effect on Lithium Metal Stability and Passivation

Using Li-P-S and Li-Ge-S ternary systems as examples, we illustrate the reduction behavior of different cation chemistry and the effect of cation on Li stability and passivation. The Li-P-S composition space (Fig. 4.2a) includes many well-known solid electrolyte materials, such as Li_3PS_4, $Li_7P_3S_{11}$, and Li_2S-P_2S_5 glass. For example, the lithiation reaction of Li_3PS_4 (blue dashed line in Fig. 4.2a, and Fig. 4.2b) starts with the reduction of P at voltage 1.72 V (Table 4.1) and eventually leads to Li_3P and Li_2S, as

$$8\ Li + Li_3PS_4 \rightarrow Li_3P + 4\ Li_2S\ (\Delta H = -11.39\ eV \text{ or } -1099\ kJ\ mol^{-1}),$$

which is highly thermodynamically favorable. Since Li_3P and Li_2S are the only stable phases against Li among entire Li-P-S composition space, any Li-P-S ternary compound would form the same phase equilibria after full lithiation (green bar in Fig. 4.2a), leading to the spontaneous formation of interphase consisting of Li_3P and Li_2S. Since both phases are electronic insulating, the formed interphase is passivating against further Li reduction.[15,106] The formation of Li_3P and Li_2S interphase of $Li_7P_3S_{11}$ on Li is confirmed by *in situ* X-ray photoelectron spectroscopy (XPS) experiments.[107]

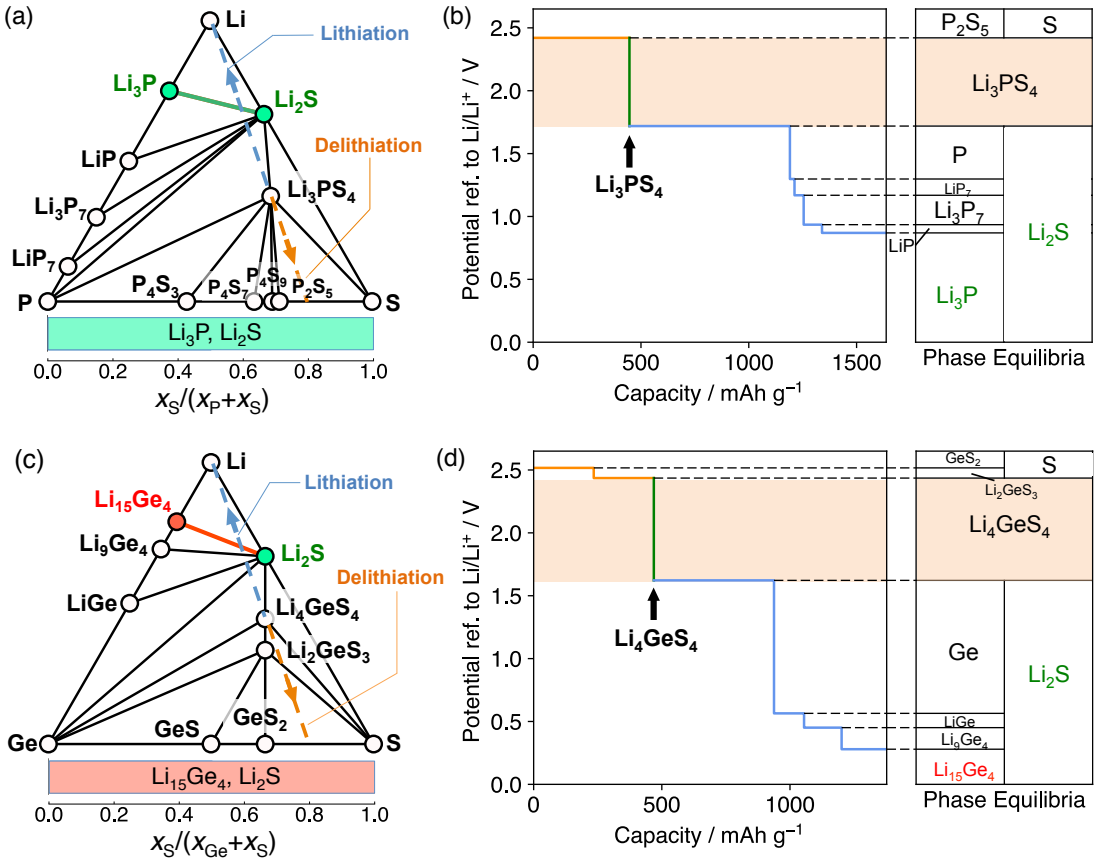

Figure 4.2. Phase diagrams of a) Li-P-S and c) Li-Ge-S system, and the equilibrium voltage profiles and phase equilibria for lithiation and delithiation reactions of b) Li_3PS_4 and d) Li_4GeS_4. Li-stable phases that are electronic insulating (Li_3P and Li_2S) and that are electronic conductive ($Li_{15}Ge_4$) are colored green and red, respectively. The bottom bar in a) and c) represents the phase equilibria with Li metal as a function of atomic fraction x_S and x_M, where passivating and non-passivating ranges are colored green and red, respectively. The lithiation and delithiation paths in a) and c) are marked as blue and orange dashed lines, respectively. These lines represent constant ratio of S and M atomic fraction x_S to x_M (M = P, Ge) but varying Li content in the composition.

Li-Ge-S system (Fig. 4.2c) is commonly used in the design of thio-LISICON electrolyte. The lithiation reaction of Li_4GeS_4 (Fig. 4.2d) would start with the reduction of

Ge at 1.62 V (Table 4.1), continue with Li-Ge alloying reactions, and eventually form $Li_{15}Ge_4$ and Li_2S in equilibrium with Li metal (Fig. 4.2d). The entire lithiation reaction can be written as

$$7.75\ Li + Li_4GeS_4 \rightarrow 0.25\ Li_{15}Ge_4 + 4\ Li_2S\ (\Delta H = -8.04\ eV \text{ or } -775\ kJ\ mol^{-1})$$

In contrast to Li_3P, metallic $Li_{15}Ge_4$ results in the interphase with mixed ionic and electronic conducting (MIEC) property. The simultaneous transport of both Li^+ and e^- through the MIEC interphase allows continuous, favorable Li reduction reaction, and hence cannot passivate at the interface.[15-19,106,108,109] The non-passivating behavior of MIEC interphase is confirmed in previous experiments, where the interfacial layers and resistance grow significantly over a short period of time.[19] Any Li-Ge-S ternary compound leads to the same phase equilibria of $Li_{15}Ge_4$ and Li_2S on Li (red bar in Fig. 4.2c). Any Ge-containing ternary sulfide, regardless of its composition, would not be passivating against Li metal. Therefore, cations play a critical role in forming passivating or non-passivating interphase layers. Unless in nitride anion chemistry, most metal or metalloid cations will be reduced (Fig. 4.1) by Li metal to form metal or Li alloys (Table 4.1 and Appendix), leading to the formation of non-passivating MIEC interphase. The strategy to protect the reduction of metal or metalloid cations is critical.

4.3. Anion Effect on Lithium Metal Stability and Passivation.

We illustrate the effects of anion chemistry on Li stability and passivation using Li-Al-X (X = O, S, F, and N) ternary systems as examples (Table 4.1, Fig. 4.3 and Appendix). The lithiation reactions of ternary oxides, sulfides and fluorides to form Li_9Al_4 and Li-X

binaries are thermodynamically favorable, leading to spontaneous interphase layer formation (Appendix). In Li-Al-O system, which is commonly used for coating layer materials,[84,110,111] the phase equilibria with Li metal are Li_9Al_4 alloy and Li_2O (Table 4.1 and Fig. 4.3a). Similarly, Li metal phase equilibria of Li-Al-S and Li-Al-F systems also include Li_9Al_4 (Table 4.1 and Fig. 4.3b-c). The presence of metallic Li_9Al_4 leads to a MIEC interphase, which may not passivate. These computation results are consistent with the experimental observation of the reduction of Al_2O_3 and Al_2S_3 at low potentials.[112,113]

The Li-Al-N system shows unique behavior compared to O, S, F-based systems (Table 4.1 and Fig. 4.3d). Al-abiding nitrides AlN and Li_3AlN_2 have negative cathodic limits and positive reaction energy for lithiation (Table 4.1 and Appendix). The phase equilibria with Li metal may consist of different combination of thermodynamically stable phases against Li metal, such as Li_9Al_4, AlN, Li_3AlN_2, and Li_3N, depending on the atomic fraction of Al x_{Al} and nitrogen x_N in the material composition. When $x_N < x_{Al}$ (red bar in Fig. 4.3d), the phase equilibria of Li reduction are Li_9Al_4 and AlN through the reaction

$$\mathrm{Li} + \mathrm{Li}_{x_{\mathrm{Li}}}\mathrm{Al}_{x_{\mathrm{Al}}}\mathrm{N}_{x_{\mathrm{N}}} \rightarrow \mathrm{Li}_9\mathrm{Al}_4 + \mathrm{Li}_3\mathrm{N},$$

leading to non-passivating MIEC interphase. At higher N content of $x_{Al} < x_N < 2x_{Al}$, the formed Li-stable phase equilibria are AlN and Li_3AlN_2, through the reaction

$$\mathrm{Li} + \mathrm{Li}_{x_{\mathrm{Li}}}\mathrm{Al}_{x_{\mathrm{Al}}}\mathrm{N}_{x_{\mathrm{N}}} \rightarrow \mathrm{Li}_3\mathrm{AlN}_2 + \mathrm{AlN}.$$

And at even higher N content $x_N > 2x_{Al}$, the phase equilibria are Li_3AlN_2 and Li_3N (Fig. 4.3d), through the reaction

$$\mathrm{Li} + \mathrm{Li}_{x_{\mathrm{Li}}}\mathrm{Al}_{x_{\mathrm{Al}}}\mathrm{N}_{x_{\mathrm{N}}} \rightarrow \mathrm{Li}_3\mathrm{AlN}_2 + \mathrm{Li}_3\mathrm{N}.$$

Since Li_3N, Li_3AlN_2 and AlN are electronic insulating,[86,114,115] the formed interphase would be passivating when $x_N \geq x_{Al}$ (green bar in Fig. 4.3d). Such passivation

interphase between Li metal and Li-Al-N compounds is similar to the spontaneously formed inter-layer at the Li-LiPON interface. In addition, both Li_3AlN_2 and Li_3N are ionic conducting materials,[86,115] which facilitate interfacial ionic transport and reduce interfacial resistance.

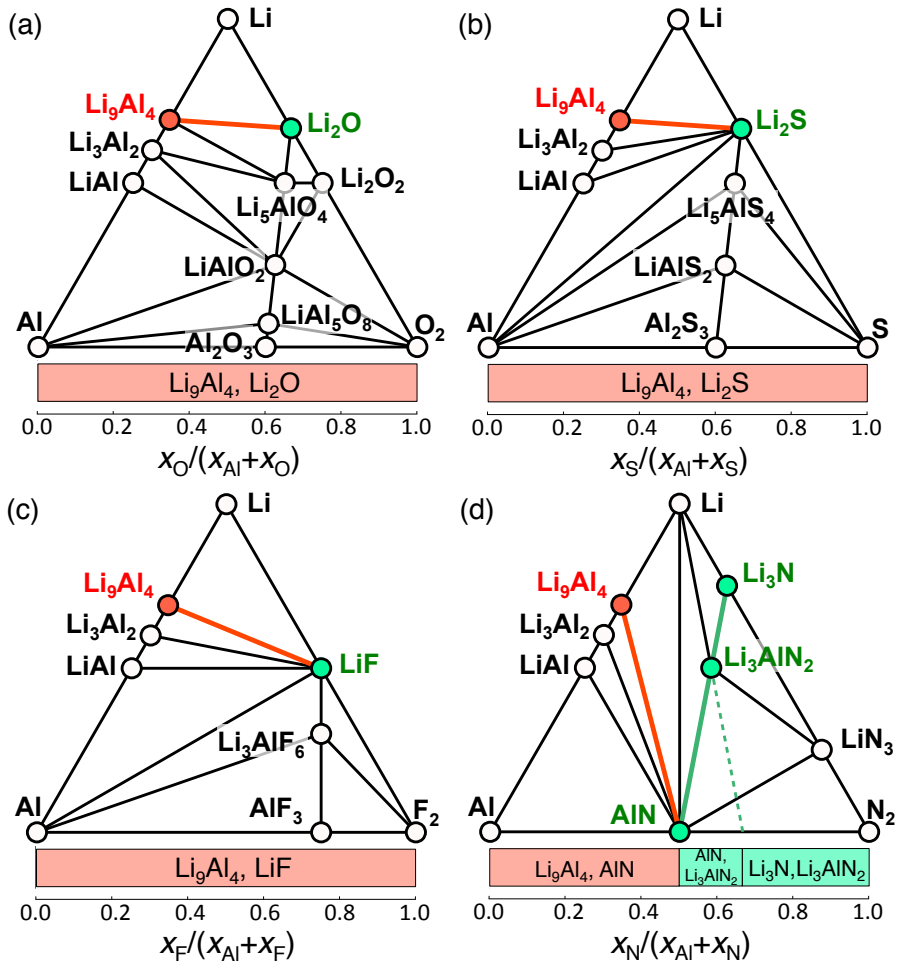

Figure 4.3. Phase diagrams of a) Li-Al-O, b) Li-Al-S, c) Li-Al-F, d) Li-Al-N systems. Li-stable phases that are electronic insulating and that are electronic conductive are colored green and red, respectively. The bottom bar represents the phase equilibria with Li metal as a function of anion and cation atomic fraction x_X and x_M, where passivating and non-passivating ranges are colored green and red, respectively.

Among these four anion chemistry with Al cation, nitride is the only anion chemistry that is stable or can form passivating interphase layer at Li metal contact. This passivation mechanism is activated at high nitrogen content $x_N \geq x_{Al}$, where electronic insulating nitride phases are formed to passivate and stabilize the interface. If nitrogen content is low, the formed interphases would still contain Li_9Al_4 alloy and cannot passivate (bottom bar in Fig. 4.3d). The passivation is enabled by the electronic insulation of (lithium) metal nitrides, such as Li_3AlN_2 and AlN, formed against Li metal. The stability of these nitrides are thermodynamic intrinsic and are unique to nitride. For example, the calculated cathodic limit of ternary nitride Li_3AlN_2 is -0.32 V (referenced to Li/Li^+), which is lower than ternary oxide $LiAlO_2$ (0.17 V), and ternary fluoride Li_3AlF_6 (1.06 V) (Appendix B).

4.4 Stability and Interphase Passivation of Nitrides

We calculated phase equilibria with Li metal for Li-M-N compositions as a function of x_M and x_N (Fig. 4.4), according to the reaction

$$\mathrm{Li} + \mathrm{Li}_{x_{\mathrm{Li}}}\mathrm{M}_{x_{\mathrm{M}}}\mathrm{N}_{x_{\mathrm{N}}} \rightarrow \text{Phase equilibria with Li metal.}$$

The excellent electrochemical stability of metal nitrides against lithium metal is general for many cations (Fig. 4.4). For cation M = Mg, Ca, Al, Hf, Sc, B, Zr, Si, Ti, Ta, Nb, W, and V, passivating interphase may form depending on the material composition. At low N content, the formed interphase includes M metal or Li-M alloy, which are electronic conducting and may not provide passivation. At high N content, the formed interphase consists of Li_3N and (lithium) metal nitrides (Fig. 4.4). If formed metal nitride is electronic insulating, the interphase would be passivating. These lithium ternary nitrides that are stable against Li metal include LiMgN, LiCaN, Li_3AlN_2, Li_2HfN_2, Li_3ScN_2, Li_3BN_2, Li_2ZrN_2,

Li_5SiN_3, Li_5TiN_3, Li_4TaN_3, Li_7TaN_4, Li_7NbN_4, Li_6WN_4 and Li_7VN_4. At high N content, these metal nitrides form at the interface and may passivate against Li metal.

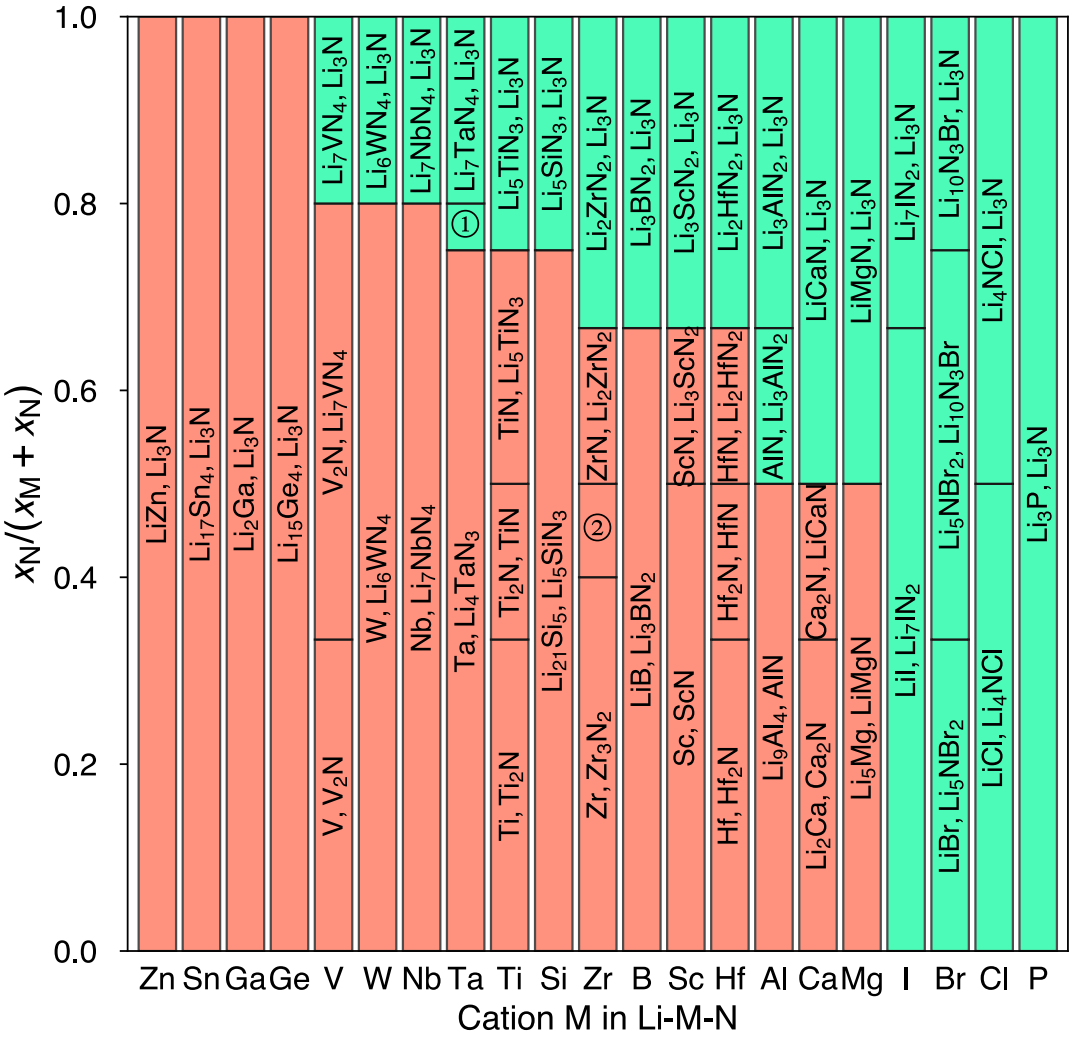

Figure 4.4. Phase equilibria of Li-M-N compositions in equilibrium with Li metal. The formed products due to Li reduction is a function of atomic fraction x_N and x_M (y axis) in the composition. (①: [Li_4TaN_3, Li_7TaN_4]; ②: [Zr_3N_2, ZrN].) The passivating and non-passivating phase equilibria regions are colored green and red, respectively.

By contrast, some cations, such as M = Ge, Ga, Sn, and Zn, cannot be stabilized in nitrides against Li metal regardless of the composition. Li metal phase equilibria of these Li-M-N systems always contain metal or Li-metal alloy (Fig. 4.4) forming MIEC interphase. The formed interphase layer is likely not passivating if these cations are used.

The systems with only non-metal elements, such as M = P, Cl, Br, I, is in general compatible with Li metal. When in equilibrium with Li metal, the reduction products are still electronic insulating phases, including Li_3P, LiCl, LiBr, and LiI. Some non-metal elements may change from cation to anion after reduction. In these nitride systems with only non-metal elements, passivating interphase would form at the Li metal interface regardless of x_N (Fig. 4.4). Similarly, using only these non-metal elements also leads to Li-passivating interphases in oxides and sulfides, as observed in LiPON, Li_3OCl/Li_3OBr, Li_9S_3N, $Li_7P_3S_{11}$, and $Li_7P_2S_8I$ solid electrolytes, which are Li metal compatible.[3,54,70,116,117]

4.5 Stability and Interphase Passivation of Mixed-anion Nitrides

Since nitrides in general show good electrochemical stability against Li metal, here we explore the stability of mixed anion chemistry with nitride corresponding to the doping of nitrogen or nitride into other anion chemistry. We first studied the Li-Al-O-N quaternary system as an example, in which Li-Al-O ternary compound is doped with nitrogen. In the quaternary Li-Al-O-N system, the final phase equilibria in contact with Li metal will only consist of Li-stable phases, including Li_9Al_4, Li_2O, Li_3N, AlN, and Li_3AlN_2 (Fig. 4.5a). Among those phases, only Li_9Al_4 is MIEC, and all other phases are electronic insulating. Similar to the ternary case, the phase equilibria with Li metal are determined by atomic fraction of Al and nitrogen, x_N and x_{Al}. At low N content of $x_N < x_{Al}$, the formed phase

equilibria consist of Li_9Al_4, Li_2O, AlN represented by the red triangle in Fig. 4.5a-b. For example, the lithiation reaction of Al_3NO_3 (gamma-ALON) follows the blue dashed line in Fig. 4.5a to form these products. This lithiation reaction has the voltage profile and phase equilibria shown in Fig. 4.5c. For composition at higher N content of $x_{Al} < x_N < 2x_{Al}$ (green triangle II in Fig. 4.5a-b), Li phase equilibria are Li_3AlN_2, Li_2O, and AlN. At even higher N content of $x_N > 2x_{Al}$ (green triangle I in Fig. 4.5a-b), the phase equilibria with Li are Li_3N, Li_2O, Li_3AlN_2. The phase equilibria with Li metal are a function of the Al-O-N composition, and are represented by the grand potential phase diagram in equilibrium with Li metal (Fig. 4.5b). At high N content (green triangle I and II in Fig. 4.5a-b), the formed interphase after lithiation is electronic insulating and hence passivating. These results suggest a strategy of introducing a sufficiently high amount of N to stabilize oxide compounds, which are not stable against Li metal. High-dose nitrogen doping inhibits the reduction of Al and the formation of Li-Al alloy, leading to a passivating interphase formed against Li metal.

Mixing nitrogen can also stabilize Li-M-O oxides with other cation M = Mg, Ca, Al, B, Zr, Si, Ti, Ta, Nb, V and W. Similar to M = Al, having high amount of nitrogen in Li-M-O-N systems leads to forming electronic insulating nitrides against Li (Fig. 4.6, Table 4.2 and Appendix B). For example in Li-Nb-O-N system, electronic insulating phase equilibria form at high N content $x_N \geq 4x_{Nb}$ (Fig. 4.6a and Table 2). In Li-Ca-O-N system, Li-stable phase equilibria, including electronic-insulating LiCaN nitride and CaO oxide, may form as passivation interphase at the high O and N content of $x_N + x_O \geq x_{Ca}$ (Fig. 4.6b and Table 4.2). Therefore, high-dose nitrogen doping is effective in passivating many oxides with metal cations.

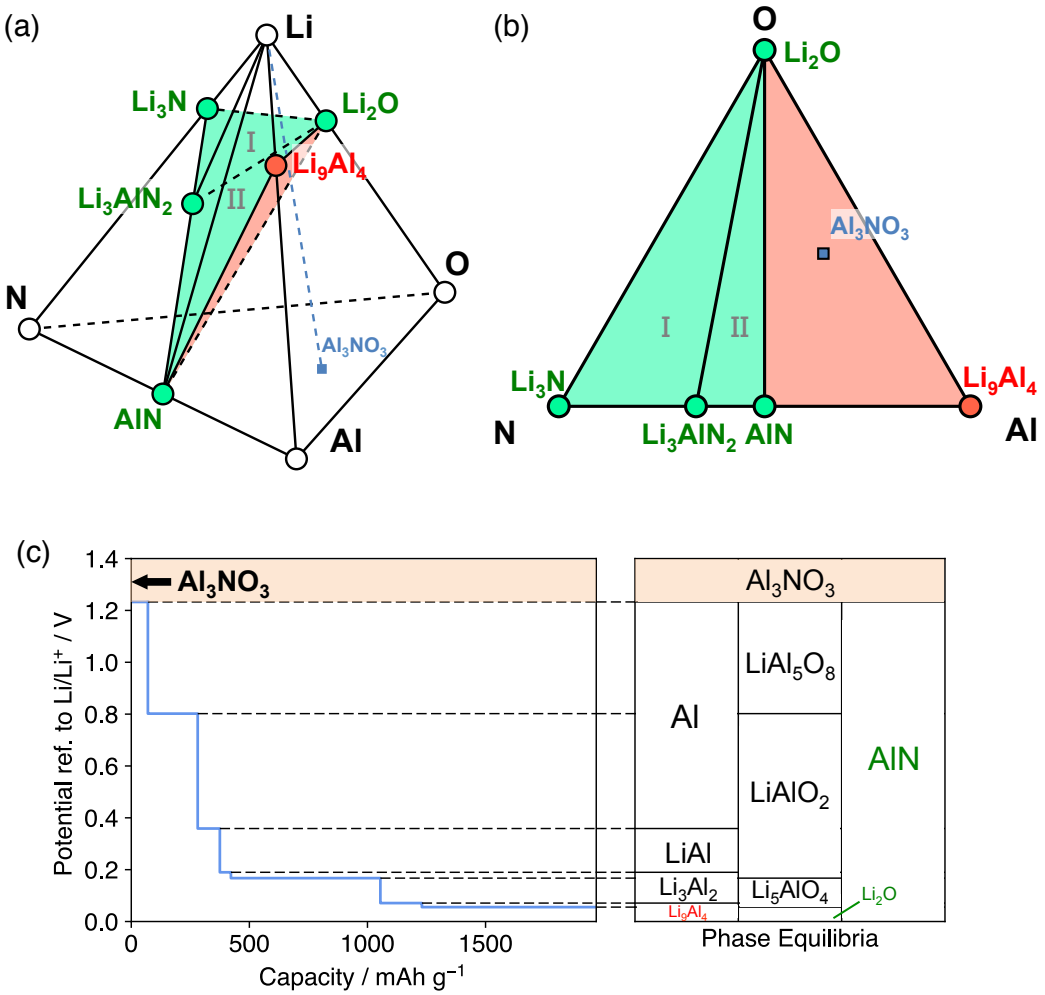

Figure 4.5. a) Li-Al-O-N quaternary phase diagram showing only Li-stable phases. The blue dashed line represents the lithiation path of Al_3NO_3 (blue square point). b) Grand potential phase diagram of Li-Al-O-N system in equilibrium with Li metal. The Gibbs triangle of the grand potential phase diagram is based on non-Li composition Al-O-N, which determines the phase equilibria after lithiation. For example, the phase equilibria of Al_3NO_3 (blue square) with Li metal are Li_9Al_4, Li_2O, and AlN, corresponding to the red triangle region. The composition regions that form passivating and that form non-passivating interphases are colored green and red, respectively. c) Voltage profile and phase equilibria for the lithiation of Al_3NO_3.

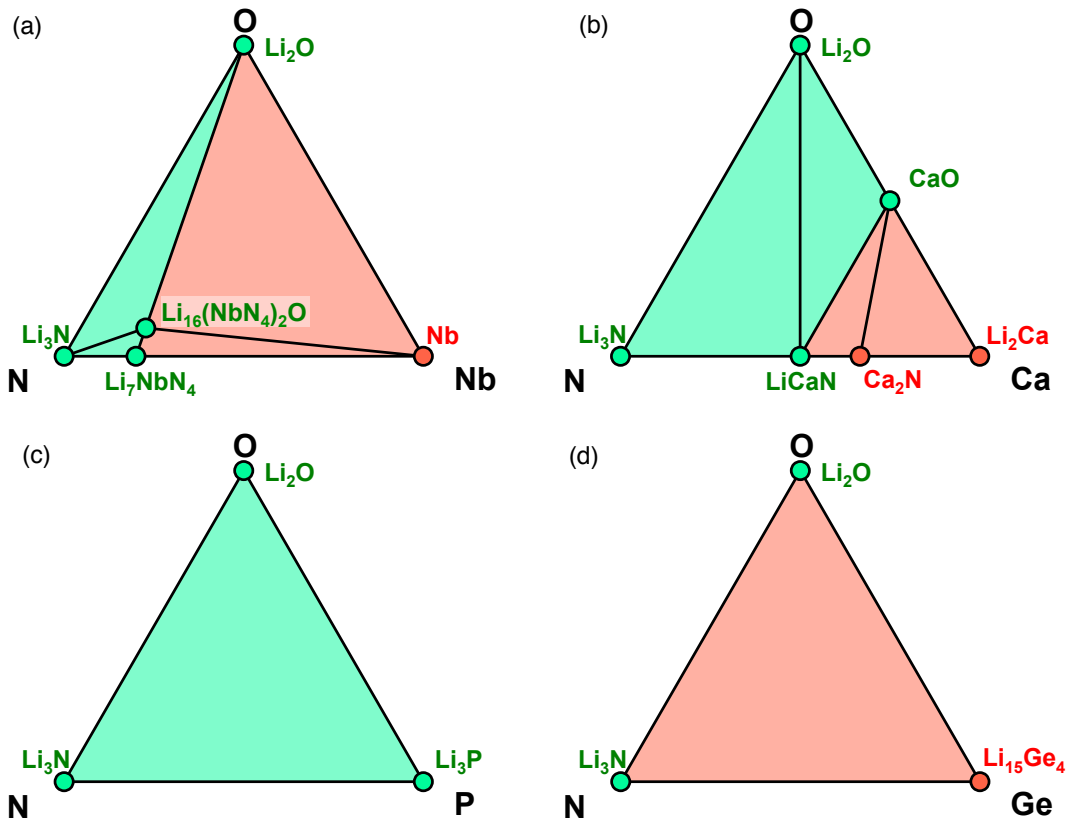

Figure 4.6. Grand potential phase diagrams of a) Li-Nb-O-N, b) Li-Ca-O-N, c) Li-P-O-N, d) Li-Ge-O-N systems in equilibrium with Li metal. The composition regions that form passivating and that form non-passivating interphases are colored green and red, respectively.

Li-P-O-N oxynitride system has Li phase equilibria consisting of only electronic insulating phases, Li_3N, Li_2O, and Li_3P (Fig. 4.6c), which are observed by *in situ* XPS experiments.[45] In addition, Li_3N and Li_3P are fast lithium ionic conductors, which facilitate interfacial Li transport and reduce interface resistance. The formation of passivating interphase results in excellent Li compatibility of LiPON. Similarly, other non-metal elements, such as Cl, Br, and I, also always form passivating interphase at Li metal. Such

passivating layer, as in the case of Li-LiPON interface, may achieve good stability on Li metal anode.

Table 4.2. Composition range in Li-M-N-O systems that form stable passivation interphase.

Cation M	Composition range forming passivation interphase layer
Al	$x_N \geq x_{Al}$
Nb	$x_N \geq 4x_{Nb}$
B	$x_N \geq 2x_B$
Zr	$x_N \geq 2x_{Zr}$
Ta	$x_N \geq 4x_{Ta}$ or $x_N \geq 3x_{Ta} + 2x_O$
Ti	$x_N \geq 3x_{Ti}$
Si	$x_N \geq 3x_{Si}$
V	$x_N \geq 4x_V$
W	$x_N \geq 4x_W$
Mg	$x_N \geq x_{Mg}$
Ca	$x_N + x_O \geq x_{Ca}$
P, Cl, Br, I	Any x_N and x_M
Ge, Sn, Ga, Zn	None

Unfortunately, for oxides with some other cations, passivating interphases cannot be achieved by the introduction of nitrogen. For example, the phase equilibria of Li-Ge-O-N system with Li metal are always Li_3N, Li_2O, and $Li_{15}Ge_4$ regardless of N content (Fig. 4.6d). The presence of $Li_{15}Ge_4$ would lead a MIEC interphase. Similarly, materials containing Sn, Ga, or Zn have Li phase equilibria always containing metal or

Li-metal alloy (Appendix B and Table 4.2), and hence may not be passivated by the formation of nitrides.

4.6 Discussion

Our computation results revealed the Li metal stability of materials with different cation and anion chemistry. Most oxides, sulfides, and fluorides, which are widely studied as current solid electrolytes or coating layer materials, are not stable against Li metal. Metal and metalloid cations in oxides, sulfides, and fluorides (and other halides) are reduced at low potentials in most of these compounds. The thermodynamically favorable Li reduction of metal cations would lead to the formation of mixed ionic and electronic conducting (MIEC) interphase and continuous decomposition of bulk materials, resulting in poor stability against Li metal. To avoid the detrimental effects of metal cations on stability, using only non-metal elements, such as P, Cl, Br, I, instead forms passivating interphase and enables stability against Li metal, as demonstrated in some Li-compatible solid electrolytes, such as LiPON, Li_3OCl/Li_3OBr, Li_9S_3N, $Li_7P_3S_{11}$, and $Li_7P_2S_8I$.[3,54,70,116,117] However, there is a limited choice of these compounds for stabilizing Li metal. Our results provide the composition space to select, design, and discover materials that are stable against Li.

The major discovery of our study is that nitride anion chemistry has significantly better stability against Li metal compared to oxide, sulfide, and halide. Many nitride materials are thermodynamically stable against Li metal. In addition, the nitrides formed at the interface during lithiation become stable, passivating SEI against Li metal. This chemistry knowledge from our computation suggests multiple strategies as follows to stabilize materials against Li metal and to improve the performance of Li metal anode.

1) Many nitride materials that are electronic insulators may be used as protective buffer layers on Li metal anode. These buffer layers are thermodynamically stable against Li metal, thus will protect the electrolyte from reduction and will have long-term stability on Li metal. For example, Li_3N is demonstrated as an effective buffer layer material to protect liquid or solid electrolytes and to improve the cyclability and coulombic efficiency of Li metal anode.[84,99,100] Besides Li_3N, many Li-containing nitrides that are stable against Li metal, e.g. Li_3AlN_2, Li_5SiN_3, Li_3BN_2, LiMgN, LiCaN, Li_2HfN_2, Li_3ScN_2, Li_2ZrN_2, Li_5TiN_3, Li_4TaN_3, Li_7TaN_4, Li_7NbN_4, Li_6WN_4 and Li_7VN_4, may also be used as buffer layers on Li metal anode. In addition, developing new materials, such as $Li_{18}P_6N_{16}$ nitridophosphate,[118] may also be a promising direction.

2) Our results also suggest that high-dose nitrogen doping in materials can lead to *in situ* spontaneous passivation against Li metal. Surface modification techniques such as nitrogen ion/plasma treatment and other nitriding techniques can locally enrich nitrogen content on the surfaces of the material. The nitrogen-rich surface put into contact with Li metal would form nitride passivation interphase layers and transform into a Li-stable interface. For example, if one can introduce sufficient amount of N into the surface region of Al_2O_3 to the composition range $x_N \geq x_{Al}$, passivation phase Li_3AlN_2 /AlN and Li_2O would form (Fig. 4.5). The necessary nitrogen content and composition to passivate each cation are provided by our calculations (Fig. 4.6, Table 4.2 and Appendix). Various experimental approaches can be used to introduce nitrogen into the material and to stabilize the material interfaces against Li metal. For example, applying nitrogen-doped thin films on Li metal anodes has shown to improve Li metal stability and to inhibit lithium dendrite.[119] Multiple

studies also demonstrated nitrogen doping on carbon-based anode materials greatly improves the cycling stability.[120-122]

3) Another way to locally enrich nitrogen is introducing Li_3N to further react at the interface and to form a stable SEI layer. Li_3N may be introduced as a coating layer or by nitriding Li metal. For example, Li_3N can react with Al_2O_3 at the contact interface and form stable SEI consisting of Li_3AlN_2 and Li_2O through an exothermic reaction, $Al_2O_3 + 4\ Li_3N \rightarrow 2\ Li_3AlN_2 + 3\ Li_2O$ (ΔH = -5.76 eV or -556 kJ mol^{-1}). A similar strategy was demonstrated on Li metal protection by Polyplus.[84]

4) In addition, mixing nitrogen-containing compounds, such as nitride, nitrite, and nitrate, into the materials can also stabilize the interface. For example, Al_2O_3 mixed with $LiNO_3$ may also form a SEI of Li_3AlN_2 and Li_2O in contact with Li through an exothermic reaction $Al_2O_3 + 4\ LiNO_3 + 32\ Li \rightarrow 2\ Li_3AlN_2 + 15\ Li_2O$ (ΔH = -58.20 eV or -5615 kJ mol^{-1}). A similar strategy of using nitrogen-containing additives in liquid electrolytes was demonstrated in forming stable SEI layer on Li metal anode.[123-127] For example, $LiNO_3$ as additive was reported to significantly improve the cyclability and coulombic efficiency of Li metal anode by forming a SEI containing lithium nitride and oxynitrides.[128-130] In agreement with our prediction, high concentration of $LiNO_3$ is needed to achieve high nitrogen content and to form a stable SEI.[125] In addition, other nitrogen-containing compounds, such as cyanide and cyanate, are demonstrated for nitriding metals. Novel nitrogen-containing compounds may be developed for nitriding materials in lithium batteries.

While our computation demonstrated the thermodynamic origin of using nitrides and rich nitrogen content to stabilize Li metal anode, experimental techniques to realize

these new strategies in lithium batteries may need further study to address multiple potential challenges. First, nitride buffer coating layer is desired to be thin (~10 nm), dense, and uniform, to achieve low interfacial resistance and good passivation.[131] Applying such coating may requires thin-film-based techniques, such as sputtering, vapor deposition, atomic layer deposition (ALD), and plasma nitriding, which may not be cost competitive.[132] In addition, some nitrides may be moisture or air sensitive,[131] which requires additional protection during manufacture and processing. Gas nitriding techniques based on nitrogen rich gas, such as ammonia, may be an economic and scalable approach as demonstrated in the nitriding of metals.[132] However, ammonia treatment may induce H into the materials, which may be detrimental for the properties of electrolytes or electrodes. Experimental techniques to economically coat nitride layers and to effectively dope high nitrogen content at the interface need further research and development.

The aforementioned strategies of using nitrogen anion chemistry to stabilize Li metal anode may offer multiple additional advantages. The thermodynamically favorable lithiation reactions provide interfacial wetting, which would promote interfacial contacts.[16,106,133] Moreover, a fraction of nitrogen may be lithiated to form Li_3N, a good ionic conductor, as part of the interphase to facilitate interfacial Li ion transport. In addition, many nitrides exhibit good tolerance to stress, which is a desirable mechanical property for stable interfacial layer during cycling and for suppressing Li dendrite growth.[132,134-138] Therefore, the formation of stable SEI layer using nitride anion chemistry provides good stability against Li metal, reduces interfacial resistance, and may mechanically suppress Li dendrite formation. High nitrogen content as predicted by our calculations (Fig. 4.6 and Table 4.2) is necessary to form phase equilibria only consisting of passivating phases and to completely

inhibit the formation of reduced metallic phases, while a lower nitrogen content may still retard interfacial degradation and benefit the performance of Li metal anode as a result of kinetic stabilization.

The limitations of using the thermodynamic scheme to predict interfacial phenomena should be noted as follows. In this study, we approximated the interphase as the phase equilibria, which are the most thermodynamically favorable states, whereas kinetics of reaction and diffusion are not considered. While kinetics and diffusion play crucial roles in the reactions at the interfaces, the thermodynamics provide an ultimate boundary of stability. Given facile Li diffusion, it is expected the phase equilibria would form at the immediate contact with Li metal, as demonstrated in previous *in-situ* XPS study.[17-19,45,107] Despite possible kinetic or diffusional limitations for such reactions, the thermodynamic driving force would always exist for forming the most favorable phase equilibria. These decomposition reactions may have a significant impact on the long-term stability of the battery. It is possible that the formed interphase layers are different from thermodynamic equilibria. For example, some phases that are not stable against lithium metal may form due to kinetic stabilization. In addition, kinetic limitation of the lithiation reduction at the interface may lead to the formation of intermediate decomposition products, which may be passivating to slow down further degradation.[107] As a result of such kinetic effects, some intermediate decomposition products or less than adequate nitrogen doping may still improve the stability at Li metal interfaces. Nevertheless, designing the interface with thermodynamic intrinsic stability against Li metal is still desired to realize long-term stability, cyclability, and coulombic efficiency of the lithium battery.

Additional approximations made in our computation scheme and their potential impact are noted as follows. We used the mixture of bulk phase properties to approximate the interphase property, and did not consider the microstructures of interphase. For example, if the formed electronic-conducting phases are not percolating from Li metal to electrolyte, the overall interphase layer would still be passivating. The effects of microstructures, local off-stoichiometry, defects accumulation, and kinetically stabilized meta-stable phases, which were not considered in our calculations, may also impact interphase properties and passivation effects. In addition, our scheme relies on known phases to predict Li reduction products of materials. There may be errors in the predicted phase equilibria if some phases that exist in nature were not included. This scenario is more likely in nitride systems, which have been relatively less studied than oxides. In addition, due to the lack of available electronic conductivity data of many materials, we used a simple cutoff based on DFT calculated band gap and the valence states of metal cations to judge whether a phase is electronic conductive or insulating. While the trend of the nitride stability is captured, using experimentally measured electronic conductivity would be more reliable in estimating the interphase properties. Some passivating interphase may still have a low electronic conductivity leading to a slow interphase layer growth and impedance increase during cycling or over time. For example, while the SEI layer on graphite anode in commercial lithium ion battery is well accepted as a passivation film, Dahn *et al*. showed slow growth of SEI and continuous lithium loss.[139,140] The Li-compatible solid electrolyte $Li_7P_3S_{11}$, also shows a slow interphase impedance increase over time.[107] Nevertheless, these passivating interphases have significantly better stability than non-passivating interphases, and provide improved cyclability and battery performance.[19]

4.7 Conclusion

In this chapter, our computation revealed that material stability against lithium metal is governed by cation and anion chemistry. Metal cations in oxides, sulfides, and fluorides are usually reduced by lithium metal, leading to poor stability against lithium metal. We discovered that nitride anion chemistry shows unique stability against Li metal. In general, metal nitrides have a significantly lower reduction potential than oxides, sulfides, and fluorides, and many nitrides are thermodynamically stable against Li metal. On the basis of this chemistry knowledge, we suggest new strategies to form stable SEI on Li metal anode. Many nitrides that have intrinsic Li metal stability can be used as buffer layers to protect materials against Li metal. In addition, high-dose nitrogen doping and nitrogen enriching at the interface can lead to spontaneous formation of a stable, passivating SEI on Li metal, transforming a lithium unstable interface into a lithium stable interface. Specifically, many cations, such as Mg, Ca, B, Al, Zr, V, W, Si, Ti, Nb, and Ta, can be protected in nitride anion chemistry systems at sufficiently high nitrogen content. However, some cations, such as Ge, Sn, Ga, and Zn, are always reduced by Li metal regardless of anion chemistry and composition. Our results provide guiding principles for the selection, design, and discovery of materials with Li metal stability, and predict interfacial engineering strategies to stabilize Li metal anodes in lithium batteries.

Chapter 5. Ionic Transport in Grain Boundaries of Lithium Garnet

The key advancement of ASLiBs is mainly because of the discovery and development of solid electrolyte materials. Li-stuffed garnet $Li_7La_3Zr_2O_{12}$ (LLZO) is a very promising group of material.[26] For example, the Al-doped cubic phase $Li_{6.25}Al_{0.25}La_3Zr_2O_{12}$ exhibits bulk ionic conductivity ~ 0.4 mS/cm at room temperature.[141] The fast bulk ionic transport in Li-stuffed garnet has drawn a lot of research effort to understand the underlying mechanism of its fast ion diffusion.[21-25] The cubic phase lithium garnet (c-LLZO) have partially occupied 24*d* and 96*h* Li sites, which forms 3D interconnected pathways.[21] The high Li content activates the concerted migration mode,[22] which enables lithium garnet material to have fast ion transport and thus high ionic conductivity.

However, the solid electrolytes in all-solid-state battery are usually polycrystalline, rather than single crystal. Besides the bulk diffusion, ion diffusion along and across the grain boundaries (GBs) are an essential part of the ionic transport. Therefore, a good solid electrolyte should also have decent ion transport at grain boundaries. Sluggish ionic transport at grain boundaries would have an negative impact on the overall ionic conductivity of SEs and the battery performance.[26,27]

Grain boundaries have different structures and chemistry from bulk, and thus different properties. Since the discovery of superionic cubic phase Li-garnet materials, researchers have been investigating the grain boundary ion transport in this material. Early experiments in 2007 reported that for $Li_7La_3Zr_2O_{12}$, the resistance contributed from grain boundary is comparable to that from bulk under room temperature.[142] In 2010 another work reported that by increasing the calcination temperature, well-sintered $Li_7La_3Zr_2O_{12}$ sample

shows negligible grain boundary resistance.[57] Later Al dopant becomes widely used to stabilize the cubic phase Li-garnet under room temperature. In 2014, experimental results of resolved grain boundary and bulk resistance in Al-doped c-LLZO were reported, where grain boundary shows larger resistance and higher activation energy compared to bulk.[143] A following work in 2015 reported that using proper hot-pressing temperature can increase the sample density and decrease the grain boundary resistance in Al-doped c-LLZO.[141] While another work also in 2015 reported that using solid state reaction, the synthesized Al-doped c-LLZO have more ionic conductive grain boundary compared to bulk.[144]

Moreover, the grain boundaries in solid electrolytes are closely related to lithium dendrite growth, which is currently a critical problem for all-solid-state lithium batteries. Recent experimental works show that lithium dendrite preferentially grows inside the grain boundary of solid electrolyte, which eventually leads to short circuit and cell failure.[28,29] The properties of grain boundaries, such as the ion diffusion property, may help us understand the dendrite growth in the grain boundaries of solid electrolytes.

However, despite its significance, current understanding on the structure, composition and more importantly, the diffusion properties of grain boundaries in solid electrolyte materials, is still limited. This is mainly due to the complex nature of grain boundaries, which poses difficulty for both experimental characterization and computational modeling.

In this chapter, we aim to bridge these knowledge gap. Using molecular dynamics simulation, we investigate the ionic diffusion properties of grain boundaries in lithium garnet. We study the distinct ion diffusion behavior at grain boundaries different from the

facile ion transport in the bulk. We investigate the relationship between the diffusion properties and the structure properties of the grain boundaries. We also reveal why the conventional space-charge theory at grain boundary does not apply to super-ionic conductors like lithium garnet.

5.1 Computational Methods

1. Interatomic potential

We performed classic molecular dynamics simulation to study the ionic diffusion in Li garnet. The sample we constructed is Al doped cubic phase Li garnet (below denoted as c-LLZO) based on experimental reported structure.[21] We used composition $Li_{6.25}Al_{0.25}La_3Zr_2O_{12}$, in which Al^{3+} were randomly doped to Li1 (24*d*) sites to stabilize the cubic phase.

The interatomic potential takes a pairwise form and consists of two parts: a long-range term describes the Coulomb interaction plus a short-range term describes the repulsive and van der Waals interactions. The short range interaction term were modeled by the Buckingham potential

$$E_{buck}(r) = Ae^{-r/\rho} - C \cdot r^{-6} \quad (r < r_c),$$

where r is the atomic pair distance. r_c is the cutoff distance and is set to 12 Å. A, C, ρ are fitting parameters and are listed in Table 5.1, most of which are taken from literatures.[145,146]

All ions except oxygen ions take their formal charge. The core/shell model is applied on O ions to account for the polarization behavior. The shell mass M_{shell}, shell charge Y and the coupling core-shell harmonic spring constant k are also listed in Table 5.1.

Table 5.1. Interatomic potential parameters in Al-LLZO system.

Buckingham potential parameters				Core-shell model parameters for O		
Ionic pair	A (eV)	ρ (Å)	C(eV·Å^{-6})	Y (***e***)	k (eV·Å^{-2})	M_{shell}(a.u.)
Li - O	1430.0	0.260	4.0	-2.76	30.2	1.6
La - O	4579.23	0.3044	0.0			
Zr - O	1385.02	0.350	0.0			
Al - O	1738.0	0.289	0.0			
O – O	22764.3	0.149	27.63			

Fig. C1 shows the lattice parameters of Al-doped LLZO ($Li_{6.25}Al_{0.25}La_3Zr_2O_{12}$) and undoped LLZO ($Li_7La_3Zr_2O_{12}$) in quenching simulation. Our potential successfully captures the spontaneous cubic-tetragonal phase transition behavior in undoped LLZO, while the Al-doped LLZO is stabilized at cubic phase during quenching. The calculated lattice parameters and thermal expansion coefficient agree very well with experimental results (Fig. C1).[21] The room temperature lattice parameter difference is only 0.33%.

Fig. 5.1 shows the calculated the diffusion properties using the aforementioned classic interatomic potential. We observed very typical Arrhenius behavior and the calculated activation energy is 0.23 eV, which is very close to the value from experiments[147] and from first principles calculations.[22,24] (Fig. 5.1) The room temperature conductivity is roughly one magnitude higher than experimental values. In terms of lattice parameter, activation energy and the capture of phase change, our potential shows good performance compared to previous reported classical potentials, especially in the activation energy.

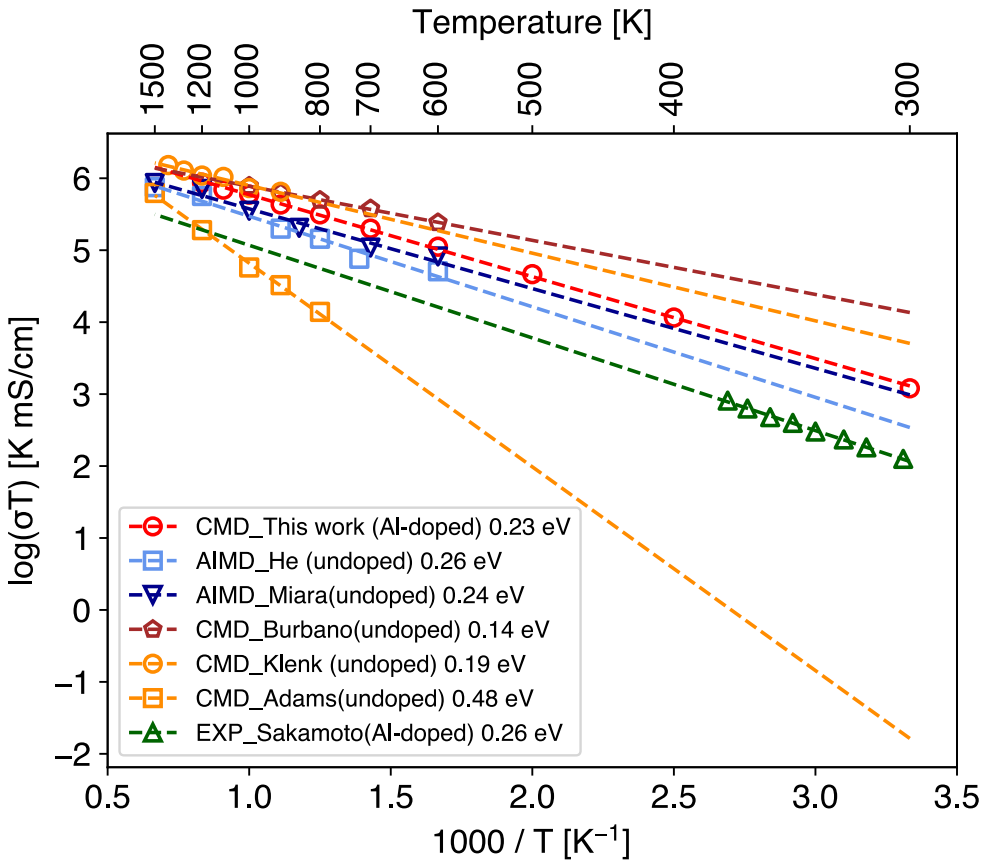

Figure 5.1. Arrhenius plot of ionic conductivity from this work and previous literature reports, including experimental reports (EXP),[147] *ab initio* molecular dynamics simulation (AIMD),[22,24] and classic molecular dynamics simulation (CMD).[148-150] The activation energy listed in the legend are either from literature if available, or fitted if unavailable from literature.

2. Grain boundary sample construction and molecular dynamics simulation details

Since garnet is a group of material share similar framework structure,[26] we assumed they probably share similar low-energy surface orientation. Garnet-type minerals generally have <110> and <112> as the low energy surface orientation.[151] Therefore, here we also selected <110> and <112> as candidate orientations to

construct twist grain boundaries. To satisfy the periodic boundary condition. We construct Σ3 <110> and Σ5 <112> twist grain boundaries. The grain boundaries are perpendicular to *z* axis, and the twist angles are 70.53° and 78.46° respectively around the *z* axis. The simulation box size (under 500 K) are 77.8 Å × 110.1 Å × 147.6 Å for <110> grain boundary and 91.7 Å × 56.2 Å × 127.8 Å for <112> grain boundary, respectively.

All simulation are performed with LAMMPS package.[152] Samples were first heated up to 1200 K and equilibrated for 0.1 ns, and then quenched to target temperature. The self-diffusion simulations were performed under NVE ensemble.

3. Local diffusivity calculation

We tracked the atom trajectories and use the mean-squared-displacement (MSD) to calculate the diffusivity. Conventionally, the diffusivity, as a statistical quantity, is calculated by averaging MSD on all diffusive ions. However, in our grain boundary model, the diffusivity is also a local quantity, which has a non-uniform distribution along *z* direction due to the existence of grain boundaries. To capture the local diffusivity distribution, we calculate local diffusivity based on the locally averaged squared displacement.

We first sliced the sample into 40 layers perpendicular to *z* direction, and then grouped the atom displacement into different layers based on the average *z* position during that period of lag time. We then calculate the MSD for each layer with different lag time. In this way, we can capture the local diffusivity distribution with a reasonable special resolution.

5.2 Diffusion and Structure Properties of Grain Boundaries in Lithium Garnet

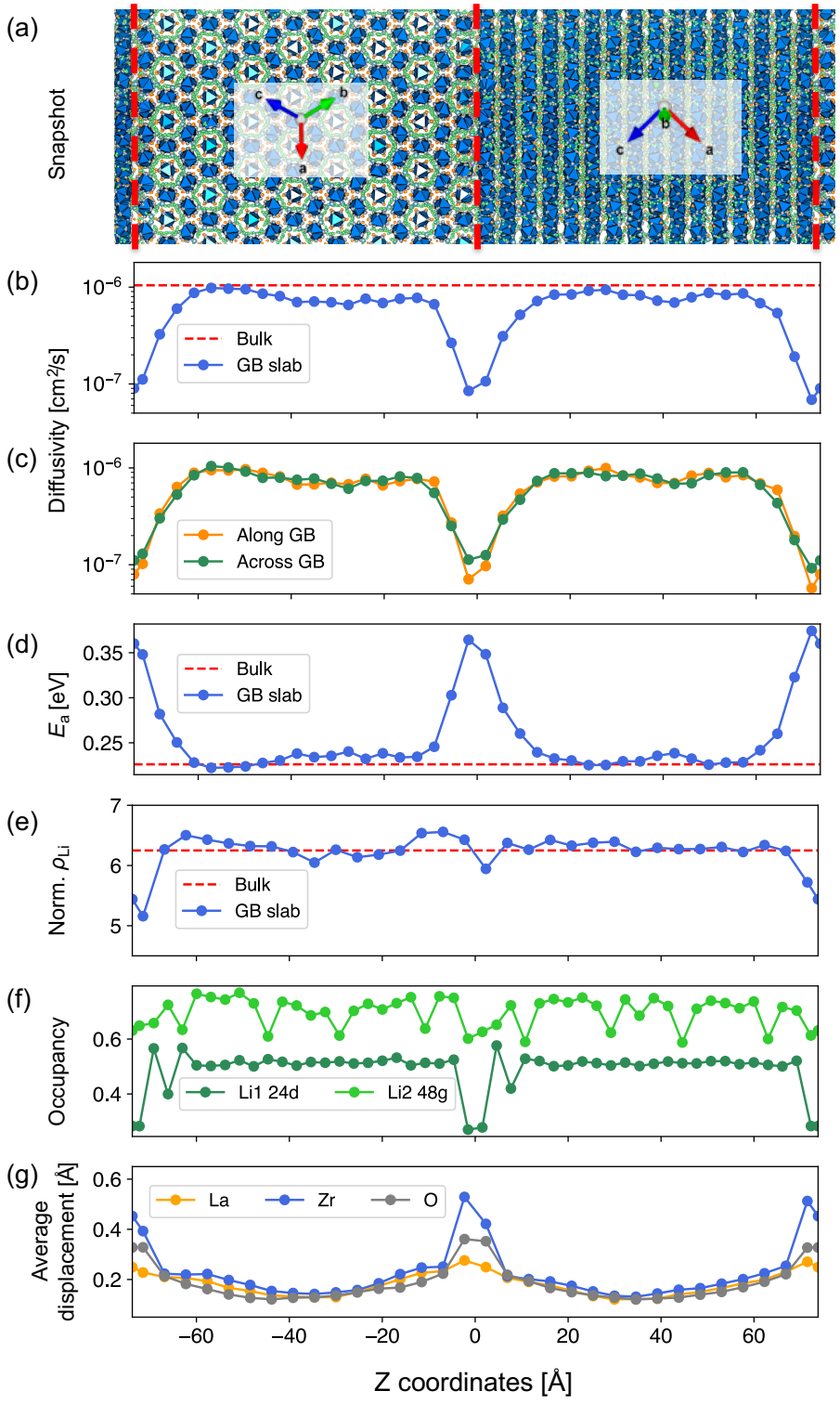

Figure 5.2. a) constructed slab structure of twist <110> Σ3 grain boundaries. The twist angle is 70.53° and the slab thickness is 2 x 73.80 Å. The labeled axes correspond to the conventional cell of lithium garnet. The navy polyhedral are ZrO_6 polyhedral. b) Local ionic diffusivity in the grain boundary slab (blue line) and reference bulk diffusivity (red dashed line) at 500 K. c) Local ionic diffusivity along the grain boundary plane (*xy*) direction (orange line) and across the grain boundary plane (*z*) direction (green line). d) Local activation energy in the grain boundary slab (blue line) and reference bulk activation energy (red dashed line). e) The temporally averaged Li density in the grain boundary slab (blue line) and the bulk reference (red dashed line). Both are normalized to per formula. f) The temporally averaged site occupancies of Li1(24*d*) and merged Li2 (48*g*) sites. g) The averaged displacement between the initial position and average position of framework atoms La, Zr and O. O positions are based on the positions of O cores.

We picked <110> Σ3 twist grain boundary as a representative example to study the grain boundary diffusion in lithium garnet. Fig. 5.2a snapshot shows the constructed structure used in our modeling. Two <110> Σ3 twist grain boundaries locate at $z = 0$ Å and $z = 73.80$ Å, respectively (red dashed line). Fig. 5.2b shows the calculated local ionic diffusivity versus *z* coordinates at 500 K (the blue line). In the center part of the slabs, the diffusivity is very close to the bulk diffusivity 10^{-6} cm^2/s (the red dashed line). However, the diffusivity shows a sharp decrease near the two grain boundaries. In the center region of ±1 nm near the grain boundary planes, the diffusivity drops to 10^{-7} cm^2/s, which is about one order of magnitude lower than that of the center part of the slab. This indicates that the grain boundaries impede the facile ion diffusion in lithium garnet. Fig. 5.2c shows the calculated the directional ionic diffusivity along the grain boundary (*xy*) and across the grain boundary

(z) direction at 500 K. Diffusivity along both directions show similar behavior, which drops to an about one-order-of-magnitude lower in the ±1 nm region near the grain boundaries. This indicates that near the grain boundary core region, diffusion along all directions slows down.

The trend observed at 500 K (Fig. 5.2 b-c) also applies to other temperatures. We fitted the diffusivity using Arrhenius equation to get the local activation energy E_a (Fig. 5.2d). The local activation energy at grain boundary core increases to 0.36 eV, while for regions that are more than 1 nm away from the grain boundaries, the activation energy is still close to the bulk value 0.23 eV.

From our calculation, we found that grain boundaries slow down the ionic diffusion, in both along and across the grain boundary directions. The affected region is localized, only in an approximately 2 nm-thick region beside the grain boundary plane. At the core of grain boundaries, the activation energy of ionic diffusion increases to 0.36 eV. The calculated ionic conductivity at 300 K (extrapolated from Arrhenius relationship) is only 0.03 mS/cm, which is nearly two orders of magnitude lower than the bulk. Both in plane and out of plane diffusion are slowed down, which may because the diffusion channels of lithium garnet are 3-D interconnected. For region that are more than 1 nm away from the grain boundary plane, the ionic diffusion appears to be unaffected. Both the diffusivity and activation energy are very close to bulk value, suggesting that these regions still exhibit bulk-like fast ion diffusion.

Structure analysis was performed to understand the origin of slower diffusion near grain boundary. Fig. 5.2e shows the distribution of temporally averaged local Li content ρ_{Li} normalized to per formula. Compared to the bulk value (6.25 per formula, red dashed line),

there is a slight decrease of lithium content near the two grain boundaries, as they drop to approximately 5.2 and 6 Li per formula, respectively. The two grain boundaries show some variance, which may because the two grain boundaries are not completely symmetric.

We also performed site analysis to calculate the site occupancy on Li1(24*d*) and Li2 (original 96*h* sites, but merged neighboring pairs into 48*g* for occupancy calculation). We used 0.9 Å as a cutoff radius to judge whether a site is occupied or not. As shown in Fig. 5.2f, the occupancy of both Li sites show decrease near the grain boundaries, especially for Li1 sites. This suggested that the Li ions near the grain boundary are not at their original lattice sites. The mismatched lattice at these high-angle grain boundaries strongly disturbs the original interconnected channels of Li ions, which provides fast ion diffusion. As a consequence, the grain boundaries exhibit slower ion diffusion.

In comparison, we also quantified the framework (La, Zr and O atoms) change near the grain boundary. Fig. 5.2g shows the averaged root square displacement between their initial position and average position of these framework atoms. (O positions is calculated based on O core positions) In the region near grain boundaries, the averaged displacement for La, Zr, and O atoms are only around 0.2 Å, 0.5 Å, and 0.4 Å away from their original lattice sites, respectively. This suggested that there is no severe framework structure change near the grain boundaries.

We also performed same analysis for <112> twist grain boundaries (Appendix C), and similar trends were observed. Therefore, our simulation reveals the grain boundary impedes the ion diffusion in approximately 2 nm thick nearby region. Structure analysis shows that framework atoms (La, Zr and O) change is limited, while the original Li sites

show occupancy decrease. The local Li reconfiguration is more likely to be the structure origin of slower diffusion near grain boundaries.

5.3 Discussion

Our simulations reveal the Li diffusion mechanism at grain boundaries in cubic phase lithium garnet material. Grain boundaries slow down the ionic diffusion in the nearby region, and the slower diffusion is observed in an approximately 2 nm thick region near the grain boundary plane. At room temperature, the diffusivity in the grain boundary core is about two orders of magnitude lower than bulk, and the activation energy increases to 0.36 eV. Outside of this 2 nm-thick region, the ionic diffusion seems unaffected by the grain boundary and still show bulk-like behavior.

Our structure analysis shows that the framework (La, Zr, and O atoms) shows limited change. However, the Li sublattice is severely distorted near the grain boundaries. The occupancy of Li sites show decrease near the grain boundaries, especially for Li1(24*d*) sites. This suggested that the Li atoms near the grain boundary moved away from their original lattice sites. Since the grain boundaries in our simulation are high angle grain boundaries, the strongly distorted Li sublattice probably leads to the absence of interconnect fast 3-D channel near the grain boundaries. Therefore, the facile ion transport in bulk lithium garnet are impeded at the grain boundaries, which results in slower grain boundary ion diffusion.

This mechanism of slow grain boundary diffusion may be a general phenomenon in most lithium super ionic conducting materials. In these super ionic conductors, the crystalline bulk phases usually have highly optimized structure characteristics for fast ion

conduction,[22,153] while the grain boundary structures usually exhibit a deviation from the ideal bulk. Therefore, the grain boundary usually has slower diffusion compared to the bulk.

Our results also show there is no significant space-charge layer effect. Neither major Li accumulation nor major depletion was observed. The ionic conductivity change mostly originates from the increase of activation energy induced by structure change, instead of carrier concentration change. In fact, based on space-charge layer theory, the Debye Length can be calculated as

$$L_{\mathrm{Debye}} = \sqrt{\frac{k_{\mathrm{B}} T \varepsilon \varepsilon_0}{2e^2 c_{\mathrm{Li}}}}$$

where T is the temperature, ε_0 is the relative permittivity, k_{B} is the Boltzmann constant, c_{Li} is the concentration of charge carriers, and ε_0 is the absolute permittivity. As an estimation, we consider all the Li ions as effective charge carriers, and use an approximate relative permittivity $\varepsilon = 10$.[154] The Debye length at 300 K would be only 0.18 Å, even much shorter than the interatomic distance. Note that the space charge theory is based on continuum assumptions, under which both the carrier concentration and the electrostatic potential have continuous special distribution. In contrast, the calculated Debye length in lithium garnet falls into atomistic scale, at which both carrier concentration and the electrostatic potential are ill-defined. This indicates that the conventional space charge layer theory is not applicable to the super-ionic conductor material like lithium garnet.

The lack of space charge layer effect may also be generally expected for super ionic conductor materials, most of which have highly disordered ion sublattice and very high carrier concentration. In super ionic conductor materials, the change of carrier concentration near grain boundaries is usually not the limiting factor of ion diffusion. Instead, the

mismatched lattice near the grain boundaries, especially high angle grain boundaries, may lead to high migration barrier, and thus resulting in slower diffusion.

Therefore, grain boundaries in lithium garnet exhibit different ion diffusion mechanism from bulk. The abrupt change of ion transport properties at grain boundaries may affect the field distribution inside the solid electrolyte and may have impact on Li dendrite growth, which deserve further detailed studies in the future.

Chapter 6. Strain Induced Order-disorder Transition in Lithium Garnet

Mechanical strain is an important factor that can significantly affect the ion diffusion in solid electrolytes and battery performance.[30,31]. During the assembling of all-solid-state battery, externally applying mechanical strain is a commonly used method to improve the physical contact and to decrease the interfacial resistance.[155] Besides, electrode materials, such as Li metal anode and $LiFePO_4$ cathode, can undergo considerable volume change during the battery cycling.[156,157] This would also induce a strain on the solid electrolytes that are in intimate contact with the electrodes. Mechanical strain can have a critical impact on the ionic diffusion in solid electrolytes. It was previously reported that in oxygen ionic conductor and lithium ionic conductor materials, strain can induce orders of magnitude change in diffusivity.[158,159] Nevertheless, for lithium garnet, currently there is very little information about the effect of mechanical strain on its ion diffusion properties.

In this chapter, we aim to understand the strain effect on lithium garnet. By constructing atomistic model and using molecular dynamics simulations, we investigate the effect of mechanical strain on the ionic diffusion in lithium garnet material. We explore how the strain could affect the ionic diffusion in lithium garnet. We also reveal the coupling between mechanical strain and Li sublattice ordering, and demonstrate the strain can induce order-disorder transition in Li sublattice of lithium garnet, which has a significant effect on the diffusion. These understanding can be helpful to the further development of all-solid-state Li-ion battery.

6.1 Effect of Mechanic Deformation on the Ionic Diffusion in lithium garnet

We study how mechanical deformation on lithium garnet affects its ionic diffusion properties. Tensile and compressive uniaxial strain were applied, respectively, and the engineering normal strain is 1% and 3%. The lateral strain is controlled by Poisson ratio, which was set to 0.26.[136,160]

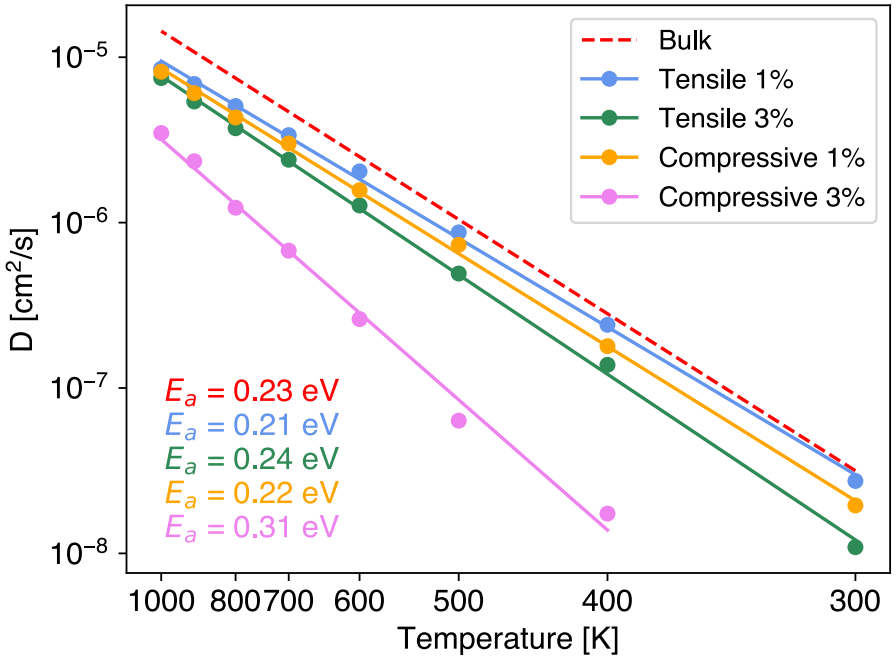

Figure 6.1. Arrhenius relationship of lithium garnet under mechanical deformation.

Fig. 6.1 shows the calculated diffusivity under different strain. In all cases, mechanical deformation decreases the ionic diffusivity. 1% tensile or compressive strain only slight slows the diffusion. The calculated activation energy are 0.21 eV (1% tensile, blue line in Fig. 6.1) and 0.22 eV (1% compressive, orange line in Fig. 6.1), respectively, which are very close to the bulk value (red dashed line in Fig. 6.1). Increasing tensile strain to 3% further decreases the diffusivity, while the calculated activation energy is 0.24 eV, which still does not show any significant change from the undeformed bulk. However, 3%

compressive strain leads to a significant decrease in diffusivity (purple line in Fig. 6.1) and an increase of the activation energy to 0.31 eV.

6.2 Strain-induced Order-Disorder Transition in Lithium Garnet

Undoped lithium garnet $Li_7La_3Zr_2O_{12}$ has two polymorphs, high temperature cubic phase c-LLZO and low temperature tetragonal phase t-LLZO. c-LLZO has a disordered Li sublattice, in which Li ions partially occupy 24*d* and 96*h* sites, while t-LLZO has an ordered Li sublattice, in which Li ions fully occupy 8*a*, 16*f*, and 32*g* sites. The cubic phase has a higher ionic conductivity thanks to its disordered Li sublattice. To obtain the more ionic conductive cubic phase lithium garnet, dopants like Al are commonly used to stabilize the cubic phase under room temperature.

Before applying deformation, our Al-doped LLZO sample stays at the cubic phase with disordered Li sublattice. Applying a 3% compressive strain would change its lattice parameters close to the undoped tetragonal phase of lithium garnet. The a / c ratio of the sample under 3% compressive engineering strain is 1.039, while the a / c ratio of tetragonal phase undoped LLZO reported from experiments is 1.036.[21] This suggest that the applied compressive strain may leads Li sublattice undergo an order-disorder transition, and thus leads to slow ionic diffusion.

We calculated the virtual XRD pattern of Li sublattice in the c-LLZO sample to investigate the Li sublattice ordering change. The XRD pattern is calculated based on virtual diffraction analysis,[161] using a wavelength of 1.542 Å (Cu Kα as the virtual radiation source).

The XRD pattern is determined by both the lattice parameters and the sublattice ordering. The compressive strain loading leads to tetragonal lattice parameters with a / c =

1.039. We calculated the XRD patterns based on an ordered Li sublattice, where Li fully occupy 8*a*, 16*f*, and 32*g* sites (Fig. 6.2a), and a disordered Li sublattice, where Li partially occupy 24*d* and 96*h* sites (Fig. 6.2b). We then compared them with the pattern calculated from the compressed sample (Fig. 6.2c). The pattern from the Li sublattice in the compressed sample (Fig. 6.2c) matches well with the pattern from the one with an ordered Li sublattice (Fig. 6.2a). This confirms that the 3% compressive strain can induce an disorder-order transition in Al doped c-LLZO. The ordered Li sublattice then leads to the ionic diffusion slowing down.

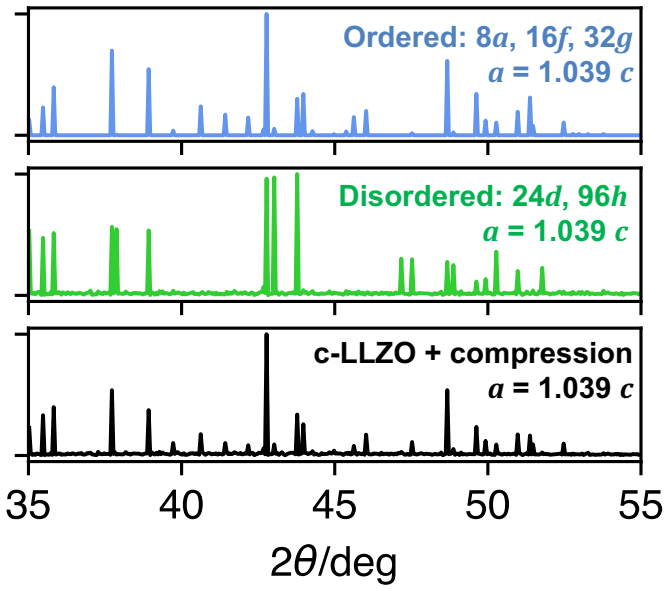

Figure 6.2. Calculated virtual XRD patterns of Li sublattice in a tetragonal lattice. The lattice parameters is fixed to $a / c = 1.039$, corresponds to a 3% compressive strain loading. The sublattice orderings are a) ordered Li sublattice (fully occupied 8*a*, 16*f*, and 32*g* sites) b) disordered Li sublattice (partially occupied 24*d* and 96*h* sites) c) Al doped c-LLZO under 3% compressive strain loading and after equilibrium. The pattern in c) matches the pattern in a), confirming the Li sublattice in the deformed c-LLZO changes to an ordered one.

The coupling between the lattice parameters and sublattice ordering is probably the origin of this strain-induced order-disorder transition in lithium garnet.[23] To further explore the strain-induced order-disorder transition in lithium garnet, we also studied the strain effect on undoped LLZO ($Li_7La_3Zr_2O_{12}$).

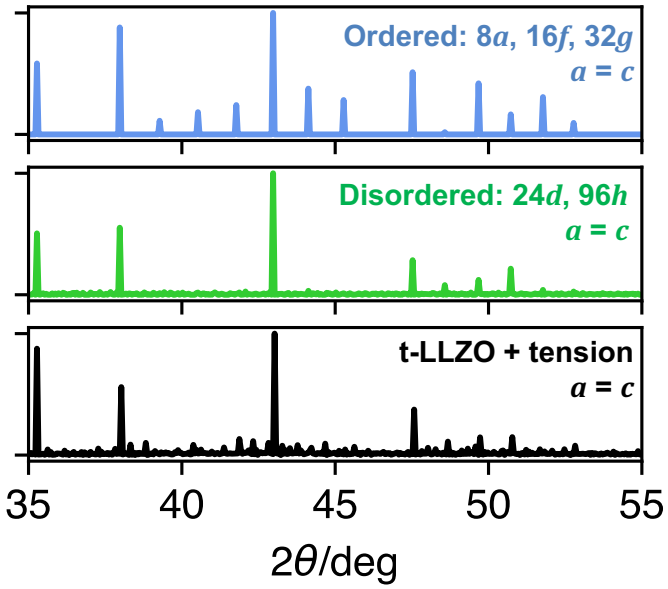

Figure 6.3. Calculated virtual XRD patterns of Li sublattice in a cubic lattice. The lattice parameters are fixed to $a / c = 1$. The sublattice orderings are a) ordered Li sublattice (fully occupied 8*a*, 16*f*, and 32*g* sites) b) disordered Li sublattice (partially occupied 24*d* and 96*h* sites) c) from undoped t-LLZO under a tensile strain loading to cubic lattice parameters. The pattern in c) matches the pattern in b), confirming the Li sublattice in deformed t-LLZO changes to a disordered one.

The undoped LLZO naturally stays at tetragonal phase with ordered Li sublattice below the transition temperature. We applied a tensile strain loading and deform the sample of undoped t-LLZO, forcing it to have cubic lattice parameters, i.e. $a = b = c$. The lattice parameters are extrapolated from the cubic phase lattice parameters of undoped LLZO

above the transition temperature (Fig. C1). Then we used the same method to calculated the virtual XRD pattern.

Fig. 6.3 shows the XRD pattern of Li sublattice in the deformed t-LLZO sample with a cubic lattice. By comparing with the pattern from ordered Li sublattice (fully occupied 8*a*, 16*f*, and 32*g* sites, Fig. 6.3a), and the pattern from disordered Li sublattice (partially occupied 24*d* and 96*h* sites, Fig. 6.3b), we found that the pattern from t-LLZO sample under tensile loading (Fig. 6.3c) matches the one with disordered Li sublattice (Fig. 6.3b). Therefore, we confirmed that strain can also induce an order-disorder transition in undoped t-LLZO.

6.3 Discussion

Our study revealed the effect of mechanical deformation on the ion diffusion in lithium garnet. Both tensile and compressive strain would decrease the ion diffusivity in c-LLZO. At moderate strain, the decrease in ion diffusion is minor in c-LLZO, and the activation energy does not show any significant change.

A compressive deformation on c-LLZO changes its lattice into a tetragonal lattice. The lattice parameters are coupled with the Li sublattice ordering. Therefore, the compressive deformation can transform the original disordered Li sublattice into ordered sublattice similar to that in t-LLZO. The ordered Li sublattice results in a significant decrease in conductivity.

The order-disorder transition induced by mechanical deformation can also be used to facilitate Li-ion diffusion. The undoped LLZO stays at tetragonal phase below the transition temperature, with an ordered Li sublattice and low ionic conductivity. By

applying a tensile mechanical deformation on t-LLZO and changing the lattice into a cubic lattice, a Li sublattice undergoes an order-disorder transition. The Li sublattice transform into a disordered sublattice, like that in c-LLZO. This sublattice change leads to a c-LLZO type ionic diffusion, which have significant higher ionic conductivity compared to the undeformed t-LLZO.

Chapter 7. Conclusion and Future Work

7.1 Conclusions

The major conclusions of this dissertation are summarized below.

1) Most solid electrolytes have limited electrochemical stability window, especially the sulfide based solid electrolytes. Conventional CV experiments would overestimate the intrinsic electrochemical window of solid electrolytes.
2) The poor stability at the solid electrolyte–electrode interface indicates a strong thermodynamic driving force of decomposition, which leads to the spontaneous formation of interphase layers.
3) The interphase layers have a significant impact on the battery performance. MIEC interphase layer cannot provide passivation, which can lead to continuous decomposition and high interfacial resistance, while SEI-type interphase layer can provide the essential passivation and protect the solid electrolytes from further reduction.
4) For interface with poor stability, applying coating layer materials is a practical engineering strategy to improve the interface stability and to decrease the interfacial resistance.
5) Material stability against lithium metal is governed by cation and anion chemistry. Metal cations in oxides, sulfides, and fluorides are usually reduced by lithium metal, leading to poor stability against lithium metal.
6) Nitride anion chemistry shows unique stability against Li metal. In general, metal nitrides have a significantly lower reduction potential than oxides, sulfides, and fluorides.

7) Many nitrides that have intrinsic lithium metal stability can be used as buffer layers to protect materials from lithium metal reduction. Enriching nitrogen content at the interface with lithium metal can potential leads to the formation of a stable, passivating SEI, transforming a lithium-unstable interface into a lithium-stable interface.
8) Grain boundary slows down the ionic diffusion in lithium super-ionic conducting materials.
9) Strain can induce order-disorder transition in lithium garnet materials, and this transition has a significant effect on the ionic diffusion.

7.2 Future Work

To improve the performance and reliability of all-solid-state Li-ion battery, interface stability is a critical factor that need to be considered. This dissertation revealed the intrinsic electrochemical window of solid electrolyte is narrow, and the formed interphase plays a crucial role in interfacial stability. However, there are more issues regarding the stability and interface issues in all-solid-state Li-ion batteries.

A few possible future directions are listed below.

1) Despite the high ionic conductivity and easy processing, sulfide-based solid electrolytes are generally quite sensitive to moisture, posing difficulty for manufacturing process. The moisture sensitivity can also be assessed by computations. Such knowledge would be useful to improve the moisture resistivity of sulfide-based solid electrolytes.

2) For the grain boundary in solid electrolytes, I only looked into a few selected orientation grain boundaries within one typical solid electrolyte (lithium garnet). It might be worthwhile to look into grain boundaries with other orientations and terminations, or in other solid electrolyte materials, to get a more comprehensive understanding on the grain boundary diffusion in solid electrolytes.
3) In this dissertation, I observed the strain-induced order-disorder transition in lithium garnet. Such coupling between strain and order-disorder transition may not be only limited to lithium garnet. Other materials with order-disorder transition may also have similar behavior. It may be worth to investigate the strain effect on other super ionic conductor materials.

Publications, Patents, and Presentations

Publications

1) **Y. Zhu**, X. He, Y. Mo, Origin of outstanding stability in the lithium solid electrolyte materials: insights from thermodynamic analyses based on first principles calculations. ***ACS Applied Materials & Interfaces***, 7, 23685-23693, (2015)

2) **Y. Zhu**, X. He, Y. Mo, First principles study on electrochemical and chemical stability of solid electrolyte–electrode interfaces in all-solid-state Li-ion batteries. ***Journal of Materials Chemistry A***, 4, 3253-3266, (2016) **(Featured front cover,** selected as the **"2016 Journal of Materials Chemistry A HOT Papers"** and **editorial "most highly cited original research articles in 2016")**

3) **Y. Zhu**, X. He, Y. Mo, Strategies based on nitride materials chemistry to stabilize Li metal anode. ***Advanced Science***, 1600517, (2017)

4) F. Han[§], **Y. Zhu**[§], X. He, Y. Mo, C. Wang, Electrochemical stability of $Li_{10}GeP_2S_{12}$ and $Li_7La_3Zr_2O_{12}$ solid electrolytes. ***Advanced Energy Materials***, 6, 1501590, (2016) **([§] co first-authors)**

5) X. He, **Y. Zhu**, Y. Mo, Origin of fast ion diffusion in super-ionic conductors. ***Nature Communication***, 6, (2017)

6) K. H. Park, Q. Bai, D. H. Kim, D. Y. Oh, **Y. Zhu**, Y. Mo, Y. S. Jung, Design Strategies, Practical Considerations, and New Solution Processes of Sulfide Solid Electrolytes for All-Solid-State Batteries, ***Advanced Energy Materials***, 8, 1800035, (2018)

7) X. Fan, E. Hu, J. Li, **Y. Zhu**, *et al*., High energy-density and reversibility of iron fluoride cathode enabled via an intercalation-extrusion reaction, ***Nature Communication***, 9, 2324 (2018)

8) X. He, **Y. Zhu**, A. Epstein, Y. Mo, Statistical variances of diffusional properties from ab initio molecular dynamics simulations. ***npj Computational Materials***. 4 (1), (2018)

9) K. He, S. Zhang, J. Li, X. Yu, Q. Meng, **Y. Zhu**, *et al*., Visualizing non-equilibrium lithiation of spinel oxide via *in situ* transmission electron microscopy, ***Nature Communication***, 7, 11441 (2016)

10) W. Luo, Y. Gong, **Y. Zhu**, *et al*., Transition from super-lithiophobicity to super-lithiophilicity of garnet solid-state electrolyte, ***Journal of the American Chemical Society***, 138 (37), 12258, (2016)

11) W. Luo, Y. Gong, **Y. Zhu**, *et al*., Reducing interfacial resistance between garnet-structured solid-state electrolyte and Li metal anode by a germanium Layer, ***Advanced Materials***, 29 (22), 1606042, (2017)

12) K. He, F. Lin, **Y. Zhu**, *et al*., Sodiation kinetics of metal oxide conversion electrodes: a comparative study with lithiation. ***Nano Letters,*** 15, 5755-5763 (2015)

13) J. Li, K. He, Q. Meng, X. Li, **Y. Zhu**, *et al*., Kinetic phase evolution of spinel cobalt oxide during lithiation. ***ACS Nano***, 10, 9577 (2016)

14) K. K. Fu, Y. Gong, B. Liu, **Y. Zhu**, *et al*., Toward garnet electrolyte–based Li metal batteries: An ultrathin, highly effective, artificial solid-state electrolyte/metallic Li interface. ***Science Advance***, 3(4), 1601659 (2017)

15) K. K. Fu, Y. Gong, S. Xu, **Y. Zhu**, *et al*., Stabilizing the Garnet Solid-Electrolyte/Polysulfide Interface in Li-S Batteries. ***Chemistry of Materials***, 29, 8037 (2017)

16) Q. Bai, **Y. Zhu**, X. He, E. Wachsman, Y. Mo, First principles hybrid functional study of small polarons in doped $SrCeO_3$ perovskite: towards computation design of materials with tailored polaron. ***Ionics***. 15, 5755-5763 (2017)

17) Q. Bai, X. He, **Y. Zhu**, Y. Mo, First Principles Study of Oxyhydride H-Ion Conductors: Toward Facile Anion Conduction in Oxide-Based Materials. ***ACS Applied Energy Materials***.15, 5755-5763 (2018)

Patents

1) C. Wang, Y. Mo, **Y. Zhu**, F. Han, X. Zhu, J. Yue, Novel Strategies to Stabilize Li Metal Anode Application Number: US 62/637,584.

Presentations

1) **Y. Zhu**, X. He, Y. Mo., Atomistic Modeling of Interface Transport in All-Solid-State Li-ion batteries, Materials Research Society, Phoenix, Arizona (2018)

2) **Y. Zhu**, X. He, Y. Mo., Novel Strategies for Lithium Metal Anode Protection Based on Nitride Materials Chemistry: Insight from First Principles Calculations, 232nd Electrochemical Society Meeting, National Harbor, Maryland (2017)

3) **Y. Zhu**, X. He, Y. Mo., Electrochemical and Chemical Stability of Solid Electrolyte–Electrode Interfaces: A First Principles Computation Study, 232nd Electrochemical Society Meeting, National Harbor, Maryland (2017)

4) **Y. Zhu**, X. He, Y. Mo. "Novel Strategies for Lithium Metal Anode Protection based on Nitride Materials Chemistry", American Chemical Society, Washington, DC. (2017)
5) **Y. Zhu**, X. He, Y. Mo. "Interface Engineering Guided by First Principles Computation – Towards Enabling Li metal In All-Solid-State Li-ion Batteries", Materials Research Society, Boston (2016)
6) **Y. Zhu**, X. He, Y. Mo., First principles study of solid electrolyte–electrode interfaces in all-solid-state Li-ion batteries, The Society of Engineering Science, 53rd Annual Technical Meeting, Maryland (2016)
7) **Y. Zhu**, X. He, Y. Mo., "First Principles Study of Electrochemical and Chemical Stability of the Solid Electrolyte–Electrode Interfaces in All-Solid-State Li-Ion Batteries", American Physics Society, Baltimore (2016)
8) Y. Mo, **Y. Zhu**., "Problems at the Electrolyte–Electrode Interfaces in All-Solid-State Li-Ion Batteries: Insight from First-Principles Computation", Materials Research Society, Boston (2015)

Appendices

Appendix A

1. Materials systems

The crystal structures and the phase equilibria of the commonly used solid electrolyte materials investigated in this study are summarized in Table A1. The energies of most materials in this study were obtained from the MP database.[34] The materials that were not included in MP database were calculated on the basis of the experimentally determined structures. For the structures with disordered site occupancies, we sampled 50-60 different configurations using the same method in the previous studies[13,162] and chose the configuration with the lowest energy as the ground state structure. For example, the ground state structure of $Li_{0.33}La_{0.56}TiO_3$ (LLTO) material was ordered from the experimental structure determined in ref. [163]. The Li_3PS_4 phase based on the $Pmn2_1$ γ phase[164] was determined to have the lowest energy among its polymorphs and was added into the phase diagrams including Li-P-S compositions.

For the materials with a non-zero energy above hull, we evaluated the electrochemical window of the material by reducing the energy above hull to zero. These solid electrolyte materials may be entropically stabilized by the disordering of Li and other ions as in the LGPS.[13]

For those materials, such as $Li_{3.25}Ge_{0.25}P_{0.75}S_4$, $Li_{1.5}Al_{0.5}Ge_{1.5}(PO_4)_3$ and $Li_7P_2S_8I$, that have no experimentally determined structures from the ICSD database, the materials entries were constructed as the phase equilibria at the given composition with a zero energy above hull. There is no experimentally determined crystal structure available for the LiPON material systems, which are typically amorphous with a range of compositions. We added

the crystalline structure of Li_2PO_2N reported in Ref. [165] as a representative of the LiPON materials systems. We also used $Li_{2.88}PO_{3.73}N_{0.14}$ and $Li_{2.98}PO_{3.3}N_{0.46}$ as typical representative LiPON phase.

Table A1. Crystal structures and phase equilibria of solid electrolyte materials

Composition	Acronym	Structure used	E above hull (meV/atom)	Phase equilibria
$Li_{10}GeP_2S_{12}$	LGPS	mp-696138[166]	21	Li_3PS_4, Li_4GeS_4
$Li_{3.25}Ge_{0.25}P_{0.75}S_4$		-	-	Li_3PS_4, Li_4GeS_4
Li_3PS_4		[164]	0	Li_3PS_4
Li_4GeS_4		mp-30249[167]	0	Li_4GeS_4
$Li_7P_3S_{11}$		mp-641703[4]	22	Li_3PS_4, P_2S_5
Li_6PS_5Cl		[168]	83	Li_3PS_4, Li_2S, LiCl
$Li_7P_2S_8I$		-	-	Li_3PS_4, LiI
Li_2PO_2N	LiPON	[165]	0	Li_2PO_2N
$Li_7La_3Zr_2O_{12}$	LLZO	[169]	7	Li_2O, La_2O_3, $Li_6Zr_2O_7$
$Li_{0.33}La_{0.56}TiO_3$	LLTO	[163]	68	TiO_2, $Li_4Ti_5O_{12}$, $La_2Ti_2O_7$
$Li_{1.3}Ti_{1.7}Al_{0.3}(PO_4)_3$	LATP	[170]	29	$LiTi_2(PO_4)_3$, Li_3PO_4, $AlPO_4$
$Li_{1.5}Al_{0.5}Ge_{1.5}(PO_4)_3$	LAGP	-	-	$AlPO_4$, $Ge_5O(PO_4)_6$, GeO_2, $Li_4P_2O_7$
$Li_{3.5}Zn_{0.25}GeO_4$	LISICON	[171]	34	Li_2ZnGeO_4, Li_4GeO_4

2. Calculated plateaus for the lithiation and delithiation of solid electrolyte materials.

Table A2. Calculated plateaus for the lithiation and delithiation of solid electrolyte materials.

(a) $Li_{10}GeP_2S_{12}$

Potential ϕ ref to Li/Li^+(V)	μ_{Li} ref to Li (eV)	Δn_{Li} per formula	Phase equilibria
0.28	-0.28	23.75	Li_2S, $Li_{15}Ge_4$, Li_3P
0.45	-0.45	22.25	Li_9Ge_4, Li_2S, Li_3P
0.56	-0.56	21	Li_3P, Li_2S, LiGe
0.87	-0.87	20	Li_3P, Li_2S, Ge
0.93	-0.93	16	Li_2S, LiP, Ge
1.17	-1.17	14.86	Li_3P_7, Li_2S, Ge
1.30	-1.30	14.29	Ge, Li_2S, LiP_7
1.62	-1.62	14	Li_2S, P, Ge
1.71	-1.71	10	Li_4GeS_4, P, Li_2S
		0	$Li_{10}GeP_2S_{12}$
2.14	-2.14	-4	GeS_2, Li_3PS_4, S
2.31	-2.31	-10	P_2S_5, GeS_2, S

(b) $Li_{3.25}Ge_{0.25}P_{0.75}S_4$

Potential ϕ ref to Li/Li^+(V)	μ_{Li} ref to Li (eV)	Δn_{Li} per formula	Phase equilibria
0.28	-0.28	23.75	Li_2S, $Li_{15}Ge_4$, Li_3P
0.45	-0.45	22.25	Li_9Ge_4, Li_2S, Li_3P
0.56	-0.56	21	Li_3P, Li_2S, LiGe
0.87	-0.87	20	Li_3P, Li_2S, Ge
0.93	-0.93	16	Li_2S, LiP, Ge
1.17	-1.17	14.86	Li_3P_7, Li_2S, Ge
1.30	-1.30	14.29	Ge, Li_2S, LiP_7
1.62	-1.62	14	Li_2S, P, Ge
1.71	-1.71	10	Li_4GeS_4, P, Li_2S
		0	$Li_{3.25}Ge_{0.25}P_{0.75}S_4$
2.14	-2.14	-4	GeS_2, Li_3PS_4, S
2.31	-2.31	-10	P_2S_5, GeS_2, S

(c) Li_4GeS_4

Potential ϕ ref to Li/Li^+(V)	μ_{Li} ref to Li (eV)	Δn_{Li} per formula	Phase equilibria
0.28	-0.28	7.75	Li_2S, $Li_{15}Ge_4$
0.45	-0.45	6.25	Li_9Ge_4, Li_2S
0.56	-0.56	5	Li_2S, LiGe
1.62	-1.62	4	Li_2S, Ge
		0	Li_4GeS_4
2.14	-2.14	-4	GeS_2, S

(d) Li_6PS_5Cl

Potential ϕ ref to Li/Li^+(V)	μ_{Li} ref to Li (eV)	Δn_{Li} per formula	Phase equilibria
0.87	-0.87	8	Li_3P, Li_2S, LiCl
0.93	-0.93	6	LiP, Li_2S, LiCl
1.17	-1.17	5.43	Li_3P_7, Li_2S, LiCl
1.30	-1.30	5.14	LiP_7, Li_2S, LiCl
1.71	-1.71	5	P, Li_2S, LiCl
		0	Li_6PS_5Cl
2.01	-2.01	-2	Li_3PS_4, S, LiCl
2.31	-2.31	-5	P_2S_5, S, LiCl
2.88	-2.88	-6	P_2S_5, S, PCl_3

(e) Li_3PS_4

Potential ϕ ref to Li/Li^+(V)	μ_{Li} ref to Li (eV)	Δn_{Li} per formula	Phase equilibria
0.87	-0.87	8	Li_3P, Li_2S
0.93	-0.93	6	LiP, Li_2S
1.17	-1.17	5.43	Li_3P_7, Li_2S
1.30	-1.30	5.14	LiP_7, Li_2S
1.71	-1.71	5	P, Li_2S
		0	Li_3PS_4
2.31	-2.31	-3	P_2S_5, S

(f) $Li_7P_2S_8I$

Potential ϕ ref to Li/Li^+(V)	μ_{Li} ref to Li (eV)	Δn_{Li} per formula	Phase equilibria
0.87	-0.87	16	Li_3P, Li_2S, LiI
0.93	-0.93	12	LiP, Li_2S, LiI
1.17	-1.17	10.86	Li_3P_7, Li_2S, LiI
1.30	-1.30	10.29	LiP_7, Li_2S, LiI
1.71	-1.71	10	P, Li_2S, LiI
		0	$Li_7P_2S_8I$
2.31	-2.31	-6	P_2S_5, S, LiI
2.47	-2.47	-7	P_2S_5, S, I

(g) $Li_7P_3S_{11}$

Potential ϕ ref to Li/Li^+(V)	μ_{Li} ref to Li (eV)	Δn_{Li} per formula	Phase equilibria
0.87	-0.87	24	Li_3P, Li_2S
0.93	-0.93	18	LiP, Li_2S
1.17	-1.17	16.29	Li_3P_7, Li_2S
1.30	-1.30	15.43	LiP_7, Li_2S
1.71	-1.71	15	P, Li_2S
2.03	-2.03	1.25	Li_3PS_4, P
2.15	-2.15	1.08	Li_3PS_4, P_4S_3
2.24	-2.24	0.67	Li_3PS_4, P_4S_7
2.28	-2.28	0.29	Li_3PS_4, P_4S_9
		0	$Li_7P_3S_{11}$
2.31	-2.31	-7	P_2S_5, S

(h) LiPON

Potential ϕ ref to Li/Li^+(V)	μ_{Li} ref to Li (eV)	Δn_{Li} per formula	Phase equilibria
0.01	-0.01	8	Li_3P, Li_3N, Li_2O
0.61	-0.61	6	Li_3P, Li_7PN_4, Li_2O
0.68	-0.68	4	Li_3P, $LiPN_2$, Li_2O
		0	Li_2PO_2N
2.63	-2.63	-0.86	P_3N_5, $Li_4P_2O_7$, N_2
2.75	-2.75	-0.92	P_4ON_6, $Li_4P_2O_7$, N_2
2.77	-2.77	-1.36	P_4ON_6, $LiPO_3$, N_2
3.05	-3.05	-1.50	PON, $LiPO_3$, N_2
3.63	-3.63	-2	PON, P_2O_5, N_2

(i) LLZO

Potential ϕ ref to Li/Li^+(V)	μ_{Li} ref to Li (eV)	Δn_{Li} per formula	Phase equilibria
0.004	0.004	8	Zr, La_2O_3, Li_2O
0.048	-0.048	6.67	Zr_3O, La_2O_3, Li_2O
		0	$Li_7La_3Zr_2O_{12}$
2.91	-2.91	-0.50	Li_2O_2, La_2O_3, $Li_6Zr_2O_7$
3.17	-3.17	-3.50	Li_2O_2, La_2O_3, $La_2Zr_2O_7$
3.30	-3.30	-7	O_2, La_2O_3, $La_2Zr_2O_7$

(j) LLTO

Potential ϕ ref to Li/Li^+(V)	μ_{Li} ref to Li (eV)	Δn_{Li} per formula	Phase equilibria
0.018	-0.018	3.67	Ti_6O, La_2O_3, Li_2O
0.12	-0.12	3.33	Ti_3O, La_2O_3, Li_2O
0.29	-0.29	1.67	Ti_3O, La_2O_3, Li_4TiO_4
0.37	-0.37	1.57	Ti_2O, La_2O_3, Li_4TiO_4
0.46	-0.46	0.92	$LiTiO_2$, La_2O_3, Li_4TiO_4
0.50	-0.50	0.64	$LiTiO_2$, La_2TiO_5, Li_4TiO_4
1.12	-1.12	0.56	$LiTiO_2$, La_2TiO_5, Li_2TiO_3
1.14	-1.14	0.28	$LiTi_2O_4$, La_2TiO_5, Li_2TiO_3
1.63	-1.63	0.14	$LiTi_2O_4$, $La_2Ti_2O_7$, Li_2TiO_3
1.749	-1.749	0.09	$Li_{7/6}Ti_{11/6}O_4$, $La_2Ti_2O_7$, Li_2TiO_3
1.752	-1.752	0.01	$Li_{7/6}Ti_{11/6}O_4$, $La_2Ti_2O_7$, $Li_4Ti_5O_{12}$
		0	$Li_{0.33}La_{0.56}TiO_3$
3.71	-3.71	-0.33	O_2, $La_2Ti_2O_7$, TiO_2

(k) LAGP

Potential ϕ ref to Li/Li^+(V)	μ_{Li} ref to Li (eV)	Δn_{Li} per formula	Phase equilibria
0.06	-0.06	38.25	Li_2O, $Li_{15}Ge_4$, Li_3P, Li_9Al_4
0.28	-0.28	35.63	Li_2O, $Li_{15}Ge_4$, Li_3P, Li_5AlO_4
0.45	-0.45	33.38	Li_2O, Li_9Ge_4, Li_3P, Li_5AlO_4
0.56	-0.56	31.50	Li_2O, LiGe, Li_3P, Li_5AlO_4
0.69	-0.69	30	Li_2O, Ge, Li_3P, Li_5AlO_4
0.75	-0.75	10	Li_3PO_4, Ge, Li_3P, Li_5AlO_4
0.87	-0.87	8	Li_3PO_4, Ge, Li_3P, $LiAlO_2$
0.93	-0.93	7.50	Li_3PO_4, Ge, LiP, $LiAlO_2$
1.17	-1.17	7.36	Li_3PO_4, Ge, Li_3P_7, $LiAlO_2$
1.30	-1.30	7.29	Li_3PO_4, Ge, LiP_7, $LiAlO_2$
1.49	-1.49	7.25	Li_3PO_4, Ge, P, $LiAlO_2$
1.94	-1.94	7	Li_3PO_4, Ge, P, $LiAl_5O_8$
2.64	-2.64	6	Li_3PO_4, Ge, $AlPO_4$
2.70	-2.70	3.50	Ge, GeO_2, $Li_4P_2O_7$, $AlPO_4$
		0	$Li_{1.5}Al_{0.5}Ge_{1.5}(PO_4)_3$
4.27	-4.27	-0.10	$Ge_5O(PO_4)_6$, O_2, $Li_4P_2O_7$, $AlPO_4$
4.31	-4.31	-1.50	$Ge_5O(PO_4)_6$, O_2, GeP_2O_7, $AlPO_4$

(l) LATP

Potential ϕ ref to Li/Li^+(V)	μ_{Li} ref to Li (eV)	Δn_{Li} per formula	Phase equilibria
0.026	-0.026	30.30	Ti_3P, TiAl, Li_3P, Li_2O
0.082	-0.082	29.60	Ti_2P, TiAl, Li_3P, Li_2O
0.088	-0.088	29.38	Ti_2P, $TiAl_2$, Li_3P, Li_2O
0.23	-0.23	28.25	Ti_2P, Li_5AlO_4, Li_3P, Li_2O
0.69	-0.69	24	Li_4TiO_4, Li_5AlO_4, Li_3P, Li_2O
0.75	-0.75	16	Li_4TiO_4, Li_5AlO_4, Li_3P, Li_3PO_4
0.79	-0.79	14.80	Li_4TiO_4, $LiAlO_2$, Li_3P, Li_3PO_4
0.86	-0.86	8.33	Li_4TiO_4, $LiAlO_2$, TiP, Li_3PO_4
1.49	-1.49	7.33	Li_2TiO_3, $LiAlO_2$, TiP, Li_3PO_4
1.55	-1.55	6.52	$LiTi_2O_4$, $LiAlO_2$, TiP, Li_3PO_4
1.71	-1.71	6.35	$LiTi_2O_4$, $LiAl_5O_8$, TiP, Li_3PO_4
1.84	-1.84	5.82	TiO_2, $LiAl_5O_8$, TiP, Li_3PO_4
1.94	-1.94	5.43	TiO_2, $LiAl_5O_8$, TiP_2, Li_3PO_4
1.98	-1.98	4.76	TiO_2, $AlPO_4$, TiP_2, Li_3PO_4
2.12	-2.12	4.25	TiO_2, $AlPO_4$, P, Li_3PO_4
2.17	-2.17	2.13	$LiTiPO_5$, $AlPO_4$, P, Li_3PO_4
		0	$Li_{1.3}Ti_{1.7}Al_{0.3}P_3O_{12}$
4.21	-4.21	-0.15	$LiTi_2(PO_4)_3$, $AlPO_4$, $Li_4P_2O_7$, O_2
4.33	-4.33	-0.60	$LiTi_2(PO_4)_3$, $AlPO_4$, TiP_2O_7, O_2

4.66	-4.66	-1.30	$Ti_5P_4O_{20}$, $AlPO_4$, TiP_2O_7, O_2

(m) LISICON

Potential ϕ ref to Li Li/Li^+(V)	μ_{Li} ref to Li (eV)	Δn_{Li} per formula	Phase equilibria
0.18	-0.18	8.50	Li_2O, $Li_{15}Ge_4$, LiZn
0.28	-0.28	7.85	Li_2O, $Li_{15}Ge_4$, $Li_8Zn_2Ge_3$
0.42	-0.42	6.91	Li_2O, Li_9Ge_4, $Li_8Zn_2Ge_3$
0.45	-0.45	6.69	Li_2O, Li_9Ge_4, Li_2ZnGe
0.56	-0.56	5.75	Li_2O, LiGe, Li_2ZnGe
0.61	-0.61	5	Li_2O, Ge, Li_2ZnGe
0.73	-0.73	4.75	Li_2O, Ge, LiZnGe
1.02	-1.02	4.50	Li_2O, Ge, Zn
1.44	-1.44	0.50	Li_4GeO_4, Zn
		0	$Li_{3.5}Zn_{0.25}GeO_4$
3.39	-3.39	-1.50	Li_2ZnGeO_4, Li_2GeO_3, O_2
3.84	-3.84	-2.40	Li_2ZnGeO_4, $Li_4Ge_5O_{12}$, O_2
3.85	-3.85	-2.79	Li_2ZnGeO_4, $Li_2Ge_7O_{15}$, O_2
3.89	-3.89	-3.19	$LiZn_{1.5}Ge_3O_8$, $Li_2Ge_7O_{15}$, O_2
3.98	-3.98	-3.33	$LiZn_{1.5}Ge_3O_8$, GeO_2, O_2
4.00	-4.00	-3.50	Zn_2GeO_4, GeO_2, O_2

3. Calculated plateaus for the lithiation and delithiation of coating layer materials.

Table A3. Calculated plateaus for the lithiation and delithiation of coating layer materials.

(a) $LiTaO_3$

Potential ϕ ref to Li/Li$^+$(V)	μ_{Li} ref to Li metal (eV)	Δn_{Li} per formula	Phase equilibria
0.35	-0.35	5	Ta, Li_2O
0.54	-0.54	2	Ta, Li_5TaO_5
1.18	-1.18	1.25	Ta, Li_3TaO_4
		0	$LiTaO_3$
3.95	-3.95	-0.67	$LiTa_3O_8$, O_2
4.12	-4.12	-1	Ta_2O_5, O_2

(b) $LiNbO_3$

Potential ϕ ref to Li/Li$^+$(V)	μ_{Li} ref to Li (eV)	Δn_{Li} per formula	Phase equilibria
0.55	-0.55	5	Nb, Li_2O
0.62	-0.62	2	$LiNbO_2$, Li_2O
0.94	-0.94	1.2	$LiNbO_2$, $Li_8Nb_2O_9$
1.74	-1.74	1	$LiNbO_2$, Li_3NbO_4
		0	$LiNbO_3$
3.88	-3.88	-0.67	$LiNb_3O_8$, O_2
3.92	-3.92	-1	Nb_2O_5, O_2

(c) $Li_4Ti_5O_{12}$

Potential ϕ ref to Li/Li^+(V)	μ_{Li} ref to Li (eV)	Δn_{Li} per formula	Phase equilibria
0.018	-0.018	18.33	Ti_6O, Li_2O
0.12	-0.12	16.67	Ti_3O, Li_2O
0.29	-0.29	7.27	Ti_3O, Li_4TiO_4
0.37	-0.37	6.86	Ti_2O, Li_4TiO_4
0.50	-0.50	4	$LiTiO_2$, Li_4TiO_4
1.12	-1.12	3	$LiTiO_2$, Li_2TiO_3
1.63	-1.63	1.5	$LiTi_2O_4$, Li_2TiO_3
1.75	-1.75	1	$Li_{7/6}Ti_{11/6}O_4$, Li_2TiO_3
		0	$Li_4Ti_5O_{12}$
3.71	-3.71	-4	O_2, TiO_2

(d) Li_2SiO_3

Potential ϕ ref to Li/Li^+(V)	μ_{Li} ref to Li (eV)	Δn_{Li} per formula	Phase equilibria
0.10	-0.10	8.2	$Li_{21}Si_5$, Li_2O
0.23	-0.23	7.25	$Li_{13}Si_4$, Li_2O
0.26	-0.26	3.62	$Li_{13}Si_4$, Li_8SiO_6
0.26	-0.26	1.81	$Li_{13}Si_4$, Li_4SiO_4
0.37	-0.37	1.43	$Li_{12}Si_7$, Li_4SiO_4
0.39	-0.39	1.25	LiSi, Li_4SiO_4
0.76	-0.76	1	Si, Li_4SiO_4
		0	Li_2SiO_3
3.74	-3.74	-1	$Li_2Si_2O_5$, O_2
3.78	-3.78	-2	SiO_2, O_2

(e) Li_3PO_4

Potential ϕ ref to Li/Li^+(V)	μ_{Li} ref to Li (eV)	Δn_{Li} per formula	Phase equilibria
0.69	-0.69	8	Li_3P, Li_2O
		0	Li_3PO_4
4.21	-4.21	-1	$Li_4P_2O_7$, O_2
4.33	-4.33	-2	$LiPO_3$, O_2
4.99	-4.99	-3	P_2O_5, O_2

Appendix B

1. List of Compounds.

The lithium ternary compounds Li-M-X (X = N, O, S, F) investigated in Fig. 4.1 are summarized in Table 4.3. The structures and energies of most compounds were obtained from the Materials Project (MP) database. We added 26 additional lithium ternary compounds (Table 4.4), of which 21 were predicted using substitution prediction algorithm and 5 were from Inorganic Crystal Structure Database (ICSD).

Table B1. Lithium ternary compounds Li-M-X (X = N, O, S, F)

Cation	Ternary Compounds Li-M-X	Cation	Ternary Compounds Li-M-X
Er^{3+}	$LiErO_2$, $LiErS_2$	Tm^{3+}	$LiTmO_2$
Ho^{3+}	$LiHoO_2$, $LiHoS_2$	Y^{3+}	$LiYO_2$, $LiYS_2$, $LiYF_4$
Gd^{3+}	$LiGdO_2$	Sm^{3+}	$LiSmS_2$
Ca^{2+}	LiCaN	Be^{2+}	LiBeN, Li_2BeF_4
Sr^{2+}	LiSrN, Li_4SrN_2	Mg^{2+}	LiMgN
Sc^{3+}	Li_3ScN_2, $LiScO_2$, $LiScS_2$	Hf^{4+}	Li_2HfN_2, Li_2HfO_3, $Li_6Hf_2O_7$, Li_2HfF_6
Zr^{4+}	Li_2ZrN_2, $Li_6Zr_2O_7$, $Li2ZrO_3$, Li_2ZrS_3, Li_4ZrF_8, Li_2ZrF_6, $Li_3Zr_4F_{19}$	Na^{+}	LiNaS
K^{+}	LiKS	Ce^{4+}	Li_2CeN_2, Li_2CeO_3, $LiCeF_5$

Al^{3+}	Li_3AlN_2, $LiAl_5O_8$, $LiAlO_2$, Li_5AlO_4, $LiAlS_2$, Li_5AlS_4, Li_3AlF_6	Si^{4+}	Li_5SiN_3, Li_2SiN_2, $LiSi_2N_3$ Li_2SiO_3, $Li_2Si_2O_5$, Li_8SiO_6, Li_4SiO_4, Li_8SiS_6, Li_2SiS_3, Li_2SiF_6
Zn^{2+}	LiZnN, $Li_{10}Zn_4O_9$, Li_6ZnO_4, Li_2ZnF_4	In^{3+}	$LiInO_2$, $LiInF_4$
Ta^{5+}	Li_4TaN_3, Li_7TaN_4, $LiTaN_2$, $LiTa_3O_8$, Li_5TaO_5, $LiTaO_3$, Li_3TaO_4, Li_3TaS_4, $LiTaF_6$	Ti^{4+}	Li_2TiN_2, Li_5TiN_3, Li_4TiO_4, Li_2TiO_3, $Li_4Ti_5O_{12}$, Li_2TiS_3, Li_2TiF_6
Sn^{4+}	Li_2SnN_2, Li_8SnO_6, Li_2SnO_3, Li_2SnS_3, Li_2SnF_6	B^{3+}	Li_3BN_2, $Li_2B_4O_7$, $LiBO_2$, Li_3BO_3, $Li_3B_7O_{12}$, Li_3BS_3, $Li_5B_7S_{13}$, $LiBF_4$
Ga^{3+}	Li_3GaN_2 $LiGaO_2$, Li_5GaO_4, $LiGa_5O_8$, $LiGaS_2$, Li_3GaF_6	Ni^{2+}	Li_2NiF_4
Nb^{5+}	Li_7NbN_4, $LiNbN_2$, $LiNbO_3$, $LiNb_3O_8$, Li_3NbO_4, $Li_8Nb_2O_9$ Li_3NbS_4, $LiNbF_6$	Fe^{3+}	Li_3FeN_2, $LiFeO_2$, Li_5FeO_4, Li_3FeF_6
Ge^{4+}	Li_5GeN_3, Li_2GeN_2, $LiGe_2N_3$, $Li_2Ge_7O_{15}$, Li_4GeO_4, $Li_4Ge_5O_{12}$, Li_2GeO_3 Li_2GeS_3, Li_4GeS_4, Li_2GeF_6	W^{6+}	Li_6WN_4, Li_2WO_4, Li_4WO_5

P^{5+}	$LiPN_2$, Li_7PN_4, $Li_4P_2O_7$, $LiPO_3$, Li_3PO_4, Li_3PS_4, $LiPF_6$	Mo^{6+}	Li_6MoN_4, Li_2MoO_4, Li_4MoO_5
V^{5+}	Li_7VN_4, $LiVN_2$, Li_3VO_4, $LiVO_3$, Li_3VS_4, $LiVF_6$	Mn^{4+}	$LiMn_2N_3$, Li_2MnN_2, Li_2MnO_3, $Li_4Mn_5O_{12}$, Li_2MnF_6
Co^{4+}	Li_8CoO_6		

Table B2. Additional lithium ternary compounds.

Compound	Form. E (eV/atom)	Space group	Structure source
$LiAlS_2$	-1.614	$P4_12_12$	S-O substitution from $LiAlO_2$ (ICSD-23815)
Li_5AlS_4	-1.583	Pcab	S-O substitution from Li_5AlO_4 (ICSD-42697)
Li_8SiS_6	-1.496	$P6_3cm$	S-O substitution from Li_8SiO_6 (ICSD-65176)
Li_2SiS_3	-1.385	$Ccm2_1$	S-O substitution from Li_2SiO_3 (ICSD-853)
Li_2SiF_6	-3.423	P321	ICSD-425923
Li_2GeN_2	-0.609	P-3m1	Ge-Zr substitution from Li_2ZrN_2 (ICSD-78790)
$LiGe_2N_3$	-0.516	$Cmc2_1$	Ge-Si substitution from $LiSi_2N_3$ (ICSD-34118)
Li_2GeS_3	-1.218	$Ccm2_1$	S-O substitution from Li_2GeO_3 (ICSD-100403)
Li_2SnN_2	-0.403	P-3m1	Sn-Zr substitution from Li_2ZrN_2 (ICSD-78790)
Li_2SnS_3	-1.211	C2/c	S-O substitution from Li_2SnO_3 (ICSD-21032)
Li_2SnF_6	-3.043	P-31m	Sn-Zr substitution from Li_2ZrF_6 (ICSD-2644)
Li_2TiN_2	-1.194	P-3m1	Ti-Zr substitution from Li_2ZrN_2 (ICSD-78790)
Li_2TiS_3	-1.668	C2/c	S-O substitution from Li_2TiO_3 (ICSD-15150)

Li_2ZrS_3	-1.800	C2/c	S-O substitution from Li_2ZrO_3 (ICSD-94893)
$LiNbN_2$	-1.035	R-3m	Li-Na, Nb-Ta substitution from $NaTaN_2$ (ICSD-67347)
$LiNbF_6$	-3.414	R-3	ICSD-165202
$LiTaN_2$	-1.233	R-3m	Li-Na substitution from $NaTaN_2$ (ICSD-67347)
Li_3TaS_4	-1.526	C2/c	S-O substitution from Li_3TaO_4 (ICSD-281301)
$LiTaF_6$	-3.598	R-3	ICSD-165205
Li_2ZnF_4	-2.941	Fd-3m	Zn-Ni substitution from Li_2NiF_4 (ICSD-202859)
Li_2HfF_6	-3.788	P-31m	ICSD-251074
Li_2HfN_2	-1.353	P-3m1	Hf-Zr substitution from Li_2ZrN_2 (ICSD-78790)
LiCeF5	-3.830	$I4_1/a$	ICSD-426211
$LiVN_2$	-1.024	$Pna2_1$	Li-Mg, V-Si substitution from $MgSiN_2$ (ICSD-23501)
$LiMn_2N_3$	-0.496	$Cmc2_1$	Mn-Si substitution from $LiSi_2N_3$ (ICSD-78790)
Li_2MnN_2	-0.663	Pbca	Mn-Si substitution from Li_2SiN_2 (ICSD-420126)

2. Lithiation/delithiation reaction of materials

Table B3. Lithiation and delithiation reactions of typical Al-abiding ternary nitride, oxide, sulfide and fluoride.

a) Li_3AlN_2

Potential ϕ (V) ref. to Li/Li^+	μ_{Li} (eV) ref. to Li metal	Δn_{Li} per formula	Phase equilibria
-0.316	0.316	5.25	Li_9Al_4, Li_3N
/	/	0	Li_3AlN_2
0.789	-0.789	-2.667	AlN, LiN_3
1.668	-1.668	-3	AlN, N_2

b) $LiAlO_2$

Potential ϕ (V) ref. to Li/Li^+	μ_{Li} (eV) ref. to Li metal	Δn_{Li} per formula	Phase equilibria
0.056	-0.056	5.25	Li_9Al_4, Li_2O
0.071	-0.071	2.625	Li_9Al_4, Li_5AlO_4
0.167	-0.167	2.25	Li_3Al_2, Li_5AlO_4
/	/	0	$LiAlO_2$
3.697	-3.697	-0.8	$LiAl_5O_8$, O_2
4.101	-4.101	-1	Al_2O_3, O_2

c) $LiAlS_2$

Potential ϕ (V) ref. to Li/Li^+	μ_{Li} (eV) ref. to Li metal	Δn_{Li} per formula	Phase equilibria
0.071	-0.071	5.25	Li_9Al_4, Li_2S
0.190	-0.190	4.5	Li_3Al_2, Li_2S
0.359	-0.359	4	LiAl, Li_2S
0.963	-0.963	3	Al, Li_2S
0.973	-0.973	1.5	Li_5AlS_4, Al
/	/	0	$LiAlS_2$
2.812	-2.812	-1	Al_2S_3, S

d) Li_3AlF_6

Potential ϕ (V) ref. to Li/Li^+	μ_{Li} (eV) ref. to Li metal	Δn_{Li} per formula	Phase equilibria
0.071	-0.071	5.25	Li_9Al_4, LiF
0.190	-0.190	4.5	Li_3Al_2, LiF
0.359	-0.359	4	LiAl, LiF
1.057	-1.057	3	LiF, Al
/	/	0	Li_3AlF_6
6.477	-6.477	-3	AlF_3, F_2

Table B4. Cathodic limits and lithiation reactions for all binary and ternary fluorides, sulfides, oxides and nitrides plotted in Fig. 4.1. The reaction energy E_D normalized to per Li inserted is for the lithiation of selected compound to from the phase equilibria with Li metal. For materials that are stable against Li metal (i.e., with negative cathodic limit), the "Phase equilibria at Li" column lists the fully lithiated products after lithiation with overpotential.

Compound	Cathodic limit /V ref. to Li/Li^+	Phase equilibria at cathodic limit	Phase equilibria at Li	E_D /eV norm. to Li
ErN	-0.699	Li_3N, Er	Li_3N, Er	0.699
ErF_3	0.371	Er, LiF	LiF, Er	-0.371
Er_2S_3	0.991	$LiErS_2$, ErS	Er, Li_2S	-0.284
$LiErS_2$	0.484	Li_2S, ErS	Er, Li_2S	-0.200
Er_2O_3	-0.239	$LiErO_2$, Er	Er, Li_2O	0.288
$LiErO_2$	-0.304	Er, Li_2O	Er, Li_2O	0.304
TmN	-0.728	Li_3N, Tm	Li_3N, Tm	0.728
TmF_3	0.837	Tm, LiF	LiF, Tm	-0.837
Tm_2S_3	0.660	TmS, Li_2S	Li_2S, Tm	-0.276
Tm_2O_3	-0.238	$LiTmO_2$, Tm	Tm, Li_2O	0.316
$LiTmO_2$	-0.342	Li_2O, Tm	Tm, Li_2O	0.342
HoN	-0.675	Li_3N, Ho	Li_3N, Ho	0.675
HoF_3	0.378	LiF, Ho	LiF, Ho	-0.378
Ho_2S_3	0.997	$LiHoS_2$, HoS	Ho, Li_2S	-0.280
$LiHoS_2$	0.541	Li_2S, HoS	Ho, Li_2S	-0.204
Ho_2O_3	-0.237	$LiHoO_2$, Ho	Ho, Li_2O	0.270
$LiHoO_2$	-0.280	Ho, Li_2O	Ho, Li_2O	0.280
YN	-0.639	Y, Li_3N	Li_3N, Y	0.639
YF_3	0.625	$LiYF_4$, Y	Y, LiF	-0.429

$LiYF_4$	0.364	Y, LiF	LiF, Y	-0.364
Y_2S_3	1.167	Y_5S_7, $LiYS_2$	Y, Li_2S	-0.278
$LiYS_2$	0.600	Li_2S, YS	Y, Li_2S	-0.209
Y_2O_3	-0.204	$LiYO_2$, Y	Y, Li_2O	0.215
$LiYO_2$	-0.219	Y, Li_2O	Y, Li_2O	0.219
LaN	-0.398	Li_3N, La	Li_3N, La	0.398
LaF_3	0.339	La, LiF	LiF, La	-0.339
La_2S_3	0.846	LaS, Li_2S	La, Li_2S	-0.174
La_2O_3	-0.139	La, Li_2O	La, Li_2O	0.139
GdN	-0.559	Li_3N, Gd	Li_3N, Gd	0.559
GdF_3	0.856	LiF, Gd	LiF, Gd	-0.856
Gd_2S_3	0.935	GdS, Li_2S	Li_2S, Gd	-0.281
Gd_2O_3	-0.132	$LiGdO_2$, Gd	Li_2O, Gd	0.149
$LiGdO_2$	-0.154	Gd, Li_2O	Li_2O, Gd	0.154
SmN	-0.500	Li_3N, Sm	Li_3N, Sm	0.500
SmF_3	0.404	LiF, Sm	Sm, LiF	-0.404
Sm_2S_3	0.906	$LiSmS_2$, SmS	Sm, Li_2S	-0.283
$LiSmS_2$	0.858	Li_2S, SmS	Sm, Li_2S	-0.275
Sm_2O_3	-0.126	Sm, Li_2O	Li_2O, Sm	0.126
Ca_3N_2	0.263	Ca_2N, LiCaN	Li_3N, Li_2Ca	0.075
LiCaN	-0.111	Li_3N, Li_2Ca	Li_2Ca, Li_3N	0.111
CaF_2	0.009	LiF, Li_2Ca	Li_2Ca, LiF	-0.009

CaS	-0.061	Li_2Ca, Li_2S	Li_2S, Li_2Ca	0.061
CaO	-0.096	Li_2Ca, Li_2O	Li_2Ca, Li_2O	0.096
NdN	-0.418	Li_3N, Nd	Li_3N, Nd	0.418
NdF_3	0.441	Nd, LiF	LiF, Nd	-0.441
Nd_2S_3	0.900	Li_2S, NdS	Li_2S, Nd	-0.288
Nd_2O_3	-0.059	Nd, Li_2O	Nd, Li_2O	0.059
Be_3N_2	-0.069	LiBeN, Be	Be, Li_3N	0.414
LiBeN	-0.587	Be, Li_3N	Li_3N, Be	0.587
BeF_2	1.119	Li_2BeF_4, Be	Be, LiF	-0.999
Li_2BeF_4	0.879	Be, LiF	Be, LiF	-0.879
BeS	0.943	Li_2S, Be	Be, Li_2S	-0.943
BeO	-0.015	Be, Li_2O	Be, Li_2O	0.015
SrLiN	0.237	$SrLi_4N_2$, Sr_2N	Li_3N, Sr_3Li_2	0.011
$SrLi_4N_2$	-0.054	Sr_3Li_2, Li_3N	Li_3N, Sr_3Li_2	0.054
SrF_2	-0.013	Sr_3Li_2, LiF	Sr_3Li_2, LiF	0.013
SrS	-0.105	Sr_3Li_2, Li_2S	Sr_3Li_2, Li_2S	0.105
SrO	0.013	Li_2O, Sr	Li_2O, Sr_3Li_2	-0.011
Mg_3N_2	0.064	$LiMg_2$, LiMgN	Li_3N, Li_5Mg	0.022
LiMgN	-0.047	Li_3N, Li_5Mg	Li_3N, Li_5Mg	0.047
MgF_2	0.585	Mg, LiF	Li_5Mg, LiF	-0.186
MgS	0.575	Mg, Li_2S	Li_5Mg, Li_2S	-0.184
MgO	0.065	$LiMg_2$, Li_2O	Li_2O, Li_5Mg	-0.030

ScN	-0.689	Li_3ScN_2, Sc	Sc, Li_3N	0.790
Li_3ScN_2	-0.892	Li_3N, Sc	Li_3N, Sc	0.892
ScF_3	0.600	Sc, LiF	Sc, LiF	-0.600
Sc_2S_3	1.252	$LiScS_2$, ScS	Sc, Li_2S	-0.410
$LiScS_2$	0.664	ScS, Li_2S	Sc, Li_2S	-0.312
Sc_2O_3	0.148	$LiScO_2$, Sc	Sc, Li_2O	0.215
$LiScO_2$	-0.336	Sc, Li_2O	Li_2O, Sc	0.336
Hf_3N_4	0.667	HfN, Li_2HfN_2	Li_3N, Hf	0.486
Li_2HfN_2	-0.771	Li_3N, Hf	Li_3N, Hf	0.771
HfF_4	1.481	Li_2HfF_6, Hf	LiF, Hf	-1.173
Li_2HfF_6	1.019	Hf, LiF	LiF, Hf	-1.019
HfS_2	0.942	Li_2S, Hf_2S	Hf, Li_2S	-0.821
HfO_2	0.457	Hf, Li_2HfO_3	Hf, Li_2O	-0.077
$Li_6Hf_2O_7$	-0.153	Li_2O, Hf	Li_2O, Hf	0.153
Li_2HfO_3	0.122	$Li_6Hf_2O_7$, Hf	Li_2O, Hf	0.113
Zr_3N_4	0.956	Li_2ZrN_2, ZrN	Li_3N, Zr	0.374
Li_2ZrN_2	-0.603	Zr_2N, Li_3N	Zr, Li_3N	0.651
ZrF_4	1.619	$Li_3Zr_4F_{19}$, Zr	LiF, Zr	-1.331
Li_4ZrF_8	1.209	LiF, Zr	LiF, Zr	-1.209
Li_2ZrF_6	1.239	Li_4ZrF_8, Zr	LiF, Zr	-1.216
$Li_3Zr_4F_{19}$	1.510	Li_2ZrF_6, Zr	Zr, LiF	-1.277
ZrS_2	1.705	$Li(ZrS_2)_2$	Li_2S, Zr	-0.870

Li_2ZrS_3	1.227	$Li(ZrS_2)_2$, Li_2S	Zr, Li_2S	-0.810
ZrO_2	0.583	Li_2ZrO_3, Zr_3O	Zr, Li_2O	-0.232
$Li_6Zr_2O_7$	0.048	Li_2O, Zr_3O	Zr, Li_2O	-0.041
Li_2ZrO_3	0.339	$Li_6Zr_2O_7$, Zr_3O	Zr, Li_2O	-0.079
NaF	0.445	LiF, Na	Na, LiF	-0.445
Na_2S	0.417	Na, NaLiS	Na, Li_2S	-0.399
NaLiS	0.381	Na, Li_2S	Na, Li_2S	-0.381
Na_2O	0.925	Li_2O, Na	Na, Li_2O	-0.925
KF	0.449	LiF, K	LiF, K	-0.449
K_2S	0.488	KLiS, K	K, Li_2S	-0.410
KLiS	0.333	Li_2S, K	Li_2S, K	-0.333
K_2O	1.209	Li_2O, K	K, Li_2O	-1.209
Li_2CeN_2	-0.451	CeN, Li_3N	Ce, Li_3N	0.495
CeF_4	3.228	$LiCeF_5$, CeF_3	Ce, LiF	-1.257
$LiCeF_5$	3.158	CeF_3, LiF	Ce, LiF	-1.248
CeS_2	1.955	Ce_2S_3, Li_2S	Li_2S, Ce	-0.734
CeO_2	1.225	$Ce_{11}O_{20}$, Li_2CeO_3	Li_2O, Ce	-0.147
Li_2CeO_3	1.174	$Ce_{11}O_{20}$, Li_2O	Ce, Li_2O	-0.144
AlN	-0.004	Li_3AlN_2, Li_9Al_4	Li_3N, Li_9Al_4	0.160
Li_3AlN_2	-0.316	Li_3N, Li_9Al_4	Li_3N, Li_9Al_4	0.316
AlF_3	1.289	Li_3AlF_6, Al	Li_9Al_4, LiF	-0.767
Li_3AlF_6	1.057	Al, LiF	Li_9Al_4, LiF	-0.701

Al_2S_3	1.597	Al, $LiAlS_2$	Li_9Al_4, Li_2S	-0.740
$LiAlS_2$	0.973	Li_5AlS_4, Al	Li_9Al_4, Li_2S	-0.650
Li_5AlS_4	0.963	Al, Li_2S	Li_9Al_4, Li_2S	-0.647
Al_2O_3	1.233	$LiAl_5O_8$, Al	Li_9Al_4, Li_2O	-0.233
$LiAlO_2$	0.167	Li_5AlO_4, Li_3Al_2	Li_9Al_4, Li_2O	-0.105
Li_5AlO_4	0.056	Li_2O, Li_9Al_4	Li_9Al_4, Li_2O	-0.056
$LiAl_5O_8$	0.802	$LiAlO_2$, Al	Li_9Al_4, Li_2O	-0.195
Si_3N_4	1.127	$LiSi_2N_3$, Si	$Li_{21}Si_5$, Li_3N	-0.067
$LiSi_2N_3$	0.245	Li_2SiN_2, $Li_{13}Si_4$	Li_3N, $Li_{21}Si_5$	0.011
Li_2SiN_2	0.022	Li_5SiN_3, $Li_{21}Si_5$	Li_3N, $Li_{21}Si_5$	0.091
Li_5SiN_3	-0.148	Li_3N, $Li_{21}Si_5$	Li_3N, $Li_{21}Si_5$	0.148
SiF_4	2.298	Si, Li_2SiF_6	$Li_{21}Si_5$, LiF	-1.112
Li_2SiF_6	1.839	Si, LiF	LiF, $Li_{21}Si_5$	-1.038
SiS_2	1.633	Li_2SiS_3, Si	$Li_{21}Si_5$, Li_2S	-0.872
Li_2SiS_3	1.455	Li_8SiS_6, Si	$Li_{21}Si_5$, Li_2S	-0.840
Li_8SiS_6	1.411	Si, Li_2S	$Li_{21}Si_5$, Li_2S	-0.829
SiO_2	1.320	$Li_2Si_2O_5$, Si	$Li_{21}Si_5$, Li_2O	-0.454
Li_2SiO_3	0.761	Li_4SiO_4, Si	$Li_{21}Si_5$, Li_2O	-0.295
$Li_2Si_2O_5$	1.265	Li_2SiO_3, Si	$Li_{21}Si_5$, Li_2O	-0.372
Li_4SiO_4	0.258	$Li_{13}Si_4$, Li_8SiO_6	$Li_{21}Si_5$, Li_2O	-0.222
Li_8SiO_6	0.227	$Li_{13}Si_4$, Li_2O	Li_2O, $Li_{21}Si_5$	-0.213
Zn_3N_2	1.423	Zn, LiN_3	LiZn, Li_3N	-0.532

$LiZnN$	0.380	Li_3N, $LiZn_3$	$LiZn$, Li_3N	-0.365
ZnF_2	2.441	Zn, Li_2ZnF_4	$LiZn$, LiF	-1.764
Li_2ZnF_4	2.428	Zn, LiF	$LiZn$, LiF	-1.760
ZnS	1.200	Zn, Li_2S	$LiZn$, Li_2S	-0.941
ZnO	1.364	$Li_{10}Zn_4O_9$, Zn	Li_2O, $LiZn$	-1.014
Li_6ZnO_4	1.179	Li_2O, Zn	$LiZn$, Li_2O	-0.927
$Li_{10}Zn_4O_9$	1.318	Li_6ZnO_4, Zn	$LiZn$, Li_2O	-0.968
InN	1.037	LiN_3, In	Li_3N, $Li_{13}In_3$	-0.376
InF_3	2.625	In, $LiInF_4$	LiF, $Li_{13}In_3$	-1.195
$LiInF_4$	2.517	LiF, In	LiF, $Li_{13}In_3$	-1.184
In_2S_3	1.634	InS, Li_2S	$Li_{13}In_3$, Li_2S	-0.785
In_2O_3	1.579	$LiInO_2$, In	$Li_{13}In_3$, Li_2O	-0.734
$LiInO_2$	1.363	In, Li_2O	$Li_{13}In_3$, Li_2O	-0.712
EuN	-0.051	Li_3N, Eu	Li_3N, Eu	0.051
EuF_3	3.389	EuF_2, LiF	Eu, LiF	-1.278
Eu_2O_3	1.655	EuO, Li_2O	Li_2O, Eu	-0.531
Ta_3N_5	1.371	$Li_2Ta_3N_5$	Ta, Li_3N	0.073
Li_4TaN_3	-0.016	Li_7TaN_4, Ta	Li_3N, Ta	0.583
Li_7TaN_4	-0.771	Li_3N, Ta	Li_3N, Ta	0.771
$LiTaN_2$	0.877	$Li_2Ta_3N_5$, Li_4TaN_3	Li_3N, Ta	0.250
TaF_5	2.895	Ta, $LiTaF_6$	LiF, Ta	-2.045
$LiTaF_6$	1.876	LiF, Ta	LiF, Ta	-1.876

Li_3TaS_4	1.853	Li_2S, $Li_2(TaS_2)_3$	Li_2S, Ta	-1.302
Ta_2O_5	1.694	$LiTa_3O_8$, Ta	Li_2O, Ta	-0.758
$LiTaO_3$	1.175	Li_3TaO_4, Ta	Li_2O, Ta	-0.583
Li_3TaO_4	0.543	Li_5TaO_5, Ta	Ta, Li_2O	-0.386
$LiTa_3O_8$	1.591	$LiTaO_3$, Ta	Ta, Li_2O	-0.695
Li_5TaO_5	0.347	Ta, Li_2O	Li_2O, Ta	-0.347
Li_5TiN_3	-0.828	Li_3N, Ti_2N	Li_3N, Ti	0.829
Li_2TiN_2	0.712	TiN, Li_5TiN_3	Li_3N, Ti	0.572
TiF_4	2.928	TiF_3, Li_2TiF_6	Ti, LiF	-1.725
Li_2TiF_6	1.896	TiF_3, LiF	Ti, LiF	-1.553
TiS_2	1.939	$Li(TiS_2)_3$	Ti, Li_2S	-1.050
Li_2TiS_3	1.717	Li_2S, $LiTiS_2$	Ti, Li_2S	-1.009
TiO_2	1.712	$LiTi_2O_4$	Ti, Li_2O	-0.468
Li_2TiO_3	0.500	$LiTiO_2$, Li_4TiO_4	Ti, Li_2O	-0.167
Li_4TiO_4	0.123	Ti_3O, Li_2O	Ti, Li_2O	-0.095
$Li_4Ti_5O_{12}$	1.749	$Li_7Ti_{11}O_{24}$, Li_2TiO_3	Ti, Li_2O	-0.347
Li_2SnN_2	0.473	Li_3N, $Li_{13}Sn_5$	$Li_{17}Sn_4$, Li_3N	-0.424
SnF_4	4.319	SnF_3, Li_2SnF_6	LiF, $Li_{17}Sn_4$	-1.651
Li_2SnF_6	2.911	SnF_2, LiF	LiF, $Li_{17}Sn_4$	-1.528
SnS_2	1.945	Li_2SnS_3, SnS	Li_2S, $Li_{17}Sn_4$	-1.058
Li_2SnS_3	1.822	SnS, Li_2S	$Li_{17}Sn_4$, Li_2S	-1.043

SnO_2	1.986	Li_2SnO_3, Sn_5O_6	$Li_{17}Sn_4$, Li_2O	-0.955
Li_8SnO_6	1.243	Li_2O, Sn	$Li_{17}Sn_4$, Li_2O	-0.824
Li_2SnO_3	1.362	Li_8SnO_6, Sn	$Li_{17}Sn_4$, Li_2O	-0.853
BN	0.062	Li_3BN_2, LiB	Li_3N, LiB	0.195
Li_3BN_2	-0.453	Li_3N, LiB	LiB, Li_3N	0.453
BF_3	2.933	B, $LiBF_4$	LiF, LiB	-1.720
$LiBF_4$	1.937	B, LiF	LiB, LiF	-1.534
B_2S_3	1.870	B, $Li_5B_7S_{13}$	Li_2S, LiB	-1.319
Li_3BS_3	1.589	B, Li_2S	LiB, Li_2S	-1.272
$Li_5B_7S_{13}$	1.615	Li_3BS_3, B	Li_2S, LiB	-1.280
B_2O_3	2.067	B_6O, $Li_3B_7O_{12}$	LiB, Li_2O	-0.652
Li_3BO_3	0.284	$Li_7B_{18}O$, Li_2O	Li_2O, LiB	-0.249
$Li_2B_4O_7$	1.291	$LiBO_2$, B_6O	Li_2O, LiB	-0.508
$Li_3B_7O_{12}$	1.294	$Li_2B_4O_7$, B_6O	LiB, Li_2O	-0.519
$LiBO_2$	1.014	B_6O, Li_3BO_3	Li_2O, LiB	-0.436
GaN	0.484	Li_3GaN_2, LiGa	Li_2Ga, Li_3N	-0.281
Li_3GaN_2	0.125	Li_3N, Li_2Ga	Li_2Ga, Li_3N	-0.125
GaF_3	2.581	Li_3GaF_6, Ga	Li_2Ga, LiF	-1.637
Li_3GaF_6	2.277	Ga, LiF	Li_2Ga, LiF	-1.546

Ga_2S_3	2.099	$LiGaS_2$, GaS	Li_2Ga, Li_2S	-1.053
$LiGaS_2$	1.307	Ga, Li_2S	Li_2Ga, Li_2S	-0.964
Ga_2O_3	2.131	$LiGa_5O_8$, Ga	Li_2Ga, Li_2O	-0.902
$LiGaO_2$	1.046	Li_5GaO_4, Ga	Li_2Ga, Li_2O	-0.752
$LiGa_5O_8$	1.892	Ga, $LiGaO_2$	Li_2Ga, Li_2O	-0.865
Li_5GaO_4	0.862	Ga, Li_2O	Li_2Ga, Li_2O	-0.697
NiF_2	3.200	Ni, Li_2NiF_4	Ni, LiF	-3.165
Li_2NiF_4	3.130	Ni, LiF	Ni, LiF	-3.130
NiO	2.172	Li_2O, Ni	Li_2O, Ni	-2.172
Li_7NbN_4	-0.639	Li_3N, Nb	Nb, Li_3N	0.639
$LiNbN_2$	0.787	NbN, Li_7NbN_4	Li_3N, Nb	0.092
NbF_5	3.169	Nb_2F_5, $LiNbF_6$	Nb, LiF	-2.309
$LiNbF_6$	2.204	Nb_2F_5, LiF	Nb, LiF	-2.171
Li_3NbS_4	2.083	Li_2S, $Li_5(NbS_2)_7$	Nb, Li_2S	-1.378
Nb_2O_5	2.286	$LiNb_3O_8$, $Nb_{12}O_{29}$	Li_2O, Nb	-0.970
$LiNbO_3$	1.745	Li_3NbO_4, $LiNbO_2$	Li_2O, Nb	-0.814
$LiNb_3O_8$	2.225	$Nb_{12}O_{29}$, $LiNbO_3$	Nb, Li_2O	-0.917
$Li_8Nb_2O_9$	0.623	$LiNbO_2$, Li_2O	Nb, Li_2O	-0.577
Li_3NbO_4	0.937	$Li_8Nb_2O_9$, $LiNbO_2$	Nb, Li_2O	-0.603
FeN	0.630	Fe_3N, Li_3FeN_2	Li_3N, Fe	-0.405
Li_3FeN_2	0.188	Li_3N, Fe	Fe, Li_3N	-0.188
FeF_3	3.655	$LiFe_2F_6$	Fe, LiF	-2.663

Li_3FeF_6	3.151	FeF_2, LiF	Fe, LiF	-2.553
Fe_2O_3	2.299	Fe_3O_4, $LiFeO_2$	Fe, Li_2O	-1.535
Li_5FeO_4	1.282	Li_2O, Fe	Fe, Li_2O	-1.282
$LiFeO_2$	1.540	Li_2FeO_2	Fe, Li_2O	-1.373
Ge_3N_4	1.728	$LiGe_2N_3$, Ge	Li_3N, $Li_{15}Ge_4$	-0.438
Li_5GeN_3	0.198	$Li_{15}Ge_4$, Li_3N	$Li_{15}Ge_4$, Li_3N	-0.198
$LiGe_2N_3$	0.735	Li_2GeN_2, Ge	Li_3N, $Li_{15}Ge_4$	-0.356
Li_2GeN_2	0.500	Li_5GeN_3, LiGe	$Li_{15}Ge_4$, Li_3N	-0.282
GeF_4	3.773	Ge_5F_{12}, Li_2GeF_6	LiF, $Li_{15}Ge_4$	-1.735
Li_2GeF_6	2.710	LiF, Ge	$Li_{15}Ge_4$, LiF	-1.598
GeS_2	1.913	GeS, Li_2GeS_3	Li_2S, $Li_{15}Ge_4$	-1.107
Li_4GeS_4	1.622	Li_2S, Ge	Li_2S, $Li_{15}Ge_4$	-1.037
Li_2GeS_3	1.865	Li_4GeS_4, Ge	$Li_{15}Ge_4$, Li_2S	-1.068
GeO_2	2.408	$Li_2Ge_7O_{15}$, Ge	$Li_{15}Ge_4$, Li_2O	-0.992
Li_4GeO_4	1.016	Ge, Li_2O	Li_2O, $Li_{15}Ge_4$	-0.724

$Li_2Ge_7O_{15}$	2.275	$Li_4Ge_5O_{12}$, Ge	Li_2O, $Li_{15}Ge_4$	-0.960
$Li_4Ge_5O_{12}$	2.259	Li_2GeO_3, Ge	Li_2O, $Li_{15}Ge_4$	-0.911
Li_2GeO_3	1.579	Ge, Li_4GeO_4	Li_2O, $Li_{15}Ge_4$	-0.797
CuF_2	3.638	LiF, Cu	$LiCu_3$, LiF	-3.136
CuS	1.821	Cu_7S_4, Li_2S	$LiCu_3$, Li_2S	-1.569
CuO	2.411	LiCuO	$LiCu_3$, Li_2O	-1.863
WN_2	2.056	$Li_5W_7N_{12}$, N_2	Li_3N, W	-0.353
Li_6WN_4	-0.465	Li_3N, W	Li_3N, W	0.465
WF_6	3.593	$LiWF_6$	W, LiF	-3.067
WO_3	2.564	Li_2WO_4, $W_{18}O_{49}$	W, Li_2O	-1.650
Li_2WO_4	2.097	Li_4WO_5, W	Li_2O, W	-1.394
Li_4WO_5	1.219	W, Li_2O	W, Li_2O	-1.219
YbS_2	2.154	YbS, LiS_4	Yb, Li_2S	-0.947
YbO_2	2.853	YbO, Li_2O	Yb, Li_2O	-1.155
P_3N_5	2.286	$LiPN_2$, P	Li_3P, Li_3N	-0.552
$LiPN_2$	0.610	Li_7PN_4, Li_3P	Li_3P, Li_3N	-0.307
Li_7PN_4	0.005	Li_3P, Li_3N	Li_3P, Li_3N	-0.005
PF_5	3.302	P, $LiPF_6$	Li_3P, LiF	-2.118
$LiPF_6$	2.735	P, LiF	Li_3P, LiF	-2.059

P_2S_5	2.273	Li_3PS_4, P_4S_9	Li_3P, Li_2S	-1.532
Li_3PS_4	1.719	P, Li_2S	Li_3P, Li_2S	-1.423
P_2O_5	3.274	$LiPO_3$, P	Li_3P, Li_2O	-1.215
$Li_4P_2O_7$	2.307	Li_3PO_4, P	Li_3P, Li_2O	-0.826
Li_3PO_4	0.688	Li_2O, Li_3P	Li_3P, Li_2O	-0.688
$LiPO_3$	2.479	P, $Li_4P_2O_7$	Li_3P, Li_2O	-0.979
Li_6MoN_4	-0.362	Li_3N, Mo	Li_3N, Mo	0.362
MoF_6	4.335	Li_2MoF_6	LiF, Mo	-3.257
MoO_3	3.350	Mo_8O_{23}, Li_2MoO_4	Mo, Li_2O	-1.757
Li_2MoO_4	1.842	Li_2MoO_3, Li_4MoO_5	Li_2O, Mo	-1.420
Li_4MoO_5	1.333	Mo, Li_2O	Mo, Li_2O	-1.333
Li_7VN_4	-0.718	Li_3N, V	Li_3N, V	0.718
$LiVN_2$	0.841	VN, Li_7VN_4	Li_3N, V	0.083
VF_5	5.104	VF_4, $LiVF_6$	V, LiF	-2.968
$LiVF_6$	4.570	Li_2VF_6	V, LiF	-2.849
Li_3VS_4	1.795	V_3S_4, Li_2S	V, Li_2S	-1.433
V_2O_5	3.675	$LiVO_3$, V_3O_7	V, Li_2O	-1.493
Li_3VO_4	1.126	Li_2O, $LiVO_2$	Li_2O, V	-0.947
$LiVO_3$	3.229	LiV_2O_5, Li_3VO_4	V, Li_2O	-1.287
Li_2MnN_2	0.552	Li_7MnN_4, Mn_2N	Li_3N, Mn	-0.092
MnF_4	6.030	MnF_3, Li_2MnF_6	LiF, Mn	-3.353
Li_2MnF_6	4.557	LiF, Li_2MnF_5	LiF, Mn	-3.065

MnS_2	1.830	$Li(MnS_2)_2$	Mn, Li_2S	-1.598
MnO_2	3.711	Mn_2O_3, $Li_5Mn_7O_{16}$	Li_2O, Mn	-1.748
Li_2MnO_3	1.732	Li_2O, $LiMnO_2$	Mn, Li_2O	-1.381
$Li_4Mn_5O_{12}$	3.417	$Li_5Mn_7O_{16}$, Li_2MnO_3	Mn, Li_2O	-1.565
CoF_4	6.635	$LiCoF_4$	LiF, Co	-4.150
CoS_2	1.984	Co_3S_4, Li_2S	Co, Li_2S	-1.750
CoO_2	4.096	$Li(CoO_2)_2$	Co, Li_2O	-2.253
Li_8CoO_6	2.605	Li_5CoO_4, Li_2O	Co, Li_2O	-1.943

3. Comparison between DFT calculated and experimental values

To evaluate the error of the DFT calculation results, we compared the formation enthalpy of binary nitrides and the potential (referenced to Li/Li^+) of lithium conversion reaction of binary nitrides based on the following reaction

$$M_xN_y + 3y\ Li \rightarrow y\ Li_3N + x\ M.$$

These results are summarized and compared in Table S5. We found that the calculated conversion reaction potential is general in agreement with the experimental value with an error of less than 0.1 V.

Table B5. Experimental and calculated formation enthalpy and conversion reaction potential of binary nitrides.

	$\Delta H_{exp.}$ * (eV/atom)	$\Delta H_{cal.}$ (eV/atom)	$\phi_{exp.}$ (V)	$\phi_{cal.}$ (V)
Li_3N	-0.428	-0.460	-	-
TaN	-1.309	-1.366	-0.303	-0.297
Ca_3N_2	-0.912	-0.946	-0.190	-0.175
GaN	-0.569	-0.666	0.191	0.169
VN	-1.131	-1.164	-0.184	-0.162
NbN	-1.227	-1.252	-0.248	-0.221
Be_3N_2	-1.224	-1.233	-0.450	-0.414
HfN	-1.939	-1.940	-0.722	-0.680
Cr_2N	-0.434	-0.523	0.136	0.091
CeN	-1.694	-1.684	-0.559	-0.509
Ta_2N	-0.942	-0.934	-0.372	-0.321
Zn_3N_2	-0.047	-0.033	0.531	0.586
TiN	-1.754	-1.906	-0.600	-0.657
UN	-1.529	-1.501	-0.449	-0.387
BN	-1.309	-1.472	-0.303	-0.368
LaN	-1.553	-1.517	-0.465	-0.398
ZrN	-1.911	-1.870	-0.704	-0.633
Si_3N_4	-1.104	-1.312	-0.074	-0.152
AlN	-1.652	-1.595	-0.531	-0.450

Mg_3N_2	-0.958	-0.909	-0.228	-0.144
CrN	-0.608	-0.527	0.165	0.262
Th_3N_4	-1.935	-1.829	-0.559	-0.453
PuN	-1.553	-1.438	-0.465	-0.345
EuN	-1.129	-0.996	-0.183	-0.051
YN	-1.553	-1.879	-0.465	-0.639
ThN	-1.965	-1.761	-0.740	-0.561
ScN	-1.628	-2.106	-0.515	-0.790
InN	-0.717	-0.105	0.092	0.543

* Chase, M. W. NIST-JANAF thermochemical tables 4th ed.; National Institute of Standards and Technology: Gaithersburg, 1998.

4. Li-M-O-N grand potential phase diagrams

Figure B1. Grand potential phase diagrams in equilibrium with Li metal. The composition ranges that form passivating interphase and that form non-passivating interphase are colored green and red, respectively.

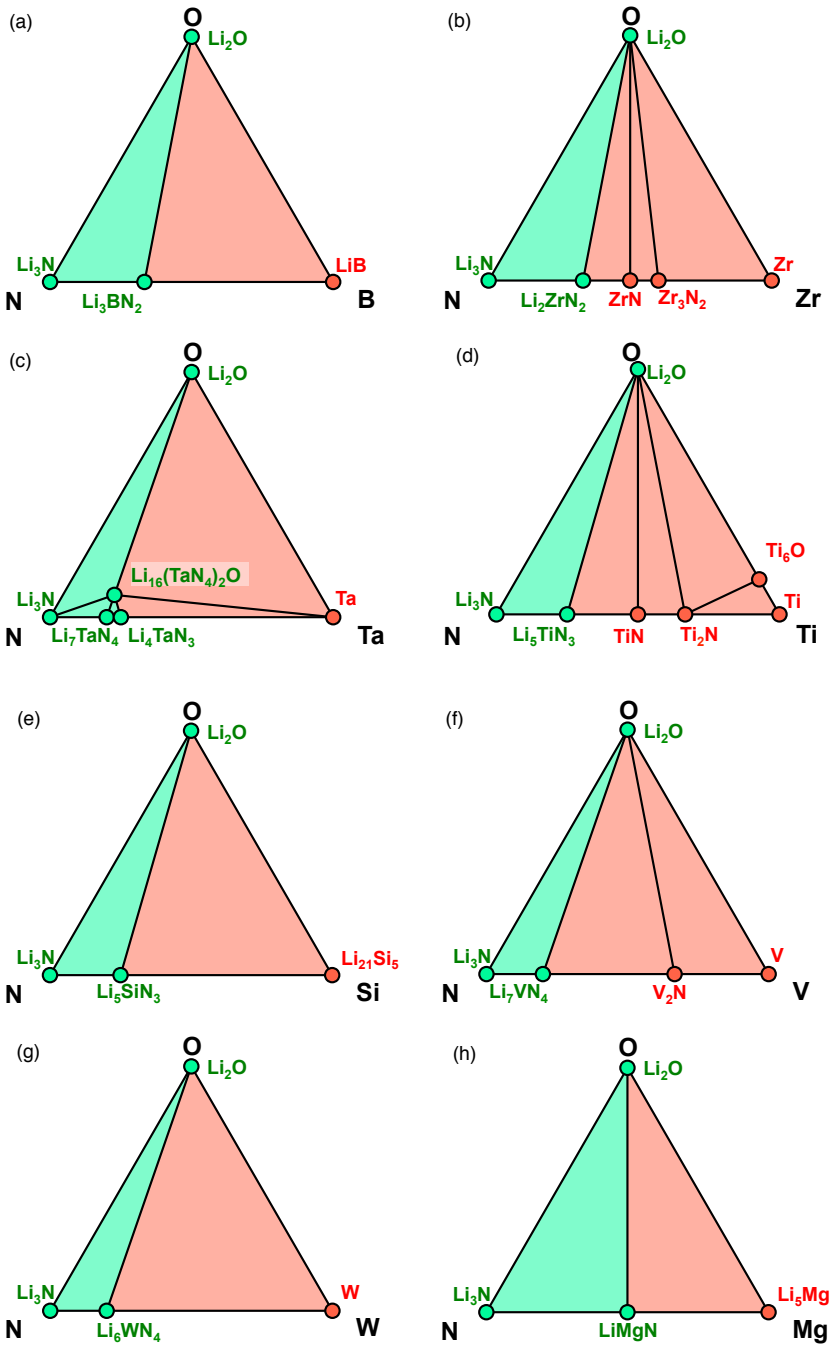

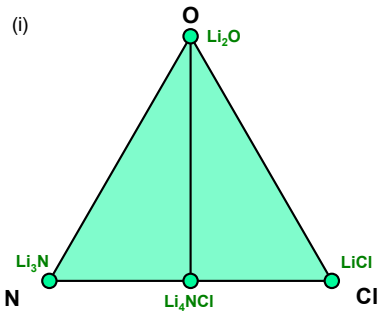
(i)
O
Li2O
Li3N
LiCl
N
Li4NCl
Cl

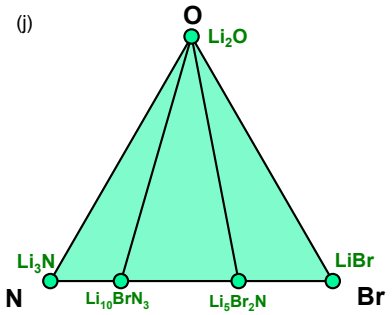
(j)
O
Li2O
Li3N
LiBr
N
Li10BrN3
Li5Br2N
Br

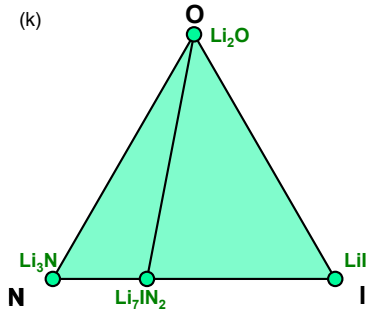
(k)
O
Li2O
Li3N
LiI
N
Li7IN2
I

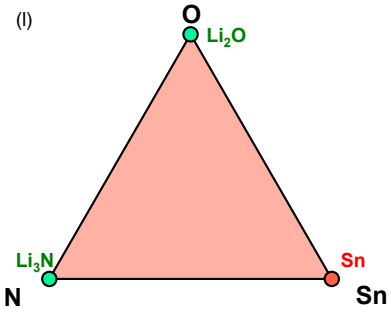
(l)
O
Li2O
Li3N
Sn
N
Sn

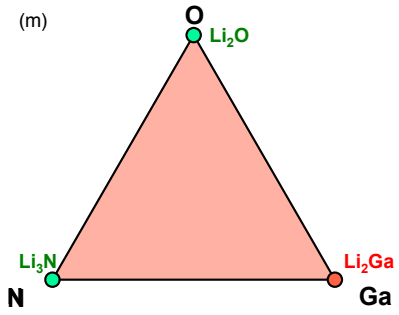
(m)
O
Li2O
Li3N
Li2Ga
N
Ga

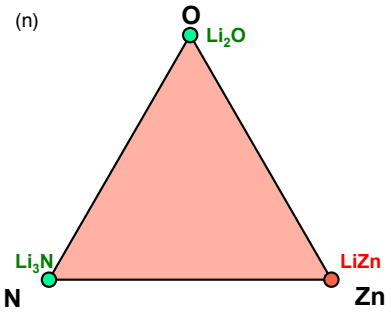
(n)
O
Li2O
Li3N
LiZn
N
Zn

Appendix C

1. Lattice parameters based on the classic interatomic potential

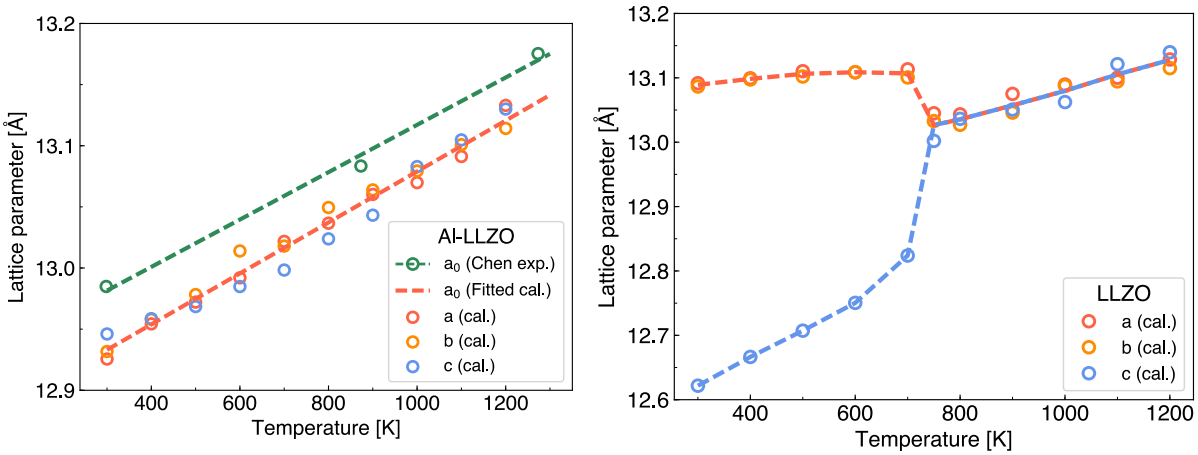

Figure C1. The calculated equilibrium lattice parameters based on the classic interatomic potential in this work. a) Al-doped LLZO ($Li_{6.25}Al_{0.25}La_3Zr_2O_{12}$), with experimental lattice parameter for comparison[21] b) undoped LLZO ($Li_7La_3Zr_2O_{12}$), which shows tetragonal-cubic phase change at approximated 750 K.

Bibliography

(1) Kamaya, N.; Homma, K.; Yamakawa, Y.; Hirayama, M.; Kanno, R.; Yonemura, M.; Kamiyama, T.; Kato, Y.; Hama, S.; Kawamoto, K.et al. A lithium superionic conductor. *Nat. Mater.* **2011,** *10* (9), 682.

(2) Takada, K. Progress and prospective of solid-state lithium batteries. *Acta Mater.* **2013,** *61* (3), 759.

(3) Seino, Y.; Ota, T.; Takada, K.; Hayashi, A.; Tatsumisago, M. A sulphide lithium super ion conductor is superior to liquid ion conductors for use in rechargeable batteries. *Energy Environ. Sci.* **2014,** *7* (2), 627.

(4) Yamane, H.; Shibata, M.; Shimane, Y.; Junke, T.; Seino, Y.; Adams, S.; Minami, K.; Hayashi, A.; Tatsumisago, M. Crystal structure of a superionic conductor, Li7P3S11. *Solid State Ionics* **2007,** *178* (15–18), 1163.

(5) Thangadurai, V.; Pinzaru, D.; Narayanan, S.; Baral, A. K. Fast Solid-State Li Ion Conducting Garnet-Type Structure Metal Oxides for Energy Storage. *J. Phys. Chem. Lett.* **2015,** *6* (2), 292.

(6) Murugan, R.; Thangadurai, V.; Weppner, W. Fast lithium ion conduction in garnet-type Li(7)La(3)Zr(2)O(12). *Angew. Chem. Int. Ed. Engl.* **2007,** *46* (41), 7778.

(7) Li, J.; Baggetto, L.; Martha, S. K.; Veith, G. M.; Nanda, J.; Liang, C.; Dudney, N. J. An Artificial Solid Electrolyte Interphase Enables the Use of a LiNi0.5Mn1.5O4 5 V Cathode with Conventional Electrolytes. *Adv. Energy Mater.* **2013,** *3* (10), 1275.

(8) Li, J.; Ma, C.; Chi, M.; Liang, C.; Dudney, N. J. Solid Electrolyte: the Key for High-Voltage Lithium Batteries. *Adv. Energy Mater.* **2015,** *5* (4), 1401408.

(9) Liu, Z.; Fu, W.; Payzant, E. A.; Yu, X.; Wu, Z.; Dudney, N. J.; Kiggans, J.; Hong, K.; Rondinone, A. J.; Liang, C. Anomalous high ionic conductivity of nanoporous beta-Li3PS4. *J. Am. Chem. Soc.* **2013,** *135* (3), 975.

(10) Park Kern, H.; Bai, Q.; Kim Dong, H.; Oh Dae, Y.; Zhu, Y.; Mo, Y.; Jung Yoon, S. Design Strategies, Practical Considerations, and New Solution Processes of Sulfide Solid Electrolytes for All-Solid-State Batteries. *Advanced Energy Materials* **2018,** *0* (0), 1800035.

(11) Thangadurai, V.; Weppner, W. Li6ALa2Ta2O12 (A = Sr, Ba): Novel Garnet-Like Oxides for Fast Lithium Ion Conduction. *Adv. Funct. Mater.* **2005,** *15* (1), 107.

(12) Yu, X.; Bates, J. B.; Jellison, G. E.; Hart, F. X. A Stable Thin-Film Lithium Electrolyte: Lithium Phosphorus Oxynitride. *J. Electrochem. Soc.* **1997,** *144* (2), 524.

(13) Mo, Y.; Ong, S. P.; Ceder, G. First Principles Study of the Li10GeP2S12 Lithium Super Ionic Conductor Material. *Chem. Mater.* **2012,** *24* (1), 15.

(14) Han, F.; Gao, T.; Zhu, Y.; Gaskell, K. J.; Wang, C. A Battery Made from a Single Material. *Adv. Mater.* **2015,** *27* (23), 3473.

(15) Zhu, Y.; He, X.; Mo, Y. Origin of Outstanding Stability in the Lithium Solid Electrolyte Materials: Insights from Thermodynamic Analyses Based on First Principles Calculations. *ACS Appl. Mater. Interfaces* **2015,** *7* (42), 23685.

(16) Han, F.; Zhu, Y.; He, X.; Mo, Y.; Wang, C. Electrochemical Stability of Li10GeP2S12 and Li7La3Zr2O12 Solid Electrolytes. *Adv. Energy Mater.* **2016,** *6* (8), 1501590.

(17) Hartmann, P.; Leichtweiss, T.; Busche, M. R.; Schneider, M.; Reich, M.; Sann, J.; Adelhelm, P.; Janek, J. Degradation of NASICON-Type Materials in Contact with Lithium Metal: Formation of Mixed Conducting Interphases (MCI) on Solid Electrolytes. *J. Phys. Chem. C* **2013,** *117* (41), 21064.

(18) Wenzel, S.; Leichtweiss, T.; Krüger, D.; Sann, J.; Janek, J. Interphase formation on lithium solid electrolytes—An in situ approach to study interfacial reactions by photoelectron spectroscopy. *Solid State Ionics* **2015,** *278*, 98.

(19) Wenzel, S.; Randau, S.; Leichtweiß, T.; Weber, D. A.; Sann, J.; Zeier, W. G.; Janek, J. r. Direct observation of the interfacial instability of the fast ionic conductor Li10GeP2S12 at the lithium metal anode. *Chem. Mater.* **2016,** *28* (7), 2400.

(20) Stramare, S.; Thangadurai, V.; Weppner, W. Lithium lanthanum titanates: a review. *Chem. Mater.* **2003,** *15* (21), 3974.

(21) Chen, Y.; Rangasamy, E.; Liang, C.; An, K. Origin of high Li+ conduction in doped Li7La3Zr2O12 garnets. *Chemistry of Materials* **2015,** *27* (16), 5491.

(22) He, X.; Zhu, Y.; Mo, Y. Origin of fast ion diffusion in super-ionic conductors. *Nature Communications* **2017,** *8*.

(23) Bernstein, N.; Johannes, M. D.; Hoang, K. Origin of the structural phase transition in Li 7 La 3 Zr 2 O 12. *Physical review letters* **2012,** *109* (20), 205702.

(24) Miara, L. J.; Ong, S. P.; Mo, Y.; Richards, W. D.; Park, Y.; Lee, J.-M.; Lee, H. S.; Ceder, G. Effect of Rb and Ta Doping on the Ionic Conductivity and Stability of the Garnet Li7+ 2 x–y (La3–x Rb x)(Zr2–y Ta y) O12 (0≤ x≤ 0.375, 0≤ y≤ 1) Superionic Conductor: A First Principles Investigation. *Chemistry of Materials* **2013,** *25* (15), 3048.

(25) Kozinsky, B.; Akhade, S. A.; Hirel, P.; Hashibon, A.; Elsässer, C.; Mehta, P.; Logeat, A.; Eisele, U. Effects of sublattice symmetry and frustration on ionic transport in garnet solid electrolytes. *Physical review letters* **2016,** *116* (5), 055901.

(26) Thangadurai, V.; Narayanan, S.; Pinzaru, D. Garnet-type solid-state fast Li ion conductors for Li batteries: critical review. *Chemical Society Reviews* **2014,** *43* (13), 4714.

(27) Ma, C.; Chen, K.; Liang, C.; Nan, C.-W.; Ishikawa, R.; More, K.; Chi, M. Atomic-scale origin of the large grain-boundary resistance in perovskite Li-ion-conducting solid electrolytes. *Energy & Environmental Science* **2014,** *7* (5), 1638.

(28) Cheng, E. J.; Sharafi, A.; Sakamoto, J. Intergranular Li metal propagation through polycrystalline Li 6.25 Al 0.25 La 3 Zr 2 O 12 ceramic electrolyte. *Electrochimica Acta* **2017,** *223*, 85.

(29) Porz, L.; Swamy, T.; Sheldon, B. W.; Rettenwander, D.; Frömling, T.; Thaman, H. L.; Berendts, S.; Uecker, R.; Carter, W. C.; Chiang, Y. M. Mechanism of lithium metal penetration through inorganic solid electrolytes. *Advanced Energy Materials* **2017,** *7* (20).

(30) Bower, A. F.; Guduru, P. R.; Sethuraman, V. A. A finite strain model of stress, diffusion, plastic flow, and electrochemical reactions in a lithium-ion half-cell. *Journal of the Mechanics and Physics of Solids* **2011,** *59* (4), 804.

(31) Schichtel, N.; Korte, C.; Hesse, D.; Janek, J. Elastic strain at interfaces and its influence on ionic conductivity in nanoscaled solid electrolyte thin films—theoretical considerations and experimental studies. *Physical Chemistry Chemical Physics* **2009,** *11* (17), 3043.

(32) Ong, S. P.; Wang, L.; Kang, B.; Ceder, G. Li−Fe−P−O2 Phase Diagram from First Principles Calculations. *Chem. Mater.* **2008,** *20* (5), 1798.

(33) Miara, L. J.; Richards, W. D.; Wang, Y. E.; Ceder, G. First-Principles Studies on Cation Dopants and Electrolyte|Cathode Interphases for Lithium Garnets. *Chem. Mater.* **2015,** *27* (11), 4040.

(34) Jain, A.; Ong, S. P.; Hautier, G.; Chen, W.; Richards, W. D.; Dacek, S.; Cholia, S.; Gunter, D.; Skinner, D.; Ceder, G.et al. Commentary: The Materials Project: A materials genome approach to accelerating materials innovation. *APL Materials* **2013,** *1* (1), 011002.

(35) Perdew, J. P.; Ernzerhof, M.; Burke, K. Rationale for mixing exact exchange with density functional approximations. *J. Chem. Phys.* **1996,** *105* (22), 9982.

(36) Blöchl, P. E. Projector augmented-wave method. *Physical Review B* **1994,** *50* (24), 17953.

(37) Kresse, G.; Furthmüller, J. Efficient iterative schemes for ab initio total-energy calculations using a plane-wave basis set. *Physical Review B* **1996,** *54* (16), 11169.

(38) Jain, A.; Hautier, G.; Moore, C. J.; Ping Ong, S.; Fischer, C. C.; Mueller, T.; Persson, K. A.; Ceder, G. A high-throughput infrastructure for density functional theory calculations. *Comput. Mater. Sci.* **2011,** *50* (8), 2295.

(39) Wang, L.; Maxisch, T.; Ceder, G. Oxidation energies of transition metal oxides within the GGA+U framework. *Phys. Rev. B: Condens. Matter Mater. Phys.* **2006,** *73* (19), 195107.

(40) Jain, A.; Hautier, G.; Ong, S. P.; Moore, C. J.; Fischer, C. C.; Persson, K. A.; Ceder, G. Formation enthalpies by mixing GGA and GGA+U calculations. *Phys. Rev. B: Condens. Matter Mater. Phys.* **2011,** *84* (4), 045115.

(41) Nazri, G. Preparation, structure and ionic conductivity of lithium phosphide. *Solid State Ionics* **1989,** *34* (1), 97.

(42) Ohta, S.; Kobayashi, T.; Seki, J.; Asaoka, T. Electrochemical performance of an all-solid-state lithium ion battery with garnet-type oxide electrolyte. *J. Power Sources* **2012,** *202*, 332.

(43) Nam, Y. J.; Cho, S.-J.; Oh, D. Y.; Lim, J.-M.; Kim, S. Y.; Song, J. H.; Lee, Y.-G.; Lee, S.-Y.; Jung, Y. S. Bendable and Thin Sulfide Solid Electrolyte Film: A New Electrolyte Opportunity for Free-Standing and Stackable High-Energy All-Solid-State Lithium-Ion Batteries. *Nano Lett.* **2015,** *15* (5), 3317.

(44) Kim, K. H.; Iriyama, Y.; Yamamoto, K.; Kumazaki, S.; Asaka, T.; Tanabe, K.; Fisher, C. A. J.; Hirayama, T.; Murugan, R.; Ogumi, Z. Characterization of the interface between LiCoO2 and Li7La3Zr2O12 in an all-solid-state rechargeable lithium battery. *J. Power Sources* **2011,** *196* (2), 764.

(45) Schwöbel, A.; Hausbrand, R.; Jaegermann, W. Interface reactions between LiPON and lithium studied by in-situ X-ray photoemission. *Solid State Ionics* **2015,** *273*, 51.

(46) Sakuda, A.; Hayashi, A.; Tatsumisago, M. Interfacial Observation between LiCoO2 Electrode and Li2S−P2S5 Solid Electrolytes of All-Solid-State Lithium Secondary Batteries Using Transmission Electron Microscopy. *Chem. Mater.* **2010,** *22* (3), 949.

(47) Leung, K.; Leenheer, A. How Voltage Drops are Manifested by Lithium Ion Configurations at Interfaces and in Thin Films on Battery Electrodes. *J. Phys. Chem. C* **2015,** *119* (19), 10234.

(48) Haruyama, J.; Sodeyama, K.; Han, L.; Takada, K.; Tateyama, Y. Space–Charge Layer Effect at Interface between Oxide Cathode and Sulfide Electrolyte in All-Solid-State Lithium-Ion Battery. *Chem. Mater.* **2014,** *26* (14), 4248.

(49) Chen, C. H.; Amine, K. Ionic conductivity, lithium insertion and extraction of lanthanum lithium titanate. *Solid State Ionics* **2001,** *144* (1–2), 51

(50) Feng, J. K.; Lu, L.; Lai, M. O. Lithium storage capability of lithium ion conductor Li1.5Al0.5Ge1.5(PO4)3. *J. Alloys Compd.* **2010,** *501* (2), 255.

(51) Alpen, U. v.; Bell, M. F.; Wichelhaus, W.; Cheung, K. Y.; Dudley, G. J. Ionic conductivity of Li14Zn(GeO4)4 (LISICON). *Electrochim. Acta* **1978,** *23* (12), 1395.

(52) Knauth, P. Inorganic solid Li ion conductors: An overview. *Solid State Ionics* **2009,** *180* (14–16), 911.

(53) West, W. C.; Whitacre, J. F.; Lim, J. R. Chemical stability enhancement of lithium conducting solid electrolyte plates using sputtered LiPON thin films. *J. Power Sources* **2004,** *126* (1-2), 134.

(54) Rangasamy, E.; Liu, Z.; Gobet, M.; Pilar, K.; Sahu, G.; Zhou, W.; Wu, H.; Greenbaum, S.; Liang, C. An Iodide-Based Li7P2S8I Superionic Conductor. *J. Am. Chem. Soc.* **2015,** *137* (4), 1384.

(55) Lepley, N. D.; Holzwarth, N. A. W.; Du, Y. A. Structures, Li+ mobilities, and interfacial properties of solid electrolytes Li3PS4 and Li3PO4 from first principles. *Phys. Rev. B: Condens. Matter Mater. Phys.* **2013,** *88* (10), 104103.

(56) Weppner, W. In *Materials for Lithium-Ion Batteries*; Julien, C.;Stoynov, Z., Eds.; Springer Netherlands: Dordrecht, 2000; Vol. 85.

(57) Kotobuki, M.; Munakata, H.; Kanamura, K.; Sato, Y.; Yoshida, T. Compatibility of Li7La3Zr2O12 Solid Electrolyte to All-Solid-State Battery Using Li Metal Anode. *J. Electrochem. Soc.* **2010,** *157* (10), A1076.

(58) Wolfenstine, J.; Allen, J. L.; Read, J.; Sakamoto, J. Chemical stability of cubic Li7La3Zr2O12 with molten lithium at elevated temperature. *J. Mater. Sci.* **2013,** *48* (17), 5846.

(59) McCloskey, B. D.; Scheffler, R.; Speidel, A.; Girishkumar, G.; Luntz, A. C. On the Mechanism of Nonaqueous Li–O2 Electrochemistry on C and Its Kinetic Overpotentials: Some Implications for Li–Air Batteries. *J. Phys. Chem. C* **2012,** *116* (45), 23897.

(60) Woo, J. H.; Trevey, J. E.; Cavanagh, A. S.; Choi, Y. S.; Kim, S. C.; George, S. M.; Oh, K. H.; Lee, S.-H. Nanoscale interface modification of LiCoO2 by Al2O3 atomic layer deposition for solid-state Li batteries. *J. Electrochem. Soc.* **2012,** *159* (7), A1120.

(61) Ramachandran, R.; Saranya, M.; Santhosh, C.; Velmurugan, V.; Raghupathy, B. P. C.; Jeong, S. K.; Grace, A. N. Co9S8 nanoflakes on graphene (Co9S8/G) nanocomposites for high performance supercapacitors. *RSC Advances* **2014,** *4* (40), 21151.

(62) Kishida, K.; Wada, N.; Adachi, H.; Tanaka, K.; Inui, H.; Yada, C.; Iriyama, Y.; Ogumi, Z. Microstructure of the LiCoO 2 (cathode)/La 2/3− x Li 3x TiO 3 (electrolyte) interface and its influences on the electrochemical properties. *Acta Mater.* **2007,** *55* (14), 4713.

(63) Kato, T.; Motoyama, M.; Iriyama, Y. the 228th ECS Meeting, Phoenix, AZ, USA, 2015; p 398.

(64) Okumura, T.; Nakatsutsumi, T.; Ina, T.; Orikasa, Y.; Arai, H.; Fukutsuka, T.; Iriyama, Y.; Uruga, T.; Tanida, H.; Uchimoto, Y. Depth-resolved X-ray absorption spectroscopic study on nanoscale observation of the electrode–solid electrolyte interface for all solid state lithium ion batteries. *J. Mater. Chem.* **2011,** *21* (27), 10051.

(65) Zhang, H.; Liu, X.; Qi, Y.; Liu, V. On the La2/3−xLi3xTiO3/Al2O3 composite solid-electrolyte for Li-ion conduction. *J. Alloys Compd.* **2013,** *577*, 57.

(66) Jacke, S.; Song, J.; Cherkashinin, G.; Dimesso, L.; Jaegermann, W. Investigation of the solid-state electrolyte/cathode LiPON/LiCoO2 interface by photoelectron spectroscopy. *Ionics* **2010,** *16* (9), 769.

(67) Kim, Y.; Veith, G. M.; Nanda, J.; Unocic, R. R.; Chi, M.; Dudney, N. J. High voltage stability of LiCoO 2 particles with a nano-scale Lipon coating. *Electrochim. Acta* **2011,** *56* (19), 6573.

(68) Iriyama, Y.; Kako, T.; Yada, C.; Abe, T.; Ogumi, Z. Reduction of charge transfer resistance at the lithium phosphorus oxynitride/lithium cobalt oxide interface by thermal treatment. *J. Power Sources* **2005,** *146* (1), 745.

(69) Ruzmetov, D.; Oleshko, V. P.; Haney, P. M.; Lezec, H. J.; Karki, K.; Baloch, K. H.; Agrawal, A. K.; Davydov, A. V.; Krylyuk, S.; Liu, Y.et al. Electrolyte Stability Determines Scaling Limits for Solid-State 3D Li Ion Batteries. *Nano Lett.* **2012,** *12* (1), 505.

(70) Dudney, N. J. Solid-state thin-film rechargeable batteries. *Mater. Sci. Eng., B* **2005,** *116* (3), 245.

(71) Kobayashi, Y.; Miyashiro, H.; Takei, K.; Shigemura, H.; Tabuchi, M.; Kageyama, H.; Iwahori, T. 5 V Class All-Solid-State Composite Lithium Battery with Li3PO4 Coated LiNi0.5Mn1.5O4. *J. Electrochem. Soc.* **2003,** *150* (12), A1577.

(72) Li, X.; Yang, R.; Cheng, B.; Hao, Q.; Xu, H.; Yang, J.; Qian, Y. Enhanced electrochemical properties of nano-Li 3 PO 4 coated on the LiMn 2 O 4 cathode material for lithium ion battery at 55 C. *Mater. Lett.* **2012,** *66* (1), 168.

(73) Song, H. G.; Kim, J. Y.; Kim, K. T.; Park, Y. J. Enhanced electrochemical properties of Li (Ni 0.4 Co 0.3 Mn 0.3) O 2 cathode by surface modification using Li 3 PO 4-based materials. *J. Power Sources* **2011,** *196* (16), 6847.

(74) Wang, Y., Michigan State University, 2014.

(75) Raccah, P. M.; Goodenough, J. B. First-Order Localized-Electron⇆ Collective-Electron Transition in LaCoO3. *Physical Review* **1967,** *155* (3), 932.

(76) Dudney, N. J. Solid-state thin-film rechargeable batteries. *Materials Science and Engineering: B* **2005,** *116* (3), 245.

(77) Ohta, N.; Takada, K.; Zhang, L.; Ma, R.; Osada, M.; Sasaki, T. Enhancement of the High-Rate Capability of Solid-State Lithium Batteries by Nanoscale Interfacial Modification. *Adv. Mater.* **2006,** *18* (17), 2226.

(78) Kitaura, H.; Hayashi, A.; Tadanaga, K.; Tatsumisago, M. Improvement of electrochemical performance of all-solid-state lithium secondary batteries by surface modification of LiMn2O4 positive electrode. *Solid State Ionics* **2011,** *192* (1), 304.

(79) Takada, K.; Ohta, N.; Zhang, L.; Fukuda, K.; Sakaguchi, I.; Ma, R.; Osada, M.; Sasaki, T. Interfacial modification for high-power solid-state lithium batteries. *Solid State Ionics* **2008,** *179* (27-32), 1333.

(80) Ohta, N.; Takada, K.; Sakaguchi, I.; Zhang, L.; Ma, R.; Fukuda, K.; Osada, M.; Sasaki, T. LiNbO3-coated LiCoO2 as cathode material for all solid-state lithium secondary batteries. *Electrochem. Commun.* **2007,** *9* (7), 1486.

(81) Kato, T.; Hamanaka, T.; Yamamoto, K.; Hirayama, T.; Sagane, F.; Motoyama, M.; Iriyama, Y. In-situ Li7La3Zr2O12/LiCoO2 interface modification for advanced all-solid-state battery. *J. Power Sources* **2014,** *260*, 292.

(82) Sakuda, A.; Kitaura, H.; Hayashi, A.; Tadanaga, K.; Tatsumisago, M. Improvement of High-Rate Performance of All-Solid-State Lithium Secondary Batteries Using LiCoO2 Coated with Li2O–SiO2 Glasses. *Electrochem. Solid-State Lett.* **2008,** *11* (1), A1.

(83) Jin, Y.; Li, N.; Chen, C. H.; Wei, S. Q. Electrochemical Characterizations of Commercial LiCoO2 Powders with Surface Modified by Li3PO4 Nanoparticles. *Electrochem. Solid-State Lett.* **2006,** *9* (6), A273.

(84) Visco, S.; Nimon, V.; Petrov, A.; Pridatko, K.; Goncharenko, N.; Nimon, E.; De Jonghe, L.; Volfkovich, Y.; Bograchev, D. Aqueous and nonaqueous lithium-air batteries enabled by water-stable lithium metal electrodes. *J. Solid State Electrochem.* **2014,** *18* (5), 1443.

(85) Chen, C. H.; Amine, K. Ionic conductivity, lithium insertion and extraction of lanthanum lithium titanate. *Solid State Ionics* **2001,** *144* (1), 51.

(86) Alpen, U. V.; Rabenau, A.; Talat, G. H. Ionic conductivity in Li3N single crystals. *Appl. Phys. Lett.* **1977,** *30* (12), 621.

(87) Deiseroth, H.-J.; Kong, S.-T.; Eckert, H.; Vannahme, J.; Reiner, C.; Zaiß, T.; Schlosser, M. Li6PS5X: A Class of Crystalline Li-Rich Solids With an Unusually High Li+ Mobility. *Angew. Chem. Int. Ed.* **2008,** *47* (4), 755.

(88) Bouchard, R. J.; Russo, P. A.; Wold, A. Preparation and electrical properties of some thiospinels. *Inorg. Chem.* **1965,** *4* (5), 685.

(89) Xu, W.; Wang, J.; Ding, F.; Chen, X.; Nasybulin, E.; Zhang, Y.; Zhang, J.-G. Lithium metal anodes for rechargeable batteries. *Energy Environ. Sci.* **2014,** *7* (2), 513.

(90) Zhang, K.; Lee, G. H.; Park, M.; Li, W.; Kang, Y. M. Recent Developments of the Lithium Metal Anode for Rechargeable Non-Aqueous Batteries. *Adv. Energy Mater.* **2016,** *6* (20), 1600811.

(91) Tarascon, J. M.; Armand, M. Issues and challenges facing rechargeable lithium batteries. *Nature* **2001,** *414* (6861), 359.

(92) Whittingham, M. S. History, Evolution, and Future Status of Energy Storage. *Proceedings of the IEEE* **2012,** *100* (Special Centennial Issue), 1518.

(93) Aurbach, D.; Zinigrad, E.; Cohen, Y.; Teller, H. A short review of failure mechanisms of lithium metal and lithiated graphite anodes in liquid electrolyte solutions. *Solid State Ionics* **2002,** *148* (3), 405.

(94) Xu, K. Nonaqueous liquid electrolytes for lithium-based rechargeable batteries. *Chem. Rev.* **2004,** *104* (10), 4303.

(95) Xu, K. Electrolytes and interphases in Li-ion batteries and beyond. *Chem. Rev.* **2014,** *114* (23), 11503.

(96) Cheng, X. B.; Zhang, R.; Zhao, C. Z.; Wei, F.; Zhang, J. G.; Zhang, Q. A Review of Solid Electrolyte Interphases on Lithium Metal Anode. *Adv. Sci.* **2015,** *3* (3), 1500213.

(97) Peled, E. The electrochemical behavior of alkali and alkaline earth metals in nonaqueous battery systems—the solid electrolyte interphase model. *J. Electrochem. Soc.* **1979,** *126* (12), 2047.

(98) Gauthier, M.; Carney, T. J.; Grimaud, A.; Giordano, L.; Pour, N.; Chang, H.-H.; Fenning, D. P.; Lux, S. F.; Paschos, O.; Bauer, C.et al. Electrode–Electrolyte Interface in Li-Ion Batteries: Current Understanding and New Insights. *J. Phys. Chem. Lett.* **2015,** *6* (22), 4653.

(99) Zhang, Y. J.; Wang, W.; Tang, H.; Bai, W. Q.; Ge, X.; Wang, X. L.; Gu, C. D.; Tu, J. P. An ex-situ nitridation route to synthesize Li3N-modified Li anodes for lithium secondary batteries. *J. Power Sources* **2015,** *277*, 304.

(100) Wu, M.; Wen, Z.; Liu, Y.; Wang, X.; Huang, L. Electrochemical behaviors of a Li3N modified Li metal electrode in secondary lithium batteries. *J. Power Sources* **2011,** *196* (19), 8091.

(101) Ma, G.; Wen, Z.; Wu, M.; Shen, C.; Wang, Q.; Jin, J.; Wu, X. A lithium anode protection guided highly-stable lithium–sulfur battery. *Chem. Commun.* **2014,** *50* (91), 14209.

(102) Li, N. W.; Yin, Y. X.; Li, J. Y.; Zhang, C. H.; Guo, Y. G. Passivation of Lithium Metal Anode via Hybrid Ionic Liquid Electrolyte toward Stable Li Plating/Stripping. *Adv. Sci.* **2016**, 1600400.

(103) Lu, Y.; Tu, Z.; Archer, L. A. Stable lithium electrodeposition in liquid and nanoporous solid electrolytes. *Nat. Mater.* **2014,** *13* (10), 961.

(104) Guo, J.; Wen, Z.; Wu, M.; Jin, J.; Liu, Y. Vinylene carbonate–LiNO3: A hybrid additive in carbonic ester electrolytes for SEI modification on Li metal anode. *Electrochem. Commun.* **2015,** *51*, 59.

(105) Amatucci, G. G.; Pereira, N. In *Lithium Batteries: Science and Technology*; Nazri, G.-A.;Pistoia, G., Eds.; Springer US: Boston, MA, 2003.

(106) Zhu, Y.; He, X.; Mo, Y. First principles study on electrochemical and chemical stability of solid electrolyte-electrode interfaces in all-solid-state Li-ion batteries. *J. Mater. Chem. A* **2016,** *4* (9), 3253.

(107) Wenzel, S.; Weber, D. A.; Leichtweiss, T.; Busche, M. R.; Sann, J.; Janek, J. Interphase formation and degradation of charge transfer kinetics between a lithium metal anode and highly crystalline Li 7 P 3 S 11 solid electrolyte. *Solid State Ionics* **2016,** *286*, 24.

(108) Kanno, R.; Hata, T.; Kawamoto, Y.; Irie, M. Synthesis of a new lithium ionic conductor, thio-LISICON–lithium germanium sulfide system. *Solid State Ionics* **2000,** *130* (1), 97.

(109) Marom, R.; Amalraj, S. F.; Leifer, N.; Jacob, D.; Aurbach, D. A review of advanced and practical lithium battery materials. *J. Mater. Chem.* **2011,** *21* (27), 9938.

(110) Xiao, X.; Lu, P.; Ahn, D. Ultrathin multifunctional oxide coatings for lithium ion batteries. *Adv. Mater.* **2011,** *23* (34), 3911.

(111) Jing, H.-K.; Kong, L.-L.; Liu, S.; Li, G.-R.; Gao, X.-P. Protected lithium anode with porous Al2O3 layer for lithium–sulfur battery. *J. Mater. Chem. A* **2015,** *3* (23), 12213.

(112) Liu, Y.; Hudak, N. S.; Huber, D. L.; Limmer, S. J.; Sullivan, J. P.; Huang, J. Y. In situ transmission electron microscopy observation of pulverization of aluminum nanowires and evolution of the thin surface Al2O3 layers during lithiation–delithiation cycles. *Nano Lett.* **2011,** *11* (10), 4188.

(113) Senoh, H.; Takeuchi, T.; Kageyama, H.; Sakaebe, H.; Yao, M.; Nakanishi, K.; Ohta, T.; Sakai, T.; Yasuda, K. Electrochemical characteristics of aluminum sulfide for use in lithium secondary batteries. *J. Power Sources* **2010,** *195* (24), 8327.

(114) Yim, W. M.; Stofko, E. J.; Zanzucchi, P. J.; Pankove, J. I.; Ettenberg, M.; Gilbert, S. L. Epitaxially grown AlN and its optical band gap. *J. Appl. Phys.* **1973,** *44* (1), 292.

(115) Yamane, H.; Kikkawa, S.; Koizumi, M. Lithium aluminum nitride, Li3AlN2 as a lithium solid electrolyte. *Solid State Ionics* **1985,** *15* (1), 51.

(116) Braga, M. H.; Ferreira, J. A.; Stockhausen, V.; Oliveira, J. E.; El-Azab, A. Novel Li3ClO based glasses with superionic properties for lithium batteries. *J. Mater. Chem. A* **2014,** *2* (15), 5470.

(117) Miara, L. J.; Suzuki, N.; Richards, W. D.; Wang, Y.; Kim, J. C.; Ceder, G. Li-ion conductivity in Li9S3N. *J. Mater. Chem. A* **2015,** *3* (40), 20338.

(118) Bertschler, E.-M.; Dietrich, C.; Janek, J.; Schnick, W. Li18P6N16-A Lithium Nitridophosphate with Unprecedented Tricyclic [P6N16] 18− Ions. *Chemistry-A European Journal* **2016,** *23* (9), 2185.

(119) Zhang, Y.-j.; Bai, W.-q.; Wang, X.-l.; Xia, X.-h.; Gu, C.-d.; Tu, J.-p. In situ confocal microscopic observation on inhibiting the dendrite formation of a-CN x/Li electrode. *J. Mater. Chem. A* **2016,** *4* (40), 15597.

(120) Li, X.; Geng, D.; Zhang, Y.; Meng, X.; Li, R.; Sun, X. Superior cycle stability of nitrogen-doped graphene nanosheets as anodes for lithium ion batteries. *Electrochem. Commun.* **2011,** *13* (8), 822.

(121) Qie, L.; Chen, W. M.; Wang, Z. H.; Shao, Q. G.; Li, X.; Yuan, L. X.; Hu, X. L.; Zhang, W. X.; Huang, Y. H. Nitrogen-doped porous carbon nanofiber webs as anodes for lithium ion batteries with a superhigh capacity and rate capability. *Adv. Mater.* **2012,** *24* (15), 2047.

(122) Reddy, A. L. M.; Srivastava, A.; Gowda, S. R.; Gullapalli, H.; Dubey, M.; Ajayan, P. M. Synthesis of nitrogen-doped graphene films for lithium battery application. *ACS nano* **2010,** *4* (11), 6337.

(123) Zhang, S. S. Role of LiNO3 in rechargeable lithium/sulfur battery. *Electrochim. Acta* **2012,** *70*, 344.

(124) Zhao, C.-Z.; Cheng, X.-B.; Zhang, R.; Peng, H.-J.; Huang, J.-Q.; Ran, R.; Huang, Z.-H.; Wei, F.; Zhang, Q. Li2S5-based ternary-salt electrolyte for robust lithium metal anode. *Energy Storage Materials* **2016,** *3*, 77.

(125) Zheng, D.; Yang, X.-Q.; Qu, D. Reaction between Lithium Anode and Polysulfide Ions in a Lithium–Sulfur Battery. *ChemSusChem* **2016,** *9* (17), 2348.

(126) Aurbach, D.; Pollak, E.; Elazari, R.; Salitra, G.; Kelley, C. S.; Affinito, J. On the surface chemical aspects of very high energy density, rechargeable Li–sulfur batteries. *J. Electrochem. Soc.* **2009,** *156* (8), A694.

(127) Xiong, S.; Xie, K.; Diao, Y.; Hong, X. Characterization of the solid electrolyte interphase on lithium anode for preventing the shuttle mechanism in lithium–sulfur batteries. *J. Power Sources* **2014,** *246*, 840.

(128) Xiong, S.; Xie, K.; Diao, Y.; Hong, X. Properties of surface film on lithium anode with LiNO 3 as lithium salt in electrolyte solution for lithium–sulfur batteries. *Electrochim. Acta* **2012,** *83*, 78.

(129) Li, W.; Yao, H.; Yan, K.; Zheng, G.; Liang, Z.; Chiang, Y.-M.; Cui, Y. The synergetic effect of lithium polysulfide and lithium nitrate to prevent lithium dendrite growth. *Nature communications* **2015,** *6*.

(130) Jozwiuk, A.; Berkes, B. B.; Weiß, T.; Sommer, H.; Janek, J.; Brezesinski, T. The critical role of lithium nitrate in the gas evolution of lithium–sulfur batteries. *Energy Environ. Sci.* **2016,** *9* (8), 2603.

(131) Tapia-Ruiz, N.; Segalés, M.; Gregory, D. H. The chemistry of ternary and higher lithium nitrides. *Coord. Chem. Rev.* **2013,** *257* (13), 1978.

(132) Zhong, Y.; Xia, X.; Shi, F.; Zhan, J.; Tu, J.; Fan, H. J. Transition Metal Carbides and Nitrides in Energy Storage and Conversion. *Adv. Sci.* **2016,** *3* (5), 1500286.

(133) Luo, W.; Gong, Y.; Zhu, Y.; Fu, K.; Dai, J.; Lacey, S. D.; Wang, C.; Liu, B.; Han, X.; Mo, Y. Transition from Super-lithiophobicity to Super-lithiophilicity of Garnet Solid-State Electrolyte. *J. Am. Chem. Soc.* **2016,** *138* (37), 12258.

(134) Czerwiec, T.; Renevier, N.; Michel, H. Low-temperature plasma-assisted nitriding. *Surf. Coat. Technol.* **2000,** *131* (1), 267.

(135) Monroe, C.; Newman, J. The impact of elastic deformation on deposition kinetics at lithium/polymer interfaces. *J. Electrochem. Soc.* **2005,** *152* (2), A396.

(136) Yu, S.; Schmidt, R. D.; Garcia-Mendez, R.; Herbert, E.; Dudney, N. J.; Wolfenstine, J. B.; Sakamoto, J.; Siegel, D. J. Elastic Properties of the Solid Electrolyte Li7La3Zr2O12 (LLZO). *Chem. Mater.* **2015,** *28* (1), 197.

(137) Herbert, E. G.; Tenhaeff, W. E.; Dudney, N. J.; Pharr, G. M. Mechanical characterization of LiPON films using nanoindentation. *Thin Solid Films* **2011,** *520* (1), 413.

(138) Zhan, G. D.; Mitomo, M.; Nishimura, T.; Xie, R. J.; Sakuma, T.; Ikuhara, Y. Superplastic Behavior of Fine-Grained β-Silicon Nitride Material under Compression. *J. Am. Ceram. Soc.* **2000,** *83* (4), 841.

(139) Sinha, N. N.; Marks, T. H.; Dahn, H. M.; Smith, A. J.; Burns, J. C.; Coyle, D. J.; Dahn, J. J.; Dahn, J. R. The rate of active lithium loss from a soft carbon negative electrode as a function of temperature, time and electrode potential. *J. Electrochem. Soc.* **2012,** *159* (10), A1672.

(140) Smith, A. J.; Dahn, H. M.; Burns, J. C.; Dahn, J. R. Long-term low-rate cycling of LiCoO2/graphite Li-ion cells at 55 C. *J. Electrochem. Soc.* **2012,** *159* (6), A705.

(141) David, I. N.; Thompson, T.; Wolfenstine, J.; Allen, J. L.; Sakamoto, J. Microstructure and Li-Ion Conductivity of Hot-Pressed Cubic Li7La3Zr2O12. *Journal of the American Ceramic Society* **2015,** *98* (4), 1209.

(142) Murugan, R.; Thangadurai, V.; Weppner, W. Fast lithium ion conduction in garnet-type Li7La3Zr2O12. *Angewandte Chemie International Edition* **2007,** *46* (41), 7778.

(143) Tenhaeff, W. E.; Rangasamy, E.; Wang, Y.; Sokolov, A. P.; Wolfenstine, J.; Sakamoto, J.; Dudney, N. J. Resolving the Grain Boundary and Lattice Impedance of Hot-Pressed Li7La3Zr2O12 Garnet Electrolytes. *ChemElectroChem* **2014,** *1* (2), 375.

(144) Cheng, L.; Chen, W.; Kunz, M.; Persson, K.; Tamura, N.; Chen, G.; Doeff, M. Effect of surface microstructure on electrochemical performance of garnet solid electrolytes. *ACS applied materials & interfaces* **2015,** *7* (3), 2073.

(145) Abrashev, M. V.; Litvinchuk, A. P.; Iliev, M. N.; Meng, R. L.; Popov, V. N.; Ivanov, V. G.; Chakalov, R. A.; Thomsen, C. Comparative study of optical phonons in the rhombohedrally distorted perovskites LaAlO 3 and LaMnO 3. *Physical Review B* **1999,** *59* (6), 4146.

(146) Wang, Y.; Huq, A.; Lai, W. Insight into lithium distribution in lithium-stuffed garnet oxides through neutron diffraction and atomistic simulation: Li 7-x La 3 Zr 2-x Ta x O 12 (x= 0–2) series. *Solid State Ionics* **2014,** *255*, 39.

(147) Sakamoto, J.; Rangasamy, E.; Kim, H.; Kim, Y.; Wolfenstine, J. Synthesis of nano-scale fast ion conducting cubic Li7La3Zr2O12. *Nanotechnology* **2013,** *24* (42), 424005.

(148) Adams, S.; Rao, R. P. Ion transport and phase transition in Li 7− x La 3 (Zr 2− x M x) O 12 (M= Ta 5+, Nb 5+, x= 0, 0.25). *Journal of Materials Chemistry* **2012,** *22* (4), 1426.

(149) Klenk, M.; Lai, W. Local structure and dynamics of lithium garnet ionic conductors: tetragonal and cubic Li 7 La 3 Zr 2 O 7. *Physical Chemistry Chemical Physics* **2015,** *17* (14), 8758.

(150) Burbano, M.; Carlier, D.; Boucher, F.; Morgan, B. J.; Salanne, M. Sparse cyclic excitations explain the low ionic conductivity of stoichiometric Li 7 La 3 Zr 2 O 12. *Physical review letters* **2016,** *116* (13), 135901.

(151) Goldschmidt, V. *Atlas der Krystallformen*; C. Winter, 1913.

(152) Plimpton, S. Fast parallel algorithms for short-range molecular dynamics. *Journal of computational physics* **1995,** *117* (1), 1.

(153) Wang, Y.; Richards, W. D.; Ong, S. P.; Miara, L. J.; Kim, J. C.; Mo, Y.; Ceder, G. Design principles for solid-state lithium superionic conductors. *Nature materials* **2015,** *14* (10), 1026.

(154) Baral, A. K.; Narayanan, S.; Ramezanipour, F.; Thangadurai, V. Evaluation of fundamental transport properties of Li-excess garnet-type Li 5+ 2x La 3 Ta 2− x Y x O 12 (x= 0.25, 0.5 and 0.75) electrolytes using AC impedance and dielectric spectroscopy. *Physical Chemistry Chemical Physics* **2014,** *16* (23), 11356.

(155) Manthiram, A.; Yu, X.; Wang, S. Lithium battery chemistries enabled by solid-state electrolytes. *Nature Reviews Materials* **2017,** *2* (4), 16103.

(156) Tealdi, C.; Heath, J.; Islam, M. S. Feeling the strain: enhancing ionic transport in olivine phosphate cathodes for Li-and Na-ion batteries through strain effects. *Journal of Materials Chemistry A* **2016,** *4* (18), 6998.

(157) Brunetti, G.; Robert, D.; Bayle-Guillemaud, P.; Rouviere, J. L.; Rauch, E. F.; Martin, J. F.; Colin, J. F.; Bertin, F.; Cayron, C. Confirmation of the domino-cascade model by LiFePO4/FePO4 precession electron diffraction. *Chemistry of Materials* **2011,** *23* (20), 4515.

(158) Kushima, A.; Yildiz, B. Oxygen ion diffusivity in strained yttria stabilized zirconia: where is the fastest strain? *Journal of Materials Chemistry* **2010,** *20* (23), 4809.

(159) Ong, S. P.; Mo, Y.; Richards, W. D.; Miara, L.; Lee, H. S.; Ceder, G. Phase stability, electrochemical stability and ionic conductivity of the Li 10±1 MP 2 X 12 (M= Ge, Si, Sn, Al or P, and X= O, S or Se) family of superionic conductors. *Energy & Environmental Science* **2013,** *6* (1), 148.

(160) Ni, J. E.; Case, E. D.; Sakamoto, J. S.; Rangasamy, E.; Wolfenstine, J. B. Room temperature elastic moduli and Vickers hardness of hot-pressed LLZO cubic garnet. *Journal of Materials Science* **2012,** *47* (23), 7978.

(161) Coleman, S. P.; Spearot, D. E.; Capolungo, L. Virtual diffraction analysis of Ni [0 1 0] symmetric tilt grain boundaries. *Modelling and Simulation in Materials Science and Engineering* **2013,** *21* (5), 055020.

(162) He, X.; Mo, Y. Accelerated materials design of Na0.5Bi0.5TiO3 oxygen ionic conductors based on first principles calculations. *Physical Chemistry Chemical Physics* **2015,** *17* (27), 18035.

(163) Fourquet, J. L.; Duroy, H.; Crosnier-Lopez, M. P. Structural and Microstructural Studies of the Series La2/3−xLi3x□1/3−2xTiO3. *J. Solid State Chem.* **1996,** *127* (2), 283.

(164) Homma, K.; Yonemura, M.; Kobayashi, T.; Nagao, M.; Hirayama, M.; Kanno, R. Crystal structure and phase transitions of the lithium ionic conductor Li3PS4. *Solid State Ionics* **2011,** *182* (1), 53.

(165) Senevirathne, K.; Day, C. S.; Gross, M. D.; Lachgar, A.; Holzwarth, N. A. W. A new crystalline LiPON electrolyte: Synthesis, properties, and electronic structure. *Solid State Ionics* **2013,** *233* (0), 95.

(166) Kamaya, N.; Homma, K.; Yamakawa, Y.; Hirayama, M.; Kanno, R.; Yonemura, M.; Kamiyama, T.; Kato, Y.; Hama, S.; Kawamoto, K.et al. A lithium superionic conductor. *Nat. Mater.* **2011,** *10* (9), 682.

(167) Murayama, M.; Kanno, R.; Kawamoto, Y.; Kamiyama, T. Structure of the thio-LISICON, Li4GeS4. *Solid State Ionics* **2002,** *154–155*, 789.

(168) Deiseroth, H. J.; Kong, S. T.; Eckert, H.; Vannahme, J.; Reiner, C.; Zaiss, T.; Schlosser, M. Li6PS5X: a class of crystalline Li-rich solids with an unusually high Li+ mobility. *Angewandte Chemie* **2008,** *47* (4), 755.

(169) Awaka, J.; Takashima, A.; Kataoka, K.; Kijima, N.; Idemoto, Y.; Akimoto, J. Crystal Structure of Fast Lithium-ion-conducting Cubic Li7La3Zr2O12. *Chem. Lett.* **2011,** *40* (1), 60.

(170) Dashjav, E.; Tietz, F. Neutron Diffraction Analysis of NASICON-type Li1+xAlxTi2–xP3O12. *Z. Anorg. Allg. Chem.* **2014,** *640* (15), 3070.

(171) Hong, H. Y. P. Crystal structure and ionic conductivity of Li14Zn(GeO4)4 and other new Li+ superionic conductors. *Materials Research Bulletin* **1978,** *13* (2), 117.